Numerical methods for the simulation of particle motion in electromagnetic fields

PhD thesis of Abele Simona

Joint PhD programme between

Supervised by

Luca Bonaventura

Co-supervised by

Carlo de Falco

Sebastian Schöps

Dipartimento di Matematica,
Mathematical models and methods in engineering, XXXII ciclo
PhD course coordinator: Irene Maria Sabadini

Abstract

In this thesis we study numerical methods for the approximate solution of problems arising in electromagnetism. Its main motivations come from applications to the modelling of high-energy particle accelerators. In this framework, we first compare the efficiency of several numerical methods for the computation of particle trajectories in the design of a magnetic quadrupole for the High Luminosity - Large Hadron Collider (HL-LHC) project and we analyse the use of a specific vector potential gauge to reduce the computational cost. The results from this first comparison motivate the subsequent investigation of the accuracy of the numerical approximation of the field. We therefore develop a new type of discretization for the reconstruction of the magnetic scalar potential in cylindrical domains and we apply it to the field reconstruction from a realistic measurement process in a Bayesian framework. We compare this method with the reconstruction obtained by a more classical method based on the separation of variables [Jac07, Section 3.7, 3.8], highlighting the benefits of the new type of discretization and its applicability to the reconstruction process. Motivated by the need of efficient methods for the description of electromagnetic fields, we extend the study to other types of problems for axisymmetric domains, which have a high practical relevance in particle accelerator applications. In this context, we propose the use of a method based on the Fourier basis and IsoGeometric Analysis (IGA) to exploit, on one hand, the computational efficiency that can be achieved thanks to the symmetry of the domain and, on the other, the exact representation of the geometry and the good approximation properties achievable in a IGA framework. Moreover, the proposed method forms a de Rham complex, which is a crucial property that allows to obtain a stable method which produces physically correct approximations. We finally apply the method to the computation of resonant modes of an accelerating TESLA cavity.

Contents

List of Figures

List of Tables

Symbol	Description
$(x,\, y,\, z)$	Cartesian coordinates
$(\rho,\, \theta,\, z)$	Cylindrical coordinates
$\dfrac{\partial f}{\partial x}$	Partial derivative of f with respect to x, often abbreviated with $\partial_x f$

Table 1: General notation

Symbol	Description
$\boldsymbol{E}$	Electric field intensity
$\boldsymbol{H}$	Magnetic field intensity
$\boldsymbol{D}$	Electric displacement
$\boldsymbol{B}$	Magnetic induction (or flux density)
ϕ	Electric scalar potential
ψ	Magnetic scalar potential
$\boldsymbol{A}$	Magnetic vector potential
$\boldsymbol{\epsilon}$	Permittivity
$\boldsymbol{\mu}$	Permeability
ϱ	Charge density
C	Particle charge
$\boldsymbol{j}$	Current density
$\boldsymbol{\sigma}$	Conductivity

Table 2: Notation in electromagnetism

Symbol	Description
$\boldsymbol{q}$	Generalized coordinates
$\boldsymbol{p}$	Canonical momenta
$\boldsymbol{w}$	Dynamical variables $\left(\boldsymbol{q}^T,\, \boldsymbol{p}^T\right)^T$

Table 3: Notation in Hamiltonian dynamics

Chapter 1

Introduction

In this thesis we study several numerical methods for the approximate solution of problems arising in electromagnetism. The motivations for this study mainly came from the context of particle accelerators, but the proposed strategies have a much broader range of applications, as we will try to emphasize when presenting the proposed numerical techniques.

Particle accelerators are structures used to bring charged particles, which travel in bunches, to a specific speed, or energy, so that they can be used for different purposes in various research areas like health, material sciences and, especially, researches related to the fundamental models of subatomic physics. Depending on the specific application, there are different characteristics of the accelerator that determine its overall quality as, for example, the energy spread in each bunch of particles or the luminosity, which is a quantity related to the achieved collision rate. Among the various types of machines, we will consider high-energy circular accelerators for particle collisions and, in particular, an application related to the High Luminosity - Large Hadron Collider (HL-LHC) project, which is a foreseen update of the well-known Large Hadron Collider (LHC), hosted by CERN. The study of the beam dynamics requires the computation of several particle trajectories for a large number of revolutions [Wol14]. It is therefore crucial to obtain efficient numerical methods to describe the effect of each element in the accelerator over the charged particles.

Among the different elements, we will first consider the magnetic quadrupoles (see Figure 1.1), which are used to focus particle beams and whose action on charged particles can be approximately described using a linear map that relates the positions and momenta at the inlet with the ones at the outlet [Car88]. However, in the case of the design of large aperture quadrupoles foreseen for the HL-LHC project [Ros11], more accurate methods are required. In this context, a wide class of methods relies on the so called trans-

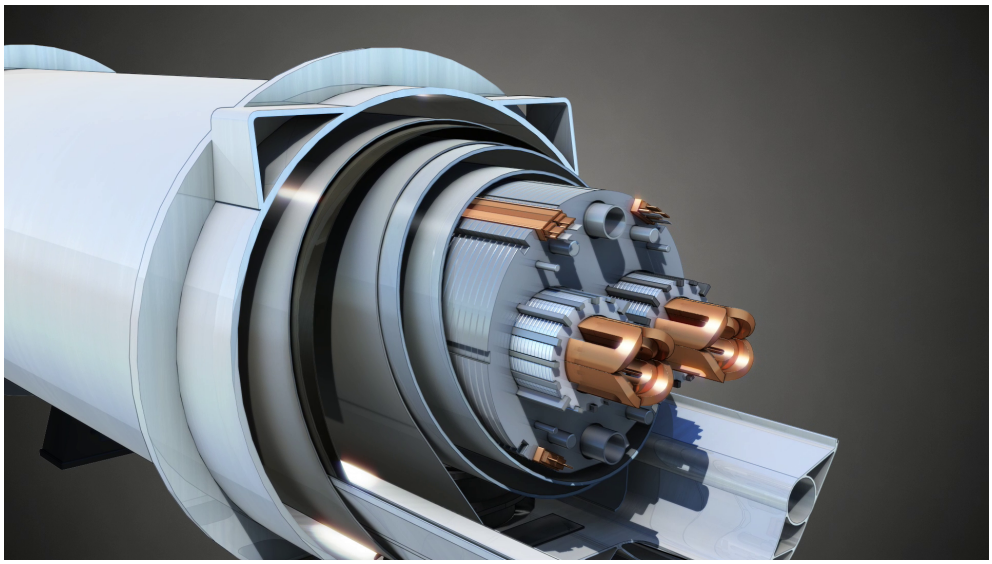

Figure 1.1: Representation of a section of a particles accelerator containing two magnetic quadrupoles used to focus the particle beams. (Source https://home.cern/resources/video/accelerators/quadrupole-animation)

fer maps, which are functions that represent a nonlinear relation between position and momenta of the particles at the inlet and the outlet, respectively. These methods typically introduce strong approximations on the field shape, such as the so called Hard Edge (HE) model, that allow then to obtain an analytic expression for the transfer map. An example of such a method, that does not consider the dependence of the field on the axial coordinate along the magnet, is the so called thin model, used in SixTrack [CER], the code developed at CERN to simulate the whole accelerator. Another example is the method proposed in [FM88], where a nonlinear contribution is added taking into account the effect of the fringe field through a limiting procedure. Other methods are based on numerical integration of the Hamilton equations which describe the motion of the particles through the field. These methods are often computationally expensive and they are strongly affected by the discretization of the field. In particular, a standard way of representing the field is achieved by locally interpolating a set of sampled values on a 3D grid (see *e.g.* [Méo12; UP14]). A more efficient representation can be instead obtained directly from the solution of Maxwell equations. An example of these representations, which will be applied in this thesis, relies on the use of the so called generalized gradients [Dra97]. Once a field description is obtained, a wide range of techniques for the integration of Hamilton equations can be applied. In this thesis, we will compare the efficiency of explicit high order Lie

methods [WFR03], implicit high order symplectic integrators [HLW06] and more conventional, non-symplectic explicit Runge-Kutta methods. Using the field description based on the generalized gradients, we will also consider a specific gauge transformation that allows to reduce the computational cost of each vector potential evaluation by approximately 50% [Sim+19a]. We finally compare the description of the nonlinear effects provided by our code with that computed with the thin model used in the SixTrack code [CER].

Another important aspect is of course the direct numerical solution of Maxwell equations, which can provide the field description for design purposes or, as already mentioned, for the computation of particle trajectories. In this framework, the standard technique is the Finite Element Method (FEM) [Mon+03], but other alternatives, such as the Boundary Element Method (BEM) [SS11] or IsoGeometric Analysis (IGA) [CHB09; Buf+11], are available and offer important advantages in specific situations. Among the different types of geometries on which we could solve Maxwell equations, we will consider axisymmetric domains which often arise in electromagnetic problems and, in particular, in particle accelerators. The solution of Maxwell equations in axisymmetric domains has been studied by different authors, both in the case of axisymmetric fields (see *e.g.* [ACJL02; CGP08; Erv13; GO12]) and for the general case (see *e.g.* [Ber+99; HL05; Lac00; MR82; Nke05; Per+17]). In this thesis, we present a method combining a spectral Fourier approach and IGA, following the strategy presented in [Oh15] for the lowest order finite element approximations. The resulting approach has good approximation properties and its discrete approximation spaces form a de Rham complex. This allows for an accurate and efficient representation of the electromagnetic field and for the solution of a wide range of problems in electromagnetism. In particular, we will apply this method to the computation of resonant modes in an accelerating TESLA cavity [Aun+00], which is another special element of particles accelerators (see Figure 1.2).

Finally, we describe the application of the proposed method to the reconstruction of the magnetic field from measurements [IG19]. More specifically, we consider the reconstruction of a quadrupolar field from the voltages induced on a spinning coil, which shows that the proposed method can also be applied to the reconstruction of the magnetic field from the available measurements.

The structure of the thesis is the following. In Chapter 2, we introduce the Maxwell equations and the functional spaces needed to formulate the problems in electromagnetism in a variational framework. In this context, we discuss the so called de Rham complex and the simplifications that can be introduced when axisymmetric domains are considered. In Chapter 3, we focus on the description of Hamiltonian systems, which will be used to

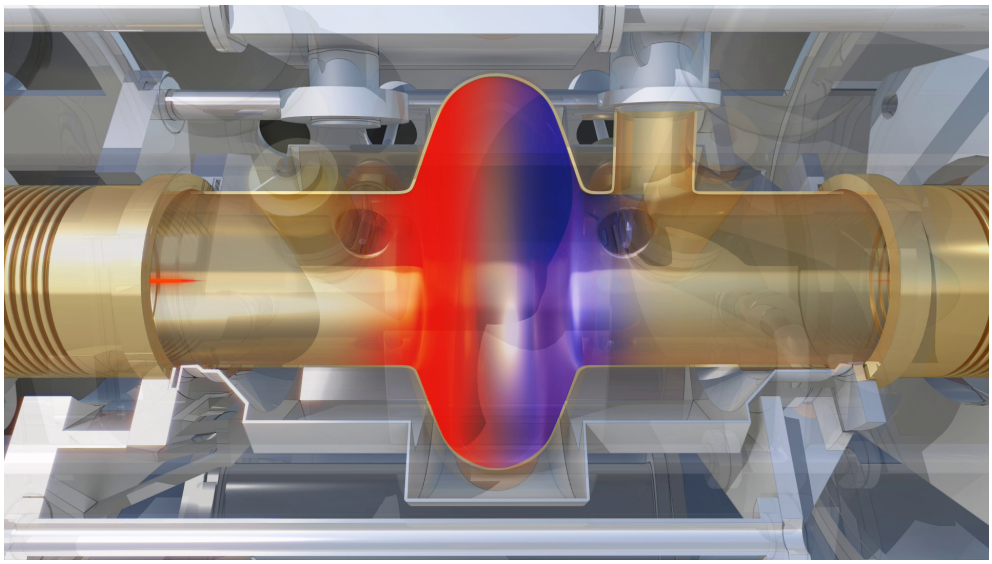

Figure 1.2: Representation of a cell of an accelerating TESLA cavity. Its oscillating electromagnetic field accelerates the particles. (Source https://home.cern/resources/video/accelerators/radio-frequency-cavity-animation)

describe the motion of charged particles in electromagnetic fields. We first introduce the concepts in the general framework of Hamiltonian mechanics and we conclude the chapter presenting the specific Hamiltonian which describes the motion of a relativistic charged particle in an electromagnetic field and some common approximations that can be done when the particle travels at high speed in a preferred direction. In Chapter 4, we present the numerical methods used to compute the solutions of the problems introduced in the first two chapters. In particular, we introduce the Galerkin approximation for the variational formulations presented in Chapter 2. We first recall the main results in the standard case of Cartesian coordinates and we then present the strategy used to deal with the particular case of cylindrical coordinates and axisymmetric domains with the use of Fourier basis and IGA, which is one of the contributions of this thesis [Sim+19b]. The solution of the Laplace problem on a cylinder is a particular case with a significant relevance in particles accelerators. We will therefore reserve a section to present the method of generalized gradients [Dra97] and another discretization, proposed in this thesis, based on the combination of a spectral and a Basis spline (B-spline) basis. We reserve the final part of the chapter to present the numerical methods employed to solve the Hamilton equations. In Chapter 5, we present two applications from the context of particle accelerators. First, magnetic quadrupoles are presented, consider-

ing different aspects. One of the main contributions of this thesis is the efficiency comparison of different methods for the computation of particle trajectories and the application of a specific gauge to significantly reduce the computational cost [Sim+19a]. We then discuss some aspects related to the field description that have a significant impact on the overall accuracy of the particle tracking and that motivate the study of different methods to describe the field. We conclude the discussion on the quadrupole presenting the results achieved in the M.Sc. thesis of Ion Gabriel Ion entitled "Bayesian methods for magnetic field reconstruction from measurements" [IG19], which was supervised by the author of this thesis during the period spent at the Technische Universität Darmstadt. In particular, we present an example of field reconstruction from measurements, which can improve the accuracy of field description and can provide important feedback on the impact of the field uncertainties on the beam dynamics. The second application considered is an accelerating TESLA cavity and, in particular, the computation of its resonant modes (eigenvalues and eigenfunctions). The axisymmetric nature of this element and its non-trivial geometry makes it a perfect example of application on which we test the new method proposed in this thesis. Finally, Chapter 6 is devoted to the conclusions and to the description of possible future developments of this work.

Chapter 2

The Maxwell equations

This chapter is devoted to the introduction of the Maxwell equations, which describe the behaviour of electromagnetic fields. The interested reader can refer, for example, to [Hip02; Jac07; Mon+03] for a more detailed exposition. We will introduce all the concepts and quantities using SI units. In Table 2.1 are reported all the quantities we will deal with, both in derived and base units of measurement. We start introducing the concept of Lipschitz domain, which is a domain with a Lipschitz boundary, according to the following definition [Mon+03, Definition 3.1].

Definition 2.1. *The boundary $\partial\Omega$ of a domain $\Omega \subset \mathbb{R}^n$ is Lipschitz if for every $\boldsymbol{x} \in \partial\Omega$ there is an open set $U \subset \mathbb{R}^n$ containing $\boldsymbol{x}$ and an orthogonal coordinate system with coordinates $\boldsymbol{\zeta} = (\zeta_1, \ldots, \zeta_n)^T$ having the following properties. There is a vector $\boldsymbol{a} \in \mathbb{R}^n$ with*

$$U = \{\boldsymbol{\zeta} : -a_j < \zeta_j < a_j,\ j = 1, \ldots, n\}$$

and a Lipschitz continuous function ϕ defined on

$$U' = \left\{\boldsymbol{\zeta}' \in \mathbb{R}^{n-1} : -a_j < \zeta_j < a_j,\ j = 1, \ldots, n-1\right\}$$

with $|\phi(\boldsymbol{\zeta}')| \leq a_n/2$ for all $\boldsymbol{\zeta}' \in U'$ such that

$$\begin{aligned} \partial\Omega \cap U &= \{\boldsymbol{\zeta} :\ \zeta_n = \phi(\boldsymbol{\zeta}'),\ \boldsymbol{\zeta}' \in U'\} \text{ and} \\ \Omega \cap U &= \{\boldsymbol{\zeta} :\ \zeta_n < \phi(\boldsymbol{\zeta}'),\ \boldsymbol{\zeta}' \in U'\}. \end{aligned} \tag{2.1}$$

The definition for a Lipschitz surface is analogous except for the second condition in (2.1). Throughout all this chapter, we will consider a surface Σ and a volume $\Omega \in \mathbb{R}^3$ that satisfy the following regularity assumptions:

Assumption 2.1. *We denote a Lipschitz orientable surface with $\Sigma \subset \mathbb{R}^3$ and a bounded Lipschitz domain with $\Omega \subset \mathbb{R}^3$.*

Symbol	Name	SI unit	SI base unit
$\boldsymbol{E}$	Electric field intensity	$\mathrm{V\,m^{-1}}$	$\mathrm{kg\,m\,A^{-1}\,s^{-3}}$
$\boldsymbol{H}$	Magnetic field intensity	$\mathrm{A\,m^{-1}}$	$\mathrm{A\,m^{-1}}$
$\boldsymbol{D}$	Electric displacement	$\mathrm{C\,m^{-2}}$	$\mathrm{A\,s\,m^{-2}}$
$\boldsymbol{B}$	Magnetic flux density	T	$\mathrm{kg\,A^{-1}\,s^{-2}}$
$\boldsymbol{\epsilon}$	Permittivity	$\mathrm{F\,m^{-1}}$	$\mathrm{kg^{-1}\,m^{-3}\,A^{2}\,s^{4}}$
$\boldsymbol{\mu}$	Permeability	$\mathrm{H\,m^{-1}}$	$\mathrm{kg\,m\,A^{-2}\,s^{-2}}$
ϱ	Charge density	$\mathrm{C\,m^{-3}}$	$\mathrm{m^{-3}\,A\,s}$
$\boldsymbol{j}$	Current density	$\mathrm{A\,m^{-2}}$	$\mathrm{A\,m^{-2}}$
$\boldsymbol{\sigma}$	Conductivity	$\mathrm{S\,m^{-1}}$	$\mathrm{kg^{-1}\,m^{-3}\,A^{2}\,s^{3}}$

Table 2.1: Electromagnetic quantities with the corresponding SI unit of measurement.

2.1 Integral and differential formulations

This section is devoted to the presentation of the different quantities that we will use in this thesis. In order to simplify the exposition, we assume that all the quantities have the regularity required by the context, postponing a more detailed discussion to the following sections. The material presented here is based on [GK04; Hip02; Jac07; Mon+03], where the interested reader can find further details. Let us consider a Lipschitz oriented surface Σ and a bounded Lipschitz domain Ω, the Maxwell equations in integral form can be written as

$$\int_{\partial\Sigma} \boldsymbol{E}\cdot\boldsymbol{\tau}\,\mathrm{d}\ell = -\frac{\mathrm{d}}{\mathrm{d}t}\int_{\Sigma}\boldsymbol{B}\cdot\boldsymbol{\nu}\,\mathrm{d}\Sigma\,, \tag{2.2}$$

$$\int_{\partial\Sigma} \boldsymbol{H}\cdot\boldsymbol{\tau}\,\mathrm{d}\ell = \frac{\mathrm{d}}{\mathrm{d}t}\int_{\Sigma}\boldsymbol{D}\cdot\boldsymbol{\nu}\,\mathrm{d}\Sigma + \int_{\Sigma}\boldsymbol{j}\cdot\boldsymbol{\nu}\,\mathrm{d}\Sigma\,, \tag{2.3}$$

$$\int_{\partial\Omega} \boldsymbol{D}\cdot\boldsymbol{\nu}\,\mathrm{d}\Sigma = \int_{\Omega}\varrho\,\mathrm{d}\Omega\,, \tag{2.4}$$

$$\int_{\partial\Omega} \boldsymbol{B}\cdot\boldsymbol{\nu}\,\mathrm{d}\Sigma = 0\,, \tag{2.5}$$

where $\boldsymbol{\nu}$ and $\boldsymbol{\tau}$ are the unit normal and unit tangent to the surface, respectively, while $\boldsymbol{E}$ and $\boldsymbol{H}$ are the electric and magnetic field intensity with the corresponding fluxes $\boldsymbol{D}$ and $\boldsymbol{B}$ which are called, respectively, electric displacement and magnetic flux density or magnetic induction. The last two fields present in Maxwell equations are the charge density ϱ and the current density $\boldsymbol{j}$. If the surface Σ in (2.3) is considered as the boundary of the volume Ω, then it is a closed surface, *i.e.* it has no boundary $\partial\Sigma = \partial\partial\Omega = \emptyset$.

If we then combine (2.3) and (2.4), we obtain

$$0 = \frac{\mathrm{d}}{\mathrm{d}t}\int_{\Omega} \varrho \,\mathrm{d}\Omega + \int_{\partial\Omega} \boldsymbol{j}\cdot\boldsymbol{\nu}\,\mathrm{d}\Sigma\,,$$

which is the continuity equation for the electric charge.
If Ω and Σ are stationary with respect to the inertial reference frame of the field vectors and the fields are sufficiently smooth, Maxwell equations (2.2)−(2.5) can be written in the differential formulation

$$\begin{aligned} \mathbf{curl}\,\boldsymbol{E} &= -\partial_t \boldsymbol{B}\,, && (2.6)\\ \operatorname{div}\boldsymbol{D} &= \varrho\,, \\ \mathbf{curl}\,\boldsymbol{H} &= \boldsymbol{j} + \partial_t \boldsymbol{D}\,, && (2.7)\\ \operatorname{div}\boldsymbol{B} &= 0\,. && (2.8) \end{aligned}$$

Other quantities, that are often useful to describe electromagnetic phenomena, are the scalar and vector potentials. The existence of such potentials, as we will discuss later, depends on the topology of the domain Ω. For now, we will assume that such potentials exist, which is true, for example, if the domain Ω is contractible. From the fact that the magnetic flux density is solenoidal (2.8), we deduce that there exists a magnetic vector potential $\boldsymbol{A}$ such that

$$\boldsymbol{B} = \mathbf{curl}\,\boldsymbol{A}\,. \tag{2.9}$$

Substituting it in (2.6), by linearity of curl operator, we obtain

$$\mathbf{curl}\,(-\partial_t \boldsymbol{A} - \boldsymbol{E}) = \boldsymbol{0}$$

So, there exists a scalar electric potential ϕ such that

$$\mathbf{grad}\,\phi = -\partial_t \boldsymbol{A} - \boldsymbol{E}\,, \tag{2.10}$$

and therefore

$$\boldsymbol{E} = -\partial_t \boldsymbol{A} - \mathbf{grad}\,\phi\,.$$

In addition to Maxwell equations, at a macroscopic level the constitutive relations must be considered, which relate the fluxes to the field intensities. These, in general, are nonlinear, non-homogeneous, anisotropic relations which might depend on various quantities such as, for example, time, current density and temperature. However, in this work, we deal only with simple material laws satisfying the following assumptions

Assumption 2.2. *We assume the material laws to be in the following form*

$$\boldsymbol{B} = \mu(\boldsymbol{x})\boldsymbol{H}\,, \qquad \boldsymbol{D} = \epsilon(\boldsymbol{x})\boldsymbol{E}\,, \qquad \boldsymbol{j} = \boldsymbol{\sigma}(\boldsymbol{x})\boldsymbol{E} + \boldsymbol{j}_0\,,$$

where μ and ϵ are called, respectively, permeability and permittivity while σ is the electric conductivity and $\boldsymbol{j}_0$ is an impressed current. Moreover, we assume the following bounds for the material parameters:

$$\begin{aligned} 0 < \epsilon_0 \le \epsilon(\boldsymbol{x}) \le \epsilon_1 < \infty\,, &\qquad \text{in } \Omega\,,\\ 0 < \mu_0 \le \mu(\boldsymbol{x}) \le \mu_1 < \infty\,, &\qquad \text{in } \Omega\,,\\ 0 \le \sigma(\boldsymbol{x}) \le \sigma_1 < \infty\,, &\qquad \text{in } \Omega\,. \end{aligned}$$

2.1.1 Time-harmonic equations

For certain types of problems, including the one that will be treated in Section 5.2, it is useful to assume the fields to be time-harmonic [Mon+03, Section 1.2], *i.e.*

Assumption 2.3. *The fields are assumed to have the following sinusoidal time dependence*

$$\begin{aligned} f(\boldsymbol{x},\, t) &= \Re\Big(\widehat{f}(\boldsymbol{x})\, e^{-i\omega t}\Big)\,,\\ \boldsymbol{f}(\boldsymbol{x},\, t) &= \Re\Big(\widehat{\boldsymbol{f}}(\boldsymbol{x})\, e^{-i\omega t}\Big)\,. \end{aligned} \tag{2.11}$$

where the quantities with the hat are complex-valued functions of the position and $\omega > 0$.

With Assumption 2.3, the derivation with respect to time amounts to multiplying the complex function (denoted with a hat) by a factor $-i\omega$, *i.e.*

$$\partial_t = -i\omega\,.$$

Considering the Assumption 2.3, from the Maxwell equation, it is possible to deduce relations between the complex-valued fields. To simplify the exposition, we will drop the hat and consider the fields in the form (2.11), at a specific ω, as complex-valued. The differential form of the Maxwell equations in frequency domain (with time-harmonic fields) is

$$\mathbf{curl}\,\boldsymbol{E} = i\omega\,\boldsymbol{B}\,, \tag{2.12}$$

$$\operatorname{div}\boldsymbol{D} = \varrho\,, \tag{2.13}$$

$$\mathbf{curl}\,\boldsymbol{H} = \boldsymbol{j} - i\omega\,\boldsymbol{D}\,, \tag{2.14}$$

$$\operatorname{div}\boldsymbol{B} = 0\,.$$

Using the Assumption 2.2 on the material laws, we can further manipulate the Maxwell equations: taking the curl of equation (2.12), using (2.14) and assuming the absence of currents, we obtain

$$\mathbf{curl}\left(\mu^{-1}\,\mathbf{curl}\,\boldsymbol{E}\right) = \omega^2\,\mathbf{curl}\,\boldsymbol{E}\,. \tag{2.15}$$

A similar equation for the magnetic field can be obtained repeating the analogous steps on equation (2.7)

$$\mathbf{curl}\left(\epsilon^{-1}\,\mathbf{curl}\,\boldsymbol{H}\right) = \omega^2\,\mathbf{curl}\,\boldsymbol{H}\,. \tag{2.16}$$

Considering instead the potentials (2.9) and (2.10), from (2.13), we obtain

$$i\omega(\operatorname{div}(\epsilon\boldsymbol{A})) - \operatorname{div}(\epsilon\,\mathbf{grad}\,\phi) = \varrho \tag{2.17}$$

and from (2.7), we deduce

$$\mathbf{curl}\left(\mu^{-1}\,\mathbf{curl}\,\boldsymbol{A}\right) = \boldsymbol{j} + \omega^2\,\epsilon\boldsymbol{A} + i\omega\,\epsilon(\mathbf{grad}\,\phi)\,. \tag{2.18}$$

2.1.2 Stationary regime

In the stationary regime, which amounts to considering the limit $\omega \to 0$, the electric and magnetic quantities, together with the corresponding Maxwell equations, decouple. In this case we can describe $\boldsymbol{E}$ and $\boldsymbol{D}$ just in terms of the electric scalar potential ϕ: from equation (2.10) we can immediately see that

$$\boldsymbol{E} = -\,\mathbf{grad}\,\phi$$

and, from (2.17), we obtain the following equation for electrostatics:

$$-\operatorname{div}(\epsilon\,\mathbf{grad}\,\phi) = \varrho\,.$$

Similarly, the magnetic quantities $\boldsymbol{H}$ and $\boldsymbol{B}$ can be described just in terms of the vector potential $\boldsymbol{A}$. In fact, equation (2.18) becomes

$$\begin{aligned} &\mathbf{curl}\left(\mu^{-1}\,\mathbf{curl}\,\boldsymbol{A}\right) = \boldsymbol{j}\,,\\ &\operatorname{div}(\epsilon\boldsymbol{A}) = 0\,, \end{aligned} \tag{2.19}$$

where the second equation is an additional constraint which corresponds to the choice of a particular gauge, called Coulomb gauge [Jac07, Section 6.3]. We will see in the following section that the Coulomb gauge will be useful to ensure the uniqueness of the solution. If, in addition to the stationarity assumption, no currents are present, we can see from (2.7) that $\boldsymbol{H}$ is irrotational and, therefore, there exists also a magnetic scalar potential ψ such that

$$\boldsymbol{H} = -\,\mathbf{grad}\,\psi \tag{2.20}$$

and equation (2.8) leads to

$$-\operatorname{div}(\mu\,\mathbf{grad}\,\psi) = 0\,. \tag{2.21}$$

2.1.3 Interface conditions

Let us now consider a domain Ω divided by a surface Σ, whose orientation is determined by a choice of the unit normal ν, into two regions. We indicate with the subscript 1 and 2 the two distinct regions Ω_1 and Ω_2, corresponding, respectively, to negative and positive values of the unit normal. We consider a different material for each region, characterized by (ϵ_1, μ_1) and (ϵ_2, μ_2), and we would like to understand how the fields behave near the interface Σ. For this purpose we will indicate with the different subscripts the limit values for the fields, *e.g.*

$$E_1 = \lim_{\delta \to 0^+} E(\boldsymbol{x}_0 - \delta \boldsymbol{\nu}) \quad \text{and} \quad E_2 = \lim_{\delta \to 0^+} E(\boldsymbol{x}_0 + \delta \boldsymbol{\nu}) \,, \quad \boldsymbol{x}_0 \in \Sigma \,.$$

Considering a volume and a surface crossing the interface Σ, from the integral formulation (2.2)−(2.5), it is possible to obtain interface conditions for the field intensities [Mon+03, Section 1.5], which read

$$\begin{aligned} \boldsymbol{\nu} \times (\boldsymbol{E}_2 - \boldsymbol{E}_1) &= \boldsymbol{0} \,, & \boldsymbol{\nu} \cdot (\mu_2 \boldsymbol{H}_2 - \mu_1 \boldsymbol{H}_1) &= \boldsymbol{0} \,, \\ \boldsymbol{\nu} \times (\boldsymbol{H}_2 - \boldsymbol{H}_1) &= \boldsymbol{j}_\Sigma \,, & \boldsymbol{\nu} \cdot (\epsilon_2 \boldsymbol{E}_2 - \epsilon_1 \boldsymbol{E}_1) &= \varrho_\Sigma \,, \end{aligned}$$

where $\boldsymbol{j}_\Sigma$ and ϱ_Σ are the surface current density and surface charge density on Σ, respectively. If we consider the material associated to Ω_2 to be a Perfect Electric Conductor (PEC) we have the following conditions [Jac07, Section 5.13]:

$$\begin{aligned} \boldsymbol{\nu} \times \boldsymbol{E}_1 &= \boldsymbol{0} \,, & \epsilon_1 \boldsymbol{E}_1 \cdot \boldsymbol{\nu} &= \rho_\Sigma \,, \\ \boldsymbol{\nu} \times \boldsymbol{H}_1 &= \boldsymbol{j}_\Sigma \,, & \mu_1 \boldsymbol{H}_1 \cdot \boldsymbol{\nu} &= 0 \,. \end{aligned}$$

Similarly, we can assume a material associated to $\boldsymbol{H}_2$ to be a Perfect Magnetic Conductor (PMC) and obtain that [Jac07, Section 5.8]

$$\boldsymbol{\nu} \times \boldsymbol{H}_1 = \boldsymbol{0} \,.$$

It is customary to specify the boundary conditions in terms of PEC and PMC instead of Dirichlet, Neumann or Robin. This is a consequence of the fact that PEC and PMC are associated to the physics of the problem, while the use of Dirichlet or Neumann boundary conditions depends on the formulation used to describe the field. For example, the use of PEC corresponds to a Dirichlet boundary condition for an $\boldsymbol{E}$-formulation (2.15) and to a Neumann boundary condition for a $\boldsymbol{H}$-formulation (2.16).

2.2 Variational formulations

In this section, we will introduce the variational formulation of the Maxwell equations. We will describe the functional spaces involved and the relations

between them by means of the de Rham complex. This approach is useful to specify the conditions for the well-posedness of boundary value problems that arise in electromagnetism and to derive appropriate numerical methods for their solution applying the Galerkin approach. The general theory is developed in the context of Riemannian manifolds with the use of differential forms, but, to simplify the exposition, we will present the concepts in the standard three-dimensional Euclidean space with Cartesian coordinates. Additional material can be found, for example in [Arn18], [Lic19]. Despite the fact that we will also apply the framework to the electromagnetic field complex coefficients described in Assumption 2.3, for simplicity we will develop the concepts in the setting of real-valued functions.

2.2.1 Sobolev spaces

Let Ω be a bounded Lipschitz domain in $\mathbb{R}^3$ and let its boundary $\partial\Omega = \overline{\Sigma}_D \cup \overline{\Sigma}_N$, where Σ_D and $\Sigma_N = \partial\Omega \setminus \overline{\Sigma}_D$ are relatively open subsets, *i.e.* there exist two open subsets of $\mathbb{R}^3$, U_D and U_N, such that $\Sigma_D = U_D \cap \partial\Omega$ and $\Sigma_N = U_N \cap \partial\Omega$ [KF75, Section 9.2], and $\Sigma_I = \overline{\Sigma}_D \cap \overline{\Sigma}_N$ can be represented locally as the graph of a Lipschitz function [Lic19]. We start defining the Hilbert spaces of square integrable scalar and vector-valued functions as

$$
\begin{aligned}
L^2(\Omega) &= \left\{ u : \int_\Omega u^2 \,\mathrm{d}\Omega < \infty \right\}, \\
L^2(\Omega;\mathbb{R}^3) &= \left\{ \boldsymbol{u} : \int_\Omega \|\boldsymbol{u}\|_e^2 \,\mathrm{d}\Omega < \infty \right\},
\end{aligned}
$$

with the corresponding inner products

$$
(u,\, v)_{L^2(\Omega)} = \int_\Omega uv \,\mathrm{d}\Omega\,, \qquad (\boldsymbol{u},\, \boldsymbol{v})_{L^2(\Omega;\mathbb{R}^3)} = \int_\Omega \boldsymbol{u}\cdot\boldsymbol{v} \,\mathrm{d}\Omega\,,
$$

where $\|\boldsymbol{u}\|_e = \sqrt{\boldsymbol{u}\cdot\boldsymbol{u}}$ is the standard Euclidean norm. On such spaces we consider the standard differential operators, to be interpreted in the weak sense, that are present in the differential formulation of the Maxwell equations (2.6)-(2.8)

$$
\begin{aligned}
\mathbf{grad}\, u &= \begin{bmatrix} \partial_x u \\ \partial_y u \\ \partial_z u \end{bmatrix}, \quad \mathbf{curl}\, \boldsymbol{u} = \begin{bmatrix} \partial_y u_z - \partial_z u_y \\ \partial_z u_x - \partial_x u_z \\ \partial_x u_y - \partial_y u_x \end{bmatrix}, \\
\operatorname{div} \boldsymbol{u} &= \partial_x u_x + \partial_y u_y + \partial_z u_z\,,
\end{aligned}
$$

whose domains are the following Hilbert spaces:

$$\begin{aligned} H^1(\Omega) &= \left\{u \in L^2(\Omega) \,:\, \mathbf{grad}\, u \in L^2(\Omega;\mathbb{R}^3)\right\}, \\ H(\mathbf{curl};\Omega) &= \left\{\boldsymbol{u} \in L^2(\Omega;\mathbb{R}^3) \,:\, \mathbf{curl}\, \boldsymbol{u} \in L^2(\Omega;\mathbb{R}^3)\right\}, \\ H(\mathrm{div};\Omega) &= \left\{\boldsymbol{u} \in L^2(\Omega;\mathbb{R}^3) \,:\, \mathrm{div}\, \boldsymbol{u} \in L^2(\Omega)\right\}. \end{aligned} \tag{2.22}$$

The corresponding inner products are

$$\begin{aligned} (u,\, v)_{H^1(\Omega)} &= (u,\, v)_{L^2(\Omega)} + (\mathbf{grad}\, u,\, \mathbf{grad}\, v)_{L^2(\Omega;\mathbb{R}^3)}, \\ (\boldsymbol{u},\, \boldsymbol{v})_{H(\mathbf{curl};\Omega)} &= (\boldsymbol{u},\, \boldsymbol{v})_{L^2(\Omega;\mathbb{R}^3)} + (\mathbf{curl}\, \boldsymbol{u},\, \mathbf{curl}\, \boldsymbol{v})_{L^2(\Omega;\mathbb{R}^3)}, \\ (\boldsymbol{u},\, \boldsymbol{v})_{H(\mathrm{div};\Omega)} &= (\boldsymbol{u},\, \boldsymbol{v})_{L^2(\Omega;\mathbb{R}^3)} + (\mathrm{div}\, \boldsymbol{u},\, \mathrm{div}\, \boldsymbol{v})_{L^2(\Omega)}. \end{aligned} \tag{2.23}$$

The definitions (2.22) can be generalized to the case of spaces with boundary conditions defined on Σ_D:

$$\begin{aligned} H^1_{\Sigma_D}(\Omega) &= \left\{u \in H^1(\Omega) \,:\, (\mathrm{tr}\, u)|_{\Sigma_D} = 0\right\}, \\ H_{\Sigma_D}(\mathbf{curl};\Omega) &= \left\{\boldsymbol{u} \in H(\mathbf{curl};\Omega) \,:\, (\gamma_{\boldsymbol{\tau}}\, \boldsymbol{u})|_{\Sigma_D} = \mathbf{0}\right\}, \\ H_{\Sigma_D}(\mathrm{div};\Omega) &= \left\{\boldsymbol{u} \in H(\mathrm{div};\Omega) \,:\, (\gamma_{\boldsymbol{\nu}}\, \boldsymbol{u})|_{\Sigma_D} = 0\right\}. \end{aligned} \tag{2.24}$$

where the trace operators, for smooth enough functions, coincide with the evaluation on the boundary of the function itself, its tangential component (previously rotated clockwise by an angle of $\pi/2$) or its normal component, respectively [Mon+03, Section 3.2.1, 3.5.3, 3.5.3]:

$$\begin{aligned} (\mathrm{tr}\, u)|_{\Sigma_D} &= u|_{\Sigma_D}, & u &\in C^1(\overline{\Omega}), \\ (\gamma_{\boldsymbol{\tau}}\, \boldsymbol{u})|_{\Sigma_D} &= \boldsymbol{u}|_{\Sigma_D} \times \boldsymbol{\nu}, & \boldsymbol{u} &\in C^1(\overline{\Omega};\mathbb{R}^3), \\ (\gamma_{\boldsymbol{\nu}}\, \boldsymbol{u})|_{\Sigma_D} &= \boldsymbol{u}|_{\Sigma_D} \cdot \boldsymbol{\nu}, & \boldsymbol{u} &\in C^1(\overline{\Omega};\mathbb{R}^3). \end{aligned}$$

We then introduce the more regular Sobolev spaces

$$H^s(\Omega) = \left\{ u \in L^2(\Omega) : \sum_{|\boldsymbol{\alpha}| \le s} \partial_{\boldsymbol{\alpha}} u \in L^2(\Omega) \right\}, \tag{2.25}$$

where s is an integer and $\boldsymbol{\alpha}$ is a multi-index and the derivatives should always be interpreted in the weak sense. The corresponding seminorms and norms are

$$|u|_{H^s(\Omega)} = \sum_{|\alpha|=s} \|\partial_{\boldsymbol{\alpha}} u\|_{L^2(\Omega)}, \quad \|u\|_{H^s(\Omega)} = \sum_{k=0}^{s} |u|_{H^s(\Omega)}.$$

A more regular class of spaces can be defined analogously to (2.22), using, instead of L^2, the Sobolev spaces (2.25)

$$H^s(\mathbf{curl};\,\Omega) = \left\{\boldsymbol{u} \in H^s(\Omega;\,\mathbb{R}^3) \,:\, \mathbf{curl}\,\boldsymbol{u} \in H^s(\Omega;\,\mathbb{R}^3)\right\},$$
$$H^s(\mathrm{div};\,\Omega) \;\; = \left\{\boldsymbol{u} \in H^s(\Omega;\,\mathbb{R}^3) \,:\, \mathrm{div}\,\boldsymbol{u} \in H^s(\Omega)\right\}.$$

In the following we will often avoid to indicate the domain Ω to simplify the notation.

2.2.2 The de Rham complex

The spaces (2.24), which we will use to write the variational formulation of the Maxwell equations, form a so called de Rham complex. In the following, we will present the material mainly following [Arn18], in which this framework has been introduced considering only the cases $\Sigma_D = \emptyset$ or $\Sigma_D = \partial\Omega$. Another presentation, closely related to electromagnetic problems, can be found in [Mon+03, Section 3.7]. Finally, for the specific results concerning mixed boundary conditions, we refer to [Lic19, Section 7]. The de Rham complex considered in this work is represented by the following sequence:

$$0 \longrightarrow H^1_{\Sigma_D} \xrightarrow{\mathbf{grad}} H_{\Sigma_D}(\mathbf{curl}) \xrightarrow{\mathbf{curl}} H_{\Sigma_D}(\mathrm{div}) \xrightarrow{\mathrm{div}} L^2 \longrightarrow 0 \tag{2.26}$$

Each arrow corresponds to a linear operator which maps a space into the subsequent one. The first arrow is associated to the inclusion of the identically null function and the last arrow to the operator that maps each element to the identically null function. The de Rham complex is a cochain complex [Arn18, Section 2.5], which is a sequence of vector spaces V^k and a set of linear operators $d^k : V^k \to V^{k+1}$ for which the sequence is closed, *i.e.* $d^{k+1} \circ d^k = 0$. For the particular case of the de Rham complex in Cartesian coordinates, the V^k spaces, $k = 0, \ldots, 3$ are

$$V^0 = H^1_{\Sigma_D}\,, \quad V^1 = H_{\Sigma_D}(\mathbf{curl})\,, \quad V^2 = H_{\Sigma_D}(\mathrm{div})\,, \quad V^3 = L^2\,. \tag{2.27}$$

and the differential operators are

$$d^0 = \mathbf{grad}, \quad d^1 = \mathbf{curl}, \quad d^2 = \mathrm{div}\;. \tag{2.28}$$

Different concepts and quantities that we will introduce are not just valid for the specific spaces (2.24), but have a broader validity in the framework of complexes whose vector spaces are Hilbert spaces. It is therefore convenient to work with the general notation used in (2.27)-(2.28). Defining $W^0 =$

$W^3 = L^2(\Omega)$ and $W^1 = W^2 = L^2(\Omega; \mathbb{R}^3)$, we have that $V^k \subset W^k$ and their inner products (2.23) can be expressed as

$$(u,\, v)_{V^k} = (u,\, v)_{W^k} + (d^k u,\, d^k v)_{W^{k+1}}\,.$$

In the following, we will often drop the subscripts associated to the W^k (L^2) inner product and the related quantities, such as the induced norm and the orthogonality with respect to it. We will instead keep the subscript when the quantities are referred to the spaces V^k. The sequence (2.26) can be written as

$$0 \longrightarrow V^0 \xrightarrow{d^0} V^1 \xrightarrow{d^1} V^2 \xrightarrow{d^2} V^3 \longrightarrow 0$$

To each space V^k in the sequence are associated three subspaces: the kernel of the operator acting on it $\mathfrak{Z}^k = \ker(d^k)$, the range of the previous operator in the sequence $\mathfrak{B}^k = \text{range}(d^{k-1})$ and the space of harmonic forms $\mathfrak{H}^k = \mathfrak{Z}^k \cap \mathfrak{B}^{k\perp}$ [Arn18, Section 4.2]. In the case of the Cartesian coordinates, we have that

$$\begin{aligned}
&\mathfrak{Z}^0 = \left\{u \in H^1_{\Sigma_D} \,:\, \mathbf{grad}\, u = \mathbf{0}\right\}, && \mathfrak{B}^0 = \{u \equiv 0\}\,,\\
&\mathfrak{Z}^1 = \{\boldsymbol{u} \in H_{\Sigma_D}(\mathbf{curl}) \,:\, \mathbf{curl}\, \boldsymbol{u} = \mathbf{0}\}\,, && \mathfrak{B}^1 = \left\{\boldsymbol{u} = \mathbf{grad}\, v, v \in H^1_{\Sigma_D}\right\},\\
&\mathfrak{Z}^2 = \{\boldsymbol{u} \in H_{\Sigma_D}(\mathrm{div}) \,:\, \mathrm{div}\, \boldsymbol{u} = 0\}\,, && \mathfrak{B}^2 = \{\boldsymbol{u} = \mathbf{curl}\, \boldsymbol{v}, \boldsymbol{v} \in H_{\Sigma_D}(\mathbf{curl})\}\,,\\
&\mathfrak{Z}^3 = L^2\,, && \mathfrak{B}^3 = \{u = \mathrm{div}\, \boldsymbol{v}, \boldsymbol{v} \in H_{\Sigma_D}(\mathrm{div})\}\,.
\end{aligned}$$

It can be shown that each operator in the sequence has closed range, *i.e.* $\mathfrak{B}^k$ is a closed subspace of W^k, and that the dimension of the space of harmonic forms is finite and is determined by the topology of the domain and of its boundary [Lic19, Section 7.1]. In this context, the Poincaré-Friedrichs inequalities [Arn18, Theorem 4.6] hold

$$\|u\|_{V^k} \leq c_P \|d^k u\|, \quad u \in \mathfrak{Z}^{k,\perp_{V^k}}\,,$$

where $c_P > 0$ is independent of u. As already discussed, the sequence (2.26) is closed, meaning that the composition of two consecutive operators maps each element to the null space, *i.e.* $\mathfrak{B}^k \subset \mathfrak{Z}^k$. Considering the complex in Cartesian coordinates, the parts involving null functions are trivial and we have that

$$\begin{aligned}
\mathbf{curl}\,(\mathbf{grad}\, u) &\equiv \mathbf{0}\,, \quad u \in H^1_{\Sigma_D}\,,\\
\mathrm{div}\,(\mathbf{curl}\, \boldsymbol{u}) &\equiv 0\,, \quad \boldsymbol{u} \in H_{\Sigma_D}(\mathbf{curl})\,.
\end{aligned}$$

The sequence is called exact if also the converse holds, in other words if $\mathfrak{B}^k \supset \mathfrak{Z}^k$ and so, if $\mathfrak{B}^k = \mathfrak{Z}^k$ [Arn18, Section 2.2]. Associated to the complex (2.26), there is its dual complex (V_k^*, d_k^*),

$$0 \longleftarrow V_0^* \xleftarrow{d_1^*} V_1^* \xleftarrow{d_2^*} V_2^* \xleftarrow{d_3^*} V_3^* \longleftarrow 0$$

which involves spaces with boundary conditions imposed on the complementary part of the domain Σ_N and the operators d_k^*, which are the adjoints of d^{k-1}:

$$d_k^* u \in V_k^* : (d_k^* u,\, v)_{W^{k-1}} = (u,\, d^{k-1} v)_{W^k}\,, \qquad v \in V^{k-1}\,.$$

In our case, we have that $d_1^* = -\operatorname{div}$, $d_2^* = \mathbf{curl}$, $d_3^* = -\mathbf{grad}$ and

$$V_0^* = L^2\,, \quad V_1^* = H_{\Sigma_N}(\operatorname{div})\,, \quad V_2^* = H_{\Sigma_N}(\mathbf{curl})\,, \quad V_3^* = H^1_{\Sigma_N}\,.$$

The dual complex of (2.26) is then given by

$$0 \longleftarrow L^2 \xleftarrow{-\operatorname{div}} H_{\Sigma_N}(\operatorname{div}) \xleftarrow{\mathbf{curl}} H_{\Sigma_N}(\mathbf{curl}) \xleftarrow{-\mathbf{grad}} H^1_{\Sigma_N} \longleftarrow 0$$

The dual complex has the same properties as the original one. It is possible to introduce the analogous subspaces $\mathfrak{Z}_k^*$, $\mathfrak{B}_k^*$ and to show that, since the operators have closed range,

$$\mathfrak{Z}_k^* = \mathfrak{B}^{k,\perp}\,, \qquad \mathfrak{B}_k^* = \mathfrak{Z}^{k,\perp}$$

and, consequently, the space of harmonic forms is equal for the two complexes: $\mathfrak{H}^k = \mathfrak{Z}^k \cap \mathfrak{Z}_k^*$,

$$\begin{aligned}
\mathfrak{H}^0 &= \left\{u \in H^1_{\Sigma_D}(\Omega) :\ \mathbf{grad}\, u = 0\right\},\\
\mathfrak{H}^1 &= \left\{\boldsymbol{u} \in H_{\Sigma_D}(\Omega;\, \mathbf{curl}) \cap H_{\Sigma_N}(\Omega;\, \operatorname{div}) :\ \mathbf{curl}\, \boldsymbol{u} = \mathbf{0},\, \operatorname{div} \boldsymbol{u} = \mathbf{0}\right\},\\
\mathfrak{H}^2 &= \left\{\boldsymbol{u} \in H_{\Sigma_D}(\Omega;\, \operatorname{div}) \cap H_{\Sigma_N}(\Omega;\, \mathbf{curl}) :\ \mathbf{curl}\, \boldsymbol{u} = \mathbf{0},\, \operatorname{div} \boldsymbol{u} = \mathbf{0}\right\},\\
\mathfrak{H}^2 &= \left\{u \in H^1_{\Sigma_N}(\Omega) :\ \mathbf{grad}\, u = 0\right\}.
\end{aligned}$$

The structure introduced above is especially useful to treat problems in electromagnetism thanks to the Helmholtz (or Hodge) decomposition, which states that each V^k and W^k space can be decomposed in orthogonal subspaces [Arn18, Theorem 4.5]

$$\begin{aligned}
W^k &= \mathfrak{B}^k \oplus \mathfrak{H}^k \oplus \mathfrak{Z}^{k,\perp} = \mathfrak{B}^k \oplus \mathfrak{H}^k \oplus \mathfrak{Z}_k^*\,, \\
V^k &= \mathfrak{B}^k \oplus \mathfrak{H}^k \oplus \mathfrak{Z}^{k,\perp_{V^k}}\,.
\end{aligned} \tag{2.29}$$

We can see that the sequence is exact if the spaces of harmonic forms vanish. The Hodge decomposition (2.29) for a function $f \in W^k$ can be obtained by solving the abstract Hodge Laplacian problem, which, expressed using the mixed weak formulation, reads

Problem 2.1. *Find $\sigma \in V^{k-1}$, $u \in V^k$ and $p \in \mathfrak{H}^k$ such that*

$$\begin{aligned} (\sigma,\, \tau) - (u,\, d^{k-1}\tau) &= 0\,, & \tau &\in V^{k-1}\,,\\ (d^{k-1}\sigma,\, v) - (d^k u,\, d^k v) + (p,\, v) &= (f,\, v)\,, & v &\in V^k\,,\\ (u,\, q) &= 0\,, & q &\in \mathfrak{H}^k\,. \end{aligned} \tag{2.30}$$

The well-posedness of Problem 2.1 and of a wider class of problems we will encounter rely on the following Theorem [Arn18, Theorem 4.9]:

Theorem 2.1. *Let $U = V^{k-1} \times V^k \times \mathfrak{H}^k$ and let $B : U \times U \to \mathbb{R}$ be the following bilinear form*

$$\begin{aligned} B(\sigma,\, u,\, p;\, \tau,\, v,\, q) = {} & (\sigma,\, \tau) - (u,\, d^{k-1}\tau)\\ & - (d^{k-1}\sigma,\, v) - (d^k u,\, d^k v) - (p,\, v)\\ & - (u,\, q)\,. \end{aligned} \tag{2.31}$$

Then, (2.31) satisfies the inf-sup condition with constant $\gamma > 0$ depending only on the Poincaré constant c_P:

$$\gamma = \inf_{0 \neq x \in U} \sup_{0 \neq y \in U} \frac{B(x,\, y)}{\|x\|_U \, \|y\|_U}\,.$$

It is easy to check that the bilinear form is also continuous so, for any $F \in U'$ there exists a unique solution $x \in U$ of the problem [Neč62, Theorem 3.1]

$$B(x,\, y) = F(y)\,, \quad y \in U \tag{2.32}$$

and we have that

$$\|x\|_U \leq \gamma^{-1} \, \|F\|_{U'}\,.$$

In order to be able to take into account the material parameters, we need to introduce a slight generalization [AFW10, Section 6.1], [Arn18, Section 8.2]. Considering as weights a set of scalar functions bounded from below and from above

$$0 < \alpha_i^{min} \leq \alpha_i \leq \alpha_i^{max} < \infty\,, \quad i = k-1,\, k,\, k+1\,,$$

we have that the standard L^2 spaces W^k are equivalent to the weighted ones W^k_α defined using the following inner products:

$$(w_1,\, w_2)_{\alpha_k} = (\alpha_k \, w_1,\, w_2)\,.$$

Due to the equivalence between the weighted and unweighted spaces, all the arguments presented above are still valid, with the exception of the definition

of the adjoint operators and of the dual spaces, that should account for the weights [AFW10, Section 6.1], *i.e.*

$$\begin{aligned}(\mathbf{grad}^*)\boldsymbol{u} &= -\alpha_0^{-1}\operatorname{div}(\alpha_1\boldsymbol{u}),\\ (\mathbf{curl}^*)\boldsymbol{u} &= \alpha_1^{-1}\,\mathbf{curl}(\alpha_2\boldsymbol{u}),\\ (\operatorname{div}^*)\boldsymbol{u} &= -\alpha_2^{-1}\,\mathbf{grad}(\alpha_3\boldsymbol{u}).\end{aligned}$$

Moreover, if the sequence considered is exact, *i.e.* there are no harmonic forms, the problem (2.32) can be simplified removing the last equation and the term associated to p. In this case, considering the weighted L^2 norms, we have the following continuous bilinear form satisfying the inf-sup condition:

$$\begin{aligned}B(\sigma,\, u;\, \tau,\, v) = (\sigma,\, \tau)_{\alpha_{k-1}} - (u,\, d^{k-1}\tau)_{\alpha_k}\\ - (d^{k-1}\sigma,\, v)_{\alpha_k} - (d^k u,\, d^k v)_{\alpha_{k+1}}.\end{aligned} \tag{2.33}$$

As already mentioned, the dimension of the space of harmonic forms depends, not only on the topology of the domain Ω, but also on its boundary Σ_D. For example, consider the contractible domain given by the cube $\Omega = (0,\,1)^3$, where Σ_D is given by the two opposite faces at $x = 0$ and $x = 1$. In this case, we have that the function $\boldsymbol{u} = (1,\,0,\,0)^T \in H_{\Sigma_D}(\Omega;\,\mathbf{curl}) \cap H_{\Sigma_N}(\Omega;\,\operatorname{div})$. Moreover, we have that $\mathbf{curl}\,\boldsymbol{u} = \mathbf{0}$, $\operatorname{div}\boldsymbol{u} = 0$ and so $\boldsymbol{u} \in \mathfrak{H}^1$.

Three-dimensional Cartesian complexes

In the following, we will assume that Ω is contractible and either $\Sigma_D = \emptyset$ or $\Sigma_D = \partial\Omega$ or the boundary conditions do not introduce any harmonic forms (exact sequence). For a detailed discussion about the argument, see *e.g.* [Lic19]. If $\Sigma_D = \emptyset$, the only non-vanishing harmonic space is $\mathfrak{H}^0$, whose dimension is one. Analogously if $\Sigma_D = \partial\Omega$ the only non-vanishing harmonic space is $\mathfrak{H}^3$, whose dimension is one. In these two cases, we can recover exactness introducing two slightly modified sequences: for $\Sigma_D = \emptyset$, the following sequence is exact,

$$\mathbb{R} \longrightarrow H^1 \xrightarrow{\mathbf{grad}} H(\mathbf{curl}) \xrightarrow{\mathbf{curl}} H(\operatorname{div}) \xrightarrow{\operatorname{div}} L^2 \longrightarrow 0 \tag{2.34}$$

while for $\Sigma_D = \partial\Omega$ the exact sequence is

$$0 \longrightarrow H^1_{\partial\Omega} \xrightarrow{\mathbf{grad}} H_{\partial\Omega}(\mathbf{curl}) \xrightarrow{\mathbf{curl}} H_{\partial\Omega}(\operatorname{div}) \xrightarrow{\operatorname{div}} L^2 \xrightarrow{\int_\Omega} \mathbb{R} \tag{2.35}$$

Exactness ensures the existence of potentials. For example, if a field $\boldsymbol{u} \in H(\mathbf{curl};\,\Omega)$ is irrotational, *i.e.* $\mathbf{curl}\,\boldsymbol{u} = \mathbf{0}$, then there exists a scalar potential

$v \in H^1(\Omega)$, defined up to constant functions (see sequence (2.34)), such that $\boldsymbol{u} = \mathbf{grad}\, v$. Similarly, for a field $\boldsymbol{u} \in H(\mathrm{div};\, \Omega)$ which is solenoidal, there exists a vector potential $\boldsymbol{v} \in H(\mathbf{curl};\, \Omega)$, defined up to gradient of scalar functions in H^1, such that $\boldsymbol{u} = \mathbf{curl}\, \boldsymbol{v}$.

Two-dimensional Cartesian complexes

We will now briefly introduce the de Rham complexes and spaces arising when a two-dimensional domain is considered. This particular case will be useful in the definition of the discrete spaces in axisymmetric domains that will be presented in Section 4.1.2. Consider a two-dimensional Lipschitz domain $S \subset \mathbb{R}^2$ and, for simplicity, no essential boundary conditions, *i.e.* the two-dimensional analogous of $\Sigma_D = \emptyset$. The relevant functional spaces in this case are defined as follows

$$\begin{aligned} Y^0 &= H^1(S) &&= \left\{u \in L^2(S) : \mathbf{grad}\, u \in L^2(S)\right\}, \\ Y^1 &= H(\mathrm{curl};\, S) &&= \left\{\boldsymbol{u} \in L^2(S;\, \mathbb{R}^2) : \mathrm{curl}\, \boldsymbol{u} \in L^2(S)\right\}, \\ Y^{1*} &= H(\mathrm{div};\, S) &&= \left\{\boldsymbol{u} \in L^2(S;\, \mathbb{R}^2) : \mathrm{div}\, \boldsymbol{u} \in L^2(S)\right\}, \\ Y^2 &= L^2(S) &&= \left\{u : \int_S u^2 < \infty\right\}. \end{aligned} \tag{2.36}$$

where **grad** and div are the standard gradient and divergence in Cartesian coordinates

$$\mathbf{grad}\, u = \begin{bmatrix} \partial_x u \\ \partial_y u \end{bmatrix}, \qquad \mathrm{div}\left(\begin{bmatrix} u_x \\ u_y \end{bmatrix}\right) = \partial_x u_x + \partial_y u_y$$

and curl denotes the scalar curl

$$\mathrm{curl}\left(\begin{bmatrix} u_x \\ u_y \end{bmatrix}\right) = \partial_x u_y - \partial_y u_x\,.$$

For functions in Y^0, it is also well-defined the operator

$$\mathbf{rot}(u) = \begin{bmatrix} \partial_y u \\ -\partial_x u \end{bmatrix} = \mathbf{P}(\mathbf{grad}(u))\,,$$

where the matrix $\mathbf{P}$ is the clockwise rotation by an angle of $\pi/2$, *i.e.*

$$\mathbf{P} = \begin{bmatrix} 0 & 1 \\ -1 & 0 \end{bmatrix}. \tag{2.37}$$

We will use the word rotor, or perpendicular gradient, to indicate **rot** and to avoid the confusion with the three-dimensional **curl**. In the two-dimensional

case, we have the following two shorter de Rham complexes which are isomorphic (see [BSV13, Theorem 5.5] in which the complexes with an analogous notation are introduced in the discrete setting):

$$\begin{array}{ccccccccc} \mathbb{R} & \longrightarrow & Y^0 & \xrightarrow{\mathbf{grad}} & Y^1 & \xrightarrow{\mathrm{curl}} & Y^2 & \longrightarrow & 0 \\ & & \updownarrow{\scriptstyle \mathrm{id}} & & \downarrow{\scriptstyle \mathbf{P}} & & \updownarrow{\scriptstyle \mathrm{id}} & & \\ \mathbb{R} & \longrightarrow & Y^0 & \xrightarrow{\mathbf{rot}} & Y^{1*} & \xrightarrow{\mathrm{div}} & Y^2 & \longrightarrow & 0 \end{array} \tag{2.38}$$

where the matrix $\mathbf{P}$ is defined in (2.37).

The two complexes with the corresponding differential operators can be seen as the result of the decomposition of the three-dimensional complex (2.34) when only constant functions along z are considered, *i.e.*

$$\mathbb{R} \longrightarrow f \xrightarrow{\mathbf{grad}} \begin{bmatrix} \boldsymbol{u}_{xy} \\ u_z \end{bmatrix} \xrightarrow{\mathrm{curl}} \begin{bmatrix} \boldsymbol{v}_{xy} \\ v_z \end{bmatrix} \xrightarrow{\mathrm{div}} g \longrightarrow 0 \tag{2.39}$$

(with $0 \to u_z$ and $\mathbf{rot} \to \boldsymbol{v}_{xy}$, $0 \to v_z$)

where

$$f \in Y^0, \quad \begin{bmatrix} \boldsymbol{u}_{xy} \\ u_z \end{bmatrix} \in Y^1 \times Y^0, \quad \begin{bmatrix} \boldsymbol{v}_{xy} \\ v_z \end{bmatrix} \in Y^{1*} \times Y^2 \quad \text{and} \quad g \in Y^2 \,.$$

For example, we have that

$$\mathbf{curl} \left(\begin{bmatrix} u_x(x,\, y) \\ u_y(x,\, y) \\ u_z(x,\, y) \end{bmatrix} \right) = \begin{bmatrix} \mathbf{rot}\,(u_z) \\ \mathrm{curl}\,(\boldsymbol{u}_{xy}) \end{bmatrix} .$$

2.2.3 Weak formulations

In the final part of this section, we consider again a three-dimensional domain Ω and boundary conditions that produce an exact sequence, which might include the extended ones (2.34)–(2.35), so that there will be no harmonic forms. In this setting we present the weak formulation for some of the problems introduced in Section 2.1, that will be then used in the chapter devoted to the applications, and we will show how the results of well-posedness can be deduced from the theory presented above.

Vector potential formulation

Consider the vector potential strong formulation for the magnetostatic problem (2.19)

$$\begin{aligned}
&\mathbf{curl}\left(\mu^{-1}\,\mathbf{curl}\,\boldsymbol{A}\right) = \boldsymbol{j}\,, && \text{in } \Omega\,,\\
&\operatorname{div}(\epsilon\boldsymbol{A}) = 0\,, && \text{in } \Omega\,,\\
&\left(\mu^{-1}\,\mathbf{curl}\,\boldsymbol{A}\right)\times\boldsymbol{\nu} = \boldsymbol{j}_\Sigma\,, && \text{on } \Sigma_N\,,\\
&\boldsymbol{A}\times\boldsymbol{\nu} = \mathbf{0}\,, && \text{on } \Sigma_D\,,\\
&(\epsilon\boldsymbol{A})\cdot\boldsymbol{\nu} = 0\,, && \text{on } \Sigma_N\,,\\
&\operatorname{div}(\epsilon\boldsymbol{A}) = 0\,, && \text{on } \Sigma_D\,,
\end{aligned} \tag{2.40}$$

where $\boldsymbol{j}$ and $\boldsymbol{j}_\Sigma$ are the current density and the surface currents, respectively, which we assume to be known. The fourth boundary condition corresponds to a homogeneous Dirichlet boundary condition which, in turn, corresponds to a vanishing normal component of the magnetic flux, $\boldsymbol{B}\cdot\boldsymbol{\nu} = 0$. Non-homogeneous Dirichlet boundary conditions can be imposed through a lifting [BR91, Section 1]. The bilinear form (2.33) involved for this problem is the one for $k = 1$ with weights $\alpha_0 \equiv 1$, $\alpha_1 = \epsilon$, $\alpha_2 = \mu^{-1}$ and the corresponding weak formulation reads

Problem 2.2. *Find* σ, $\boldsymbol{A} \in H^1_{\Sigma_D}(\Omega)\times H_{\Sigma_D}(\mathbf{curl};\,\Omega)$ *such that*

$$\begin{aligned}
&\int_\Omega (\mu^{-1}\,\mathbf{curl}\,\boldsymbol{A})\cdot\mathbf{curl}\,\boldsymbol{v} + \epsilon\,(\mathbf{grad}\,\sigma)\cdot\boldsymbol{v}\,\mathrm{d}\Omega\\
&\qquad = \int_\Omega \boldsymbol{j}\cdot\boldsymbol{v}\,\mathrm{d}\Omega - \int_{\Sigma_N}\boldsymbol{j}_\Sigma\cdot\gamma_T\,\boldsymbol{v}\,\mathrm{d}\Sigma\,, && \boldsymbol{v}\in H_{\Sigma_D}(\mathbf{curl})\,,\\
&\int_\Omega \sigma\tau - \epsilon\boldsymbol{A}\cdot\mathbf{grad}\,\tau\,\mathrm{d}\Omega = 0\,, && \tau\in H^1_{\Sigma_D}\,,
\end{aligned}$$

where $\gamma_T\,\boldsymbol{v}$ *is a well-defined tangential trace operator that, for smooth enough functions, satisfies*

$$\gamma_T\,\boldsymbol{v} = (\boldsymbol{\nu}\times\boldsymbol{v}|_{\Sigma_D})\times\boldsymbol{\nu}\,.$$

This problem is well-posed for any $\boldsymbol{j}\in L^2(\Omega)$, but the solution will be the one of (2.40), only if $\boldsymbol{j}$ and $\boldsymbol{j}_\Sigma$ satisfy some compatibility conditions. For example, from the continuity equation, since we are in the static case, we have that

$$\operatorname{div}\boldsymbol{j} = 0\,, \quad \text{in } \Omega$$

and, for the case $\boldsymbol{j}_\Sigma = \mathbf{0}$, we have that

$$\boldsymbol{j}\cdot\boldsymbol{\nu} = 0\,, \quad \text{on } \Sigma_N\,.$$

When $\boldsymbol{j}$ satisfies the compatibility conditions, we have that $\sigma = -\operatorname{div}(\epsilon \boldsymbol{A}) \equiv 0$. If $\Sigma_D \neq \emptyset$, the kernel of **grad** consists on only the zero function and we can drop the term (σ, τ) in Problem 2.2, leading to

Problem 2.3. *Find* σ, $\boldsymbol{A} \in H^1_{\Sigma_D}(\Omega) \times H_{\Sigma_D}(\mathbf{curl}; \Omega)$ *such that*

$$\begin{aligned} \int_\Omega (\mu^{-1} \mathbf{curl}\, \boldsymbol{A}) \cdot \mathbf{curl}\, \boldsymbol{v} + \epsilon\, (\mathbf{grad}\, \sigma) \cdot \boldsymbol{v}\, \mathrm{d}\Omega & \\ = \int_\Omega \boldsymbol{j} \cdot \boldsymbol{v}\, \mathrm{d}\Omega - \int_{\Sigma_N} \boldsymbol{j}_\Sigma \cdot \gamma_T\, \boldsymbol{v}\, \mathrm{d}\Sigma\,, & \quad \boldsymbol{v} \in H_{\Sigma_D}(\mathbf{curl})\,, \\ \int_\Omega \epsilon \boldsymbol{A} \cdot \mathbf{grad}\, \tau\, \mathrm{d}\Omega = 0\,, & \quad \tau \in H^1_{\Sigma_D}\,, \end{aligned}$$

This corresponds to imposing that $\epsilon \boldsymbol{A}$ is orthogonal to all the gradients of scalar functions in $H^1_{\Sigma_D}$ and, as in the previous case, if $\boldsymbol{j}$ and $\boldsymbol{j}_\Sigma$ satisfy the compatibility conditions, we have that $\sigma \equiv 0$.

Magnetic scalar potential formulation

Another class of problems arises when, in addition to the previous hypothesis, we consider a current-free region. In this case, we can reformulate the magnetostatic problem in terms of the magnetic scalar potential (2.21) [Jac07, Section 5.4]

$$\begin{aligned} \operatorname{div}(\mu\, \mathbf{grad}\, \psi) = 0\,, & \quad \text{in } \Omega\,, \\ \psi = 0\,, & \quad \text{on } \Sigma_D\,, \\ (\mu\, \mathbf{grad}\, \psi) \cdot \boldsymbol{\nu} = \boldsymbol{B} \cdot \boldsymbol{\nu}\,, & \quad \text{on } \Sigma_N\,, \end{aligned}$$

where $\boldsymbol{B} \cdot \boldsymbol{\nu}$ is the normal component of the magnetic flux which we assume to be known. The associated bilinear form (2.33) can be obtained considering $k = 0$ with weights $\alpha_0 \equiv 1$, $\alpha_1 = \mu$. In the case $\Sigma_D = \emptyset$ the problem reads

Problem 2.4. *Find* σ, $\psi \in \mathbb{R} \times H^1_{\Sigma_D}(\Omega)$ *such that*

$$\begin{aligned} \int_\Omega (\mu\, \mathbf{grad}\, \psi) \cdot \mathbf{grad}\, v + \sigma v\, \mathrm{d}\Omega = \int_{\Sigma_N} (\boldsymbol{B} \cdot \boldsymbol{\nu}) v\, \mathrm{d}\Sigma\,, & \quad v \in H^1_{\Sigma_D}\,, \\ \int_\Omega \sigma - \psi\, \mathrm{d}\Omega = 0\,, & \end{aligned} \tag{2.41}$$

where the second equation in (2.41) is simpler since the space of σ is just the space of constant functions $\mathbb{R}$. Similarly to the previous case, we can drop the term in the second equation and write the formulation

Problem 2.5. *Find* σ, $\psi \in \mathbb{R} \times H^1_{\Sigma_D}(\Omega)$ *such that*

$$\int_\Omega (\mu \,\mathbf{grad}\, \psi) \cdot \mathbf{grad}\, v + \sigma v \,\mathrm{d}\Omega = \int_{\Sigma_N} (\boldsymbol{B} \cdot \boldsymbol{\nu}) v \,\mathrm{d}\Sigma\,, \quad v \in H^1_{\Sigma_D}\,,$$
$$\int_\Omega \psi \,\mathrm{d}\Omega = 0\,,$$

In both the cases, if $\boldsymbol{B}$ satisfies the compatibility condition

$$\int_{\Sigma_N} \boldsymbol{B} \cdot \boldsymbol{\nu} \,\mathrm{d}\Sigma = 0\,,$$

we have that $\sigma = 0$ and the two formulations coincide. If instead $\Sigma_D \neq \emptyset$, $\sigma = 0$ and the terms associated to it can be neglected, leading to

Problem 2.6. *Find* $\psi \in H^1_{\Sigma_D}(\Omega)$ *such that*

$$\int_\Omega (\mu^{-1} \,\mathbf{grad}\, \psi) \cdot \mathbf{grad}\, v \,\mathrm{d}\Omega = \int_{\Sigma_N} (\boldsymbol{B} \cdot \boldsymbol{\nu}) v \,\mathrm{d}\Sigma\,, \quad v \in H^1_{\Sigma_D}\,.$$

Curl-curl eigenvalue problem

The last problem we will consider is the one associated to a cavity resonator (2.15), which is associated to the following eigenvalue problem

Problem 2.7. *Find the eigenvalue/eigenfunction pair* $(\omega^2, (\sigma, \boldsymbol{E}))$*, with* σ, $\boldsymbol{E} \in H^1_{\Sigma_D} \times H_{\Sigma_D}(\mathbf{curl})$ *and* $\boldsymbol{E} \neq \boldsymbol{0}$*, such that*

$$\int_\Omega (\mu^{-1} \,\mathbf{curl}\, \boldsymbol{E}) \cdot \mathbf{curl}\, \boldsymbol{v} + \epsilon \,(\mathbf{grad}\, \sigma) \cdot \boldsymbol{v} \,\mathrm{d}\Omega = \omega^2 \int_\Omega \boldsymbol{E} \cdot \boldsymbol{v} \,\mathrm{d}\Omega\,, \qquad \boldsymbol{v} \in H_{\Sigma_D}(\mathbf{curl})\,,$$
$$\int_\Omega \sigma\tau - \epsilon \boldsymbol{E} \cdot \mathbf{grad}\, \tau \,\mathrm{d}\Omega = 0\,, \qquad \tau \in H^1_{\Sigma_D}\,,$$

The case $\omega^2 = 0$ is associated to harmonic forms. It is also possible to consider the following equivalent formulation which will be used in practice [AFW10, Section 3.6]:

Problem 2.8. *Find the eigenvalue/eigenfunction pair* $(\omega^2, \boldsymbol{E})$*, with* $\boldsymbol{E} \in H_{\Sigma_D}(\mathbf{curl})$ *and* $\boldsymbol{E} \neq \boldsymbol{0}$ *such that*

$$\int_\Omega (\mu^{-1} \,\mathbf{curl}\, \boldsymbol{E}) \cdot \mathbf{curl}\, \boldsymbol{v} \,\mathrm{d}\Omega = \omega^2 \int_\Omega \epsilon \boldsymbol{E} \cdot \boldsymbol{v} \,\mathrm{d}\Omega\,, \;\; \boldsymbol{v} \in H_{\Sigma_D}(\mathbf{curl})\,.$$

In this case, since we consider exact sequences, the eigenfunctions associated to $\omega^2 = 0$ are gradients of functions in $H^1_{\Sigma_D}$ and are usually simply discarded.

2.3 Axisymmetric domains

In this section, we discuss the case in which the domain is axisymmetric with respect to the z-axis. In this case, it is useful to use cylindrical coordinates and represent the functions in terms of Fourier series.

2.3.1 Cylindrical coordinates

Let us introduce the cylindrical coordinates $(\rho,\, z,\, \theta)$, with the z-axis being the symmetry axis an axisymmetric domain $\breve{\Omega}$. As we will see in the following, the meridian components of a function, associated to the ρz-plane, are treated differently with respect to the azimuthal one, associated to the θ direction. For this reason, vector-valued functions will be ordered as $\boldsymbol{u} = (u_\rho,\, u_z,\, u_\theta)^T$ and, consistently, the angular variable θ is placed as the last one. This uncommon choice will considerably simplify the following considerations starting from the definition of axisymmetric domains. Throughout this thesis we will consider axisymmetric domains satisfying the following assumption:

Assumption 2.4. *We assume the domain $\breve{\Omega}$ to be described though its cross-section with respect to the ρz-plane $S \subset \mathbb{R}^+ \times \mathbb{R}$. We assume that $S \subset \mathbb{R}^2$ is a bounded Lipschitz domain obtained through a diffeomorphism $\boldsymbol{F}$ of the unit square and that $\partial S \cap \{\rho = 0\}$ is either empty or coincides with $\boldsymbol{F}(\{0\}\times[0,\, 1])$. Let $\Gamma_0 = \operatorname{int}(\partial S \cap \{\rho = 0\})$ be the interior of the intersection of the boundary of S with the z-axis and $\Gamma = \partial S \setminus \Gamma_0$. The volume $\breve{\Omega}$ is then obtained rotating the cross-section over the symmetry axis z and adding Γ_0 (see Figure 2.1), i.e.*

$$\breve{\Omega} = \left\{ \boldsymbol{x} \in \mathbb{R}^3 : \boldsymbol{x} = \boldsymbol{g}\Big((\rho,\, z,\, \theta)^T\Big),\ (\rho,\, z)^T \in S,\ \theta \in [0,\, 2\pi) \right\} \cup \Gamma_0 \,. \quad (2.42)$$

We have that $\partial\breve{\Omega} = \Gamma \times [0,\, 2\pi)$.

The Cartesian coordinates are related to the cylindrical ones by the following:

$$\begin{bmatrix} x \\ y \\ z \end{bmatrix} = \boldsymbol{g}\left(\begin{bmatrix} \rho \\ z \\ \theta \end{bmatrix} \right) = \begin{bmatrix} \rho\cos(\theta) \\ \rho\sin(\theta) \\ z \end{bmatrix} .$$

and, conversely, for $\rho > 0$, we have that

$$\rho = \sqrt{x^2 + y^2} \quad \text{and} \quad \theta = \begin{cases} -\arccos\left(\frac{x}{\rho}\right) & \text{if } y < 0\,, \\ \arccos\left(\frac{x}{\rho}\right) & \text{if } y \geq 0\,. \end{cases}$$

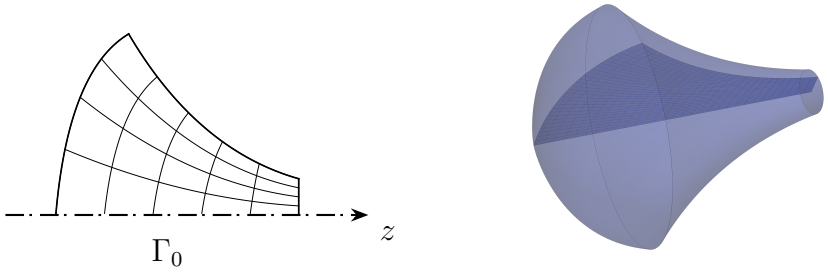

Figure 2.1: Representation of a cross-section S lying on the $\{\rho = 0\}$ axis (right) and its associated axisymmetric domain $\breve{\Omega}$ (right). Γ_0 represents the portion of the boundary of S on the axis.

To a scalar function $u^{\#}(x,\, y,\, z)$, expressed in Cartesian coordinates, is associated the function in cylindrical coordinates given by $u^{\#} \circ \boldsymbol{g}$. Similarly, a vector function expressed using the standard Cartesian base $\boldsymbol{v} = v_x\, \boldsymbol{e}_x + v_y\, \boldsymbol{e}_y + v_z\, \boldsymbol{e}_z$ can be described using the orthonormal base in cylindrical coordinates

$$\boldsymbol{v} = v_\rho\, \boldsymbol{e}_\rho + v_z\, \boldsymbol{e}_z + v_\theta\, \boldsymbol{e}_\theta\,,$$

where

$$v_\rho = v_x \cos(\theta) + v_y \sin(\theta), \quad \text{and} \quad v_\theta = -v_x \sin(\theta) + v_y \cos(\theta)\,.$$

In the following, we assume that the material parameters are axisymmetric, which is

Assumption 2.5. *The material parameters ϵ, μ and σ are axisymmetric, i.e.*

$$\partial_\theta \epsilon = 0\,, \quad \partial_\theta \mu = 0\,, \quad \partial_\theta \sigma = 0\,.$$

A vector function, expressed using the cylindrical basis, is sometimes split in the, so called, meridian and azimuthal components, which are, respectively, $\boldsymbol{u}_{\rho z} = (u_\rho,\, u_z)^T$ and u_θ [ACJL02, Definition 2.1]. The differential operators involved in the de Rham complex in Cartesian coordinates (2.26) correspond to the following ones in cylindrical coordinates:

$$\mathbf{grad}^c\, u = \begin{bmatrix} \partial_\rho u \\ \partial_z u \\ \dfrac{1}{\rho} \partial_\theta u \end{bmatrix}\,, \tag{2.43}$$

$$\mathbf{curl}^c\,\boldsymbol{u} = \begin{bmatrix} \dfrac{1}{\rho}\partial_\theta u_z - \partial_z u_\theta \\ \dfrac{1}{\rho}(\partial_\rho(\rho\,u_\theta) - \partial_\theta u_\rho) \\ \partial_z u_\rho - \partial_\rho u_z \end{bmatrix},$$

$$\mathrm{div}^c\,\boldsymbol{u} = \frac{1}{\rho}\,\partial_\rho(\rho\,u_\rho) + \frac{1}{\rho}\,\partial_\theta u_\theta + \partial_z u_z\,. \tag{2.44}$$

2.3.2 Fourier series

It is often useful to express functions in cylindrical coordinates using the Fourier series

$$\begin{aligned} u(\rho,\,z,\,\theta) &= \sum_{m\in\mathbb{Z}} c^{(m)}(\rho,\,z)\,e^{im\theta}\,, \\ c^{(m)}(\rho,\,z) &= \frac{1}{2\pi}\int_0^{2\pi} u(\rho,\,z,\,\theta)\,e^{-im\theta}\,\mathrm{d}\theta\,. \end{aligned} \tag{2.45}$$

An alternative, equivalent, representation can be written in terms of sine and cosine functions, *i.e.*

$$\begin{aligned} u(\rho,\,z,\,\theta) &= \sum_{m=0}^{\infty} u^{(m)}(\rho,\,z)\cos(m\theta) + \sum_{m=1}^{\infty} u^{(-m)}(\rho,\,z)\sin(m\theta)\,, \\ u^{(0)}(\rho,\,z) &= \frac{1}{2\pi}\int_0^{2\pi} u(\rho,\,z,\,\theta)\,\mathrm{d}\theta\,, \\ u^{(m)}(\rho,\,z) &= \frac{1}{\pi}\int_0^{2\pi} u(\rho,\,z,\,\theta)\cos(m\theta)\,\mathrm{d}\theta\,, \quad m\geq 1\,, \\ u^{(-m)}(\rho,\,z) &= \frac{1}{\pi}\int_0^{2\pi} u(\rho,\,z,\,\theta)\sin(m\theta)\,\mathrm{d}\theta\,, \quad m\geq 1\,. \end{aligned} \tag{2.46}$$

The two representations (2.45)−(2.46) are equivalent, the corresponding coefficients are related by the following expressions:

$$\begin{aligned} c^{(\pm m)} &= \frac{1}{2}\big(u^{(m)} \mp u^{(-m)}\big)\,, && m\geq 0\,, \\ u^{(m)} &= c^{(m)} + c^{(-m)}\,, && m\geq 1\,, \\ u^{(-m)} &= i\,\big(c^{(m)} - c^{(-m)}\big)\,, && m\geq 1\,, \\ u^{(0)} &= c^{(0)}\,. \end{aligned} \tag{2.47}$$

In this section, we will use the representation (2.46) and, in particular, we express each function on $\breve{\Omega}$ as the sum of a symmetric and an antisymmetric

part with respect to the plane at $\theta = 0$. For a scalar function we have that $u = u^s + u^a$, where

$$u^s = u^{(0)} + \sum_{m=1}^{\infty} u^{(m)} \cos(m\theta),$$
$$u^a = \sum_{m=1}^{\infty} u^{(-m)} \sin(m\theta).$$

For a vector function we have instead that $\boldsymbol{u} = \boldsymbol{u}^s + \boldsymbol{u}^a$, where

$$\boldsymbol{u}^s = \begin{bmatrix} u_\rho^{(0)} \\ u_z^{(0)} \\ 0 \end{bmatrix} + \sum_{m=1}^{\infty} \begin{bmatrix} u_\rho^{(m)} \cos(m\theta) \\ u_z^{(m)} \cos(m\theta) \\ u_\theta^{(m)} \sin(m\theta) \end{bmatrix},$$
$$\boldsymbol{u}^a = \begin{bmatrix} 0 \\ 0 \\ u_\theta^{(0)} \end{bmatrix} + \sum_{m=1}^{\infty} \begin{bmatrix} u_\rho^{(-m)} \sin(m\theta) \\ u_z^{(-m)} \sin(m\theta) \\ u_\theta^{(-m)} \cos(m\theta) \end{bmatrix}.$$

The Fourier coefficients $u^{(m)}$, $\boldsymbol{u}^{(m)}$ are defined on the cross section S. Applying the differential operators (2.43)−(2.44) leads to the definition of the following ones, acting directly on the Fourier coefficients:

$$\mathbf{grad}^m u^{(m)} = \begin{bmatrix} \partial_\rho u^{(m)} \\ \partial_z u^{(m)} \\ -\dfrac{m}{\rho} u^{(m)} \end{bmatrix},$$

$$\mathbf{curl}^m \boldsymbol{u}^{(m)} = \begin{bmatrix} -\dfrac{m}{\rho} u_z^{(m)} - \partial_z u_\theta^{(m)} \\ \dfrac{1}{\rho}\Big(\partial_\rho\Big(\rho\, u_\theta^{(m)}\Big) + m\, u_\rho^{(m)}\Big) \\ \partial_z u_\rho^{(m)} - \partial_\rho u_z^{(m)} \end{bmatrix},$$

$$\mathrm{div}^m \boldsymbol{u}^{(m)} = \frac{1}{\rho}\,\partial_\rho\big(\rho\, u_\rho^{(m)}\big) - \frac{m}{\rho} u_\theta^{(m)} + \partial_z u_z\,.$$

Thanks to the fact that $\partial_\theta e^{im\theta} = im\, e^{im\theta}$ we have that

$$\begin{aligned} (\mathbf{grad}^c\, u)^{(m)} &= \mathbf{grad}^m\, u^{(m)}\,, && m \in \mathbb{Z}\,, \\ (\mathbf{curl}^c\, \boldsymbol{u})^{(m)} &= \mathbf{curl}^{-m}\, \boldsymbol{u}^{(-m)}\,, && m \in \mathbb{Z}\,, \\ (\mathrm{div}^c\, \boldsymbol{u})^{(m)} &= \mathrm{div}^m\, \boldsymbol{u}^{(m)}\,, && m \in \mathbb{Z}\,. \end{aligned} \tag{2.48}$$

Weighted Sobolev spaces

The infinitesimal volume element in cylindrical coordinates is given by $\mathrm{d}\breve{\Omega} = \rho\,\mathrm{d}\rho\mathrm{d}z\mathrm{d}\theta$. This fact, and the representation by means of the Fourier series, motivate the introduction of the weighted L^2 spaces defined on the cross-section S [Ber+99, Section II.1], *i.e.*

$$\begin{aligned} L^2_\rho(S) &= \left\{ u : \int_S u^2\,\rho\,\mathrm{d}\rho\mathrm{d}z < \infty \right\}, \\ L^2_\rho(S;\,\mathbb{R}^3) &= \left\{ \boldsymbol{u} : \int_S \|\boldsymbol{u}\|_e^2\,\rho\,\mathrm{d}\rho\mathrm{d}z < \infty \right\}. \end{aligned}$$

Note that $\boldsymbol{u}$ is a vectorial function defined on S which takes values in $\mathbb{R}^3$. The associated norms are the standard ones induced by the inner products

$$(u,\,v)_{L^2_\rho(S)} = \int_S uv\,\rho\,\mathrm{d}\rho\mathrm{d}z\,, \quad (\boldsymbol{u},\,\boldsymbol{v})_{L^2_\rho(S;\,\mathbb{R}^3)} = \int_S \boldsymbol{u}\cdot\boldsymbol{v}\,\rho\,\mathrm{d}\rho\mathrm{d}z\,,$$

and will be often simply denoted using the subscript ρ

$$\|u\|_\rho = \sqrt{(u,\,u)_\rho}\,.$$

Let $\breve{u}$ be a function in Cartesian coordinates belonging to $L^2(\breve{\Omega})$, the map

$$\breve{u} \mapsto \{u^{(m)}\}_{m\in Z}\,, \quad \left(\text{or } \{c^{(m)}\}_{m\in Z}\right),$$

is a bijection from $L^2(\breve{\Omega})$ onto $\Pi_{m\in\mathbb{Z}} L^2_\rho(S)$. Moreover, the norms in the two spaces are equivalent [Ber+99, Theorem II.3.1], *i.e.*

$$\|\breve{u}\|_{L^2(\breve{\Omega})} \cong \sqrt{2\pi \sum_{m\in\mathbb{Z}} \|u^{(m)}\|^2_{L^2_\rho(S)}}\,,$$

where the symbol $\cong$ indicates that there exist two positive constants c and C such that

$$f \cong g \quad \Leftrightarrow \quad cf \le g \le Cf\,.$$

Similarly, if $\breve{\boldsymbol{u}} = (\breve{u}_x,\,\breve{u}_y,\,\breve{u}_z)^T$ is a function in Cartesian coordinates belonging to $L^2(\breve{\Omega};\mathbb{R}^3)$, the map

$$\breve{\boldsymbol{u}} \mapsto \{\boldsymbol{u}^{(m)}\}_{m\in Z}\,, \quad \left(\text{or } \{\boldsymbol{c}^{(m)}\}_{m\in Z}\right),$$

where $\boldsymbol{u}^{(m)} = (u_\rho^{(m)},\,u_z^{(m)},\,u_\theta^{(m)})^T$, is a bijection from $L^2(\breve{\Omega};\mathbb{R}^3)$ onto $\Pi_{m\in\mathbb{Z}} L^2_\rho(S;\,\mathbb{R}^3)$. Moreover, the norms in the two spaces are equivalent [Ber+99, Theorem II.3.6], *i.e.*

$$\|\breve{\boldsymbol{u}}\|_{L^2(\breve{\Omega};\,\mathbb{R}^3)} \cong \sqrt{2\pi \sum_{m\in\mathbb{Z}} \|\boldsymbol{u}^{(m)}\|^2_{L^2_\rho(S;\,\mathbb{R}^3)}}.$$

With the same reasoning, we assume that the following one-to-one maps between the spaces in Cartesian coordinates (2.22), defined on the axisymmetric domain $\breve{\Omega}$, and the corresponding ones in cylindrical coordinates are well-defined:

$$\begin{aligned} H^1(\breve{\Omega}) &\longleftrightarrow \Pi_{m\in\mathbb{Z}} H_\rho(\mathbf{grad}^m;\, S)\,, \\ H(\mathbf{curl};\, \breve{\Omega}) &\longleftrightarrow \Pi_{m\in\mathbb{Z}} H_\rho(\mathbf{curl}^m;\, S)\,, \\ H(\mathrm{div};\, \breve{\Omega}) &\longleftrightarrow \Pi_{m\in\mathbb{Z}} H_\rho(\mathrm{div}^m;\, S)\,, \end{aligned}$$

where the spaces for the Fourier coefficients will be indicated using the following compact notation:

$$\begin{aligned} Z^{m,0} &= H_\rho(\mathbf{grad}^m;\, S) = \left\{u \in L^2_\rho(S) : \mathbf{grad}^m\, u \in L^2_\rho(S;\mathbb{R}^3)\right\}, \\ Z^{m,1} &= H_\rho(\mathbf{curl}^m;\, S) \;= \left\{\boldsymbol{u} \in L^2_\rho(S;\mathbb{R}^3) : \mathbf{curl}^m\, \boldsymbol{u} \in L^2_\rho(S;\mathbb{R}^3)\right\}, \\ Z^{m,2} &= H_\rho(\mathrm{div}^m;\, S) \;\;= \left\{\boldsymbol{u} \in L^2_\rho(S;\mathbb{R}^3) : \mathrm{div}^m\, \boldsymbol{u} \in L^2_\rho(S)\right\}, \\ Z^{m,3} &= L^2_\rho(S)\,, \end{aligned} \tag{2.49}$$

and the corresponding norms are given by

$$\begin{aligned} \|u\|^2_{H_\rho(\mathbf{grad}^m;\, S)} &= \|u\|^2_\rho + \|\mathbf{grad}^m\, u\|^2_\rho\,, \\ \|\boldsymbol{u}\|^2_{H_\rho(\mathbf{curl}^m;\, S)} &= \|\boldsymbol{u}\|^2_\rho + \|\mathbf{curl}^m\, \boldsymbol{u}\|^2_\rho\,, \\ \|\boldsymbol{u}\|^2_{H_\rho(\mathrm{div}^m;\, S)} &= \|\boldsymbol{u}\|^2_\rho + \|\mathrm{div}^m\, \boldsymbol{u}\|^2_\rho\,. \end{aligned}$$

Note that the spaces associated to $-m$ coincide with the spaces associated to m, *e.g.* $H_\rho(\mathbf{curl}^m;\, S) \equiv H_\rho(\mathbf{curl}^{-m};\, S)$.

2.3.3 The de Rham complex

Thanks to (2.48), we can then draw the following diagram for each mode $m \in \mathbb{Z}$:

$$0 \longrightarrow Z^{m,0} \xrightarrow{\mathbf{grad}^m} Z^{m,1} \xrightarrow{\mathbf{curl}^m} Z^{m,2} \xrightarrow{\mathrm{div}^m} Z^{m,3} \longrightarrow 0 \tag{2.50}$$

The case $m = 0$ corresponds to axisymmetric functions and, analogously to the case in Cartesian coordinates (2.39), the complex (2.50) can be decomposed in two subcomplexes

$$\mathbb{R} \longrightarrow u^{(0)} \xrightarrow{\mathbf{grad}} \begin{bmatrix} \boldsymbol{u}^{(0)}_{\rho z} \\ u^{(0)}_\theta \end{bmatrix} \xrightarrow{\begin{matrix} -\,\mathrm{curl} \\ -\,\mathbf{rot}^c \end{matrix}} \begin{bmatrix} \boldsymbol{u}^{(0)}_{\rho z} \\ u^{(0)}_\theta \end{bmatrix} \xrightarrow{\begin{matrix} \mathrm{div}^c \\ 0 \end{matrix}} u^{(0)} \longrightarrow 0$$

where

$$\mathbf{rot}^c u = \begin{bmatrix} \partial_z u \\ -\frac{1}{\rho}\partial_\rho(\rho u) \end{bmatrix} \quad \text{and} \quad \operatorname{div}^c \boldsymbol{u}_{\rho z} = \frac{1}{\rho}\partial_\rho(\rho u_\rho) + \partial_z u_z \,.$$

In this framework, the splitting between meridian and azimuthal component highlight the fact that one of the two subcomplexes involves the standard Cartesian differential operators, but applied to functions in weighted Sobolev spaces. The case $m = 0$ has been studied by different authors and will not be considered in this thesis (see, for example, [ACJL02; CGP08; Erv13; GO12]). In the case $m \neq 0$, which corresponds to functions that are not axisymmetric, we have that the sequence (2.50) is exact [Oh15, Theorem 2.1].

2.3.4 Weak formulations

Consider the mixed formulation introduced in Cartesian coordinates (2.33) and assuming that the weights α_k are axisymmetric, it is possible to change the coordinates and use the Fourier series to obtain the following equality:

$$B(\breve{x},\, \breve{y}) = \sum_{m\in\mathbb{Z}} B_m(x^{(m)},\, y^{(m)})\,,$$

where, in the simple case of the exact sequence (2.34), $\breve{x},\, \breve{y} \in U = V^{k-1} \times V^k$, $x^{(m)},\, y^{(m)} \in U^m = Z^{m,\,k-1} \times Z^{m,\,k}$ and $B_m : U^m \times U^m \to \mathbb{R}$ are bilinear forms, acting on the Fourier coefficients, naturally obtained from the bilinear form in Cartesian coordinates through the change of coordinates and the use of the Fourier series. It is then possible to solve a sequence of problems:

Problem 2.9. *Given $F_m \in (U^m)'$, find $x^{(m)} \in U^m$ such that*

$$B_m(x^{(m)},\, y^{(m)}) = F_m(y^{(m)}), \quad y^{(m)} \in U^m\,.$$

The properties of well-posedness are deduced from the ones in Cartesian coordinates, *e.g.* for the inf-sup condition, for an arbitrary $x^{(m)} \in U^m$ we have to exhibit a $y^{(m)} \in U^m$ such that

$$B_m(x^{(m)},\, y^{(m)}) \geq \gamma \|x^{(m)}\|_{U^m} \|y^{(m)}\|_{U^m}\,.$$

Let $\breve{x}$ be the function in U built from $x^{(m)}$ and let $\breve{y} \in U$ be the function that satisfies the inf-sup condition for $\breve{x}$. Then, considering the Fourier coefficient $y^{(m)}$, we have that

$$B_m(x^{(m)},\, y^{(m)}) = B(\breve{x},\, \breve{y}) \geq \gamma\, \|\breve{x}\|_U\, \|\breve{y}\|_U \geq \gamma \|x^{(m)}\|_{U^m} \|y^{(m)}\|_{U^m}\,.$$

Boundary conditions imposed on the axisymmetric domain boundary $\partial\breve{\Omega}$ correspond to boundary conditions imposed on the curve Γ. We assume that continuous trace operators are well-defined, so that we can establish the continuity of right-hand sides involving boundary terms. For example, considering the Problem 2.3 associated to a Fourier coefficient, we have that

$$\int_{\Gamma_N} \boldsymbol{j}_\Sigma^{(m)} \cdot \gamma_{\boldsymbol{\tau}} \boldsymbol{v}^{(m)} \, \rho \, \mathrm{d}\rho \mathrm{d}z \leq C \, \|\boldsymbol{j}_\Sigma^{(m)}\|_{H_\rho^{-\frac{1}{2}}(\Gamma_N)} \|\boldsymbol{v}^{(m)}\|_{H_\rho(\mathbf{curl}^m; S)} \, .$$

In this framework, always considering $m \neq 0$, we can derive the well-posed formulations for the Fourier coefficients in axisymmetric domains from the ones introduced in Section 2.2. The mixed formulation for the vector potential, presented in Problem 2.3, becomes

Problem 2.10. *Find* $\sigma^{(m)}$, $\boldsymbol{A}^{(m)} \in H_{\rho,\Gamma_D}(\mathbf{grad}^m) \times H_{\rho,\Gamma_D}(\mathbf{curl}^m)$ *such that*

$$\begin{aligned}
&\int_S (\mu^{-1} \, \mathbf{curl}^m \, \boldsymbol{A}^{(m)}) \cdot (\mathbf{curl}^m \, \boldsymbol{v}) \, \rho \, \mathrm{d}\rho \mathrm{d}z \\
&\qquad + \int_S \epsilon \, (\mathbf{grad}^m \, \sigma^{(m)}) \cdot \boldsymbol{v} \, \rho \, \mathrm{d}\rho \mathrm{d}z \qquad\qquad \boldsymbol{v} \in H_{\rho,\Gamma_D}(\mathbf{curl}^m) \, , \\
&= \int_S \boldsymbol{j}^{(m)} \cdot \boldsymbol{v} \, \rho \, \mathrm{d}\rho \mathrm{d}z \\
&\qquad - \int_{\Gamma_N} \boldsymbol{j}_\Sigma^{(m)} \cdot (\gamma_T \, \boldsymbol{v}) \, \rho \, \mathrm{d}\rho \mathrm{d}z \, , \\
&\int_S \epsilon \boldsymbol{A}^{(m)} \cdot (\mathbf{grad}^m \, \tau) \, \rho \, \mathrm{d}\rho \mathrm{d}z = 0 \, , \qquad\qquad \tau \in H_{\rho,\Gamma_D}(\mathbf{grad}^m) \, ,
\end{aligned}$$

where $\boldsymbol{j}^m \in L^2_\rho$, $\boldsymbol{j}_\Sigma^{(m)} \in H_\rho^{-\frac{1}{2}}(\Gamma_N)$ *and the boundary conditions for the spaces involved are imposed on* Γ_D *and* Γ_N*, which are associated to* Σ_D *and* Σ_N*, respectively.*

The corresponding weak formulation for the magnetic scalar potential, presented in Problem 2.6, becomes

Problem 2.11. *Find* $\psi^{(m)} \in H_{\rho,\Gamma_D}(\mathbf{grad}^m)$ *such that*

$$\begin{aligned}
&\int_S (\mu^{-1} \, \mathbf{grad}^m \, \psi^{(m)}) \cdot (\mathbf{grad}^m \, v) \, \rho \, \mathrm{d}\rho \mathrm{d}z \\
&\qquad\qquad = \int_{\Gamma_N} (\boldsymbol{B}^{(m)} \cdot \boldsymbol{\nu}) v \, \rho \, \mathrm{d}\rho \mathrm{d}z \, , \qquad v \in H_{\rho,\Gamma_D}(\mathbf{grad}^m) \, ,
\end{aligned}$$

where $\boldsymbol{B}^{(m)} \in H_\rho^{-\frac{1}{2}}(\Gamma_N)$.

Finally, for the eigenvalue Problem 2.8, we consider the following formulation:

Problem 2.12. *Find the eigenvalue/eigenfunction pair* $(\omega^2, \boldsymbol{E}^{(m)}) \in \mathbb{R} \times H_{\rho,\Gamma_D}(\mathbf{curl}^m)$*, with* $\boldsymbol{E} \neq \mathbf{0}$*, such that*

$$\int_S (\mu^{-1}\,\mathbf{curl}^m\,\boldsymbol{E}^{(m)}) \cdot \mathbf{curl}^m\,\boldsymbol{v}\,\rho\,\mathrm{d}\rho\mathrm{d}z = \omega^2 \int_S \epsilon \boldsymbol{E}^{(m)} \cdot \boldsymbol{v}\,\rho\,\mathrm{d}\rho\mathrm{d}z \quad , \quad \boldsymbol{v} \in H_{\rho,\Gamma_D}(\mathbf{curl}^m)\,.$$

In this chapter, we have introduced all the weak formulations for the problems we will encounter in the chapter devoted to applications. In Chapter 4, we will build the conforming finite-dimensional approximations for the functional spaces introduced here.

Chapter 3

Hamiltonian mechanics

In this chapter, we briefly recall the main concepts of Hamiltonian mechanics, which will be the framework used in the chapter devoted to practical applications to determine the motion of a relativistic charged particle in an electromagnetic field. To this end, we will give at first a general introduction on the subject, mainly following [GPS02], and we will then present the particular case of a charged particle moving at relativistic speed in a magnetostatic field. This specific situation is common in high-energy circular particle accelerators, in which the charged particles in a beam travel, following the circumference of the accelerator, through different elements which affect the particle trajectories with their fields.

Consider a system with a d-dimensional configuration space which is described by d independent generalized coordinates $\boldsymbol{q}$. The evolution of this system with respect to an independent variable t is described by a curve $\boldsymbol{q}(t)$ in the configuration space. The Hamilton principle states that the evolution of the system $\boldsymbol{q}(t)$ from time $t = t_0$ to $t = t_f$ is such that the action

$$\mathcal{A}(\boldsymbol{q}) = \int_{t_0}^{t_f} \mathcal{L}(\boldsymbol{q},\, \dot{\boldsymbol{q}},\, t)\, \mathrm{d}t\,, \tag{3.1}$$

is stationary [GPS02, Section 2.1]. In (3.1), the Lagrangian $\mathcal{L}$ is a smooth function which is often dependent on the kinetic energy $T(\boldsymbol{q},\, \dot{\boldsymbol{q}},\, t)$ and on the generalized potential energy $U(\boldsymbol{q},\, \dot{\boldsymbol{q}},\, t)$, which is, in general, not only a function of the generalized coordinates $\boldsymbol{q}$, but also a function of the generalized velocities $\dot{\boldsymbol{q}}$ and of time. Associated to the generalized potential energy, we introduce the generalized forces

$$G_i = -\frac{\partial U}{\partial q_i} + \frac{\mathrm{d}}{\mathrm{d}t}\left(\frac{\partial U}{\partial \dot{q}}\right). \tag{3.2}$$

The generalized forces G_i do not necessarily have the dimension of a force, but their product with the associated generalized coordinate q_i has always the dimension of work. Consider the evolution of the system from $\boldsymbol{q}_0 = \boldsymbol{q}(t_0)$ to $\boldsymbol{q}_f = \boldsymbol{q}(t_f)$ and the variation of (3.1)

$$\begin{aligned}\delta\mathcal{A} &= \int_{t_0}^{t_f} \frac{\partial\mathcal{L}}{\partial\boldsymbol{q}} \cdot \delta\boldsymbol{q} + \frac{\partial\mathcal{L}}{\partial\dot{\boldsymbol{q}}} \cdot \delta\dot{\boldsymbol{q}}\,\mathrm{d}t \\ &= \int_{t_0}^{t_f} \left[\frac{\partial\mathcal{L}}{\partial\boldsymbol{q}} + \frac{\mathrm{d}}{\mathrm{d}t}\frac{\partial\mathcal{L}}{\partial\dot{\boldsymbol{q}}}\right] \cdot \delta\boldsymbol{q}\,\mathrm{d}t\,,\end{aligned}$$

where the last equation is obtained integrating by parts and considering the fact that the extrema of the trajectories are fixed, so

$$\delta\boldsymbol{q}(t_0) = \delta\boldsymbol{q}(t_f) = \boldsymbol{0}\,.$$

Since we can choose the variations of the generalized coordinates independently, assuming smooth functions, we obtain the Euler-Lagrange equations

$$\frac{\partial\mathcal{L}}{\partial q_i} - \frac{\mathrm{d}}{\mathrm{d}t}\left(\frac{\partial\mathcal{L}}{\partial\dot{q}_i}\right) = 0\,, \quad i = 1,\,\ldots,\,d\,. \tag{3.3}$$

Applying a Legendre transformation with respect to $\dot{\boldsymbol{q}}$ to the Lagrangian we obtain the Hamiltonian of the system

$$\mathcal{H}(\boldsymbol{q},\,\boldsymbol{p},\,t) = \boldsymbol{p}\cdot\dot{\boldsymbol{q}} - \mathcal{L}(\boldsymbol{q},\,\dot{\boldsymbol{q}},\,t)\,,$$

where

$$p_i = \frac{\partial\mathcal{L}}{\partial\dot{q}_i}(\boldsymbol{q},\,\dot{\boldsymbol{q}},\,t) \quad i = 1,\,\ldots,\,d$$

are the conjugate momenta, or canonical momenta. The quantities $(\boldsymbol{q},\,\boldsymbol{p})$ are called canonical variables. Once a Hamiltonian is given, we can consider another principle, sometimes referred as modified Hamilton principle [GPS02, Section 8.5], where the system evolution is considered in a $2d$-dimensional phase space with independent canonical variables and the physical trajectory is such that the following action is stationary:

$$\mathcal{A}(\boldsymbol{q},\,\boldsymbol{p}) = \int_{t_0}^{t_f} \boldsymbol{p}\cdot\dot{\boldsymbol{q}} - \mathcal{H}(\boldsymbol{q},\,\boldsymbol{p},\,t)\,\mathrm{d}t\,. \tag{3.4}$$

Also in this case it is convenient to consider null variations at the end points, *i.e.*

$$\delta\boldsymbol{q}(t_0) = \delta\boldsymbol{q}(t_f) = \delta\boldsymbol{p}(t_0) = \delta\boldsymbol{p}(t_f) = \boldsymbol{0}\,.$$

With the same argument used to obtain (3.3), we can compute the first variation of (3.4) and obtain the set of first order differential equations known as Hamilton equations:

$$\begin{aligned} \dot{q}_i &= \frac{\partial \mathcal{H}}{\partial p_i} \quad i = 1, \ldots, d\,, \\ \dot{p}_i &= -\frac{\partial \mathcal{H}}{\partial q_i} \quad i = 1, \ldots, d\,. \end{aligned} \tag{3.5}$$

Grouping the canonical variables in a single vector

$$\boldsymbol{w}(t) = (q_1, \ldots, q_d, p_1, \ldots, p_d)^T \in \mathbb{R}^{2d}\,,$$

it is possible to rewrite (3.5) in a compact form as

$$\dot{\boldsymbol{w}} = \mathbf{J}\nabla\mathcal{H}(\boldsymbol{w}, t) = -\mathbf{J}^{-1}\nabla\mathcal{H}(\boldsymbol{w}, t) = -\mathbf{J}^T\nabla\mathcal{H}(\boldsymbol{w}, t)\,, \tag{3.6}$$

where

$$\mathbf{J} = \begin{bmatrix} \mathbf{0}_d & \mathbf{I}_d \\ -\mathbf{I}_d & \mathbf{0}_d \end{bmatrix} \in \mathbb{R}^{2d\times 2d}\,, \tag{3.7}$$

$\mathbf{0}_d$ is the d-dimensional zero matrix and $\mathbf{I}_d$ is the d-dimensional identity matrix.

The Hamilton equations can be also written using a different formalism [GPS02, Section 9.6]. For this purpose, it is necessary to introduce some definitions. The Poisson bracket for two functions in a d-dimensional system is defined as

$$[f, g] = \frac{\partial f}{\partial q_i}\frac{\partial g}{\partial p_i} - \frac{\partial f}{\partial p_i}\frac{\partial g}{\partial q_i} = \frac{\partial f}{\partial w_i}\,[\mathbf{J}]_{ij}\,\frac{\partial g}{\partial w_j}\,, \tag{3.8}$$

where the Einstein notation has been used, *i.e.* quantities with the same index are summed together over the all range of the index. If we have two generic functions of the canonical variables $\boldsymbol{f}, \boldsymbol{g} : \mathbb{R}^{2d} \to \mathbb{R}^n$, the square matrix $\mathbb{R}^{n\times n}$ Poisson bracket can be written as

$$[\boldsymbol{f}, \boldsymbol{g}] = J_{\boldsymbol{f}}\,\mathbf{J}\,J_{\boldsymbol{g}}{}^T\,,$$

where $J_{\boldsymbol{f}}$ and $J_{\boldsymbol{g}}$ denote the Jacobian matrices of $\boldsymbol{f}$ and $\boldsymbol{g}$, respectively. Using the Poisson bracket we can easily see that

$$[\boldsymbol{w}, \boldsymbol{w}] = \mathbf{J}$$

and Hamilton equations can be written as

$$\dot{\boldsymbol{w}} = [\boldsymbol{w}, \mathcal{H}].$$

To each function of the dynamical variables (and eventually time) a differential operator, called Lie operator [Dra97, Section 1.2.7], can be associated:

$$: f : \; = [f, \cdot] = \frac{\partial f}{\partial w_i} [\mathbf{J}]_{ij} \frac{\partial}{\partial w_j} \, .$$

A generic power of a Lie operator is defined by composition, *i.e.*

$$\begin{aligned} &: f : {}^0 = \mathbf{I} \; ; \\ &: f : {}^k = \underbrace{[f \, , [f \, , [f \, , \ldots [f}_{k \, times} , \cdot \underbrace{] \ldots]]]}_{k \, times} \, . \end{aligned}$$

As a consequence, the exponential of a Lie operator, called Lie transformation, can be defined:

$$\exp(: f :) = \sum_{k=0}^{+\infty} \frac{: f : {}^k}{k!} \, . \tag{3.9}$$

As a consequence, equations (3.5) can be written as

$$\dot{\boldsymbol{w}} =: \; - \mathcal{H} : \boldsymbol{w}$$

and, if the Hamiltonian $\mathcal{H}$ is autonomous (*i.e.* it does not explicitly depend on the independent variable t), the solution of this system can be represented as

$$\boldsymbol{w}(t_f) = \exp((t_f - t_0) : \; - \mathcal{H} :) \boldsymbol{w}_0 \, ,$$

where $\boldsymbol{w}_0$ is the initial condition at time $t = t_0$.

An important aspect of Hamiltonian systems is the symplecticity of their flow. The flow ϕ is the function of time that, given an initial condition $\boldsymbol{w}_0$, describes the evolution of the canonical variables, so that $\boldsymbol{w}(t) = \phi_t(\boldsymbol{w}_0)$. The symplecticity is a property of a generic map acting on the canonical variables [HLW06, Definition 2.2]:

Definition 3.1. *A generic differentiable map $\mathcal{M} : U \subset \mathbb{R}^{2d} \to \mathbb{R}^{2d}$ (where U is an open set) is called symplectic if*

$$J_{\mathcal{M}}(\boldsymbol{w})^T \, \mathbf{J} \, J_{\mathcal{M}}(\boldsymbol{w}) = \mathbf{J} \qquad \boldsymbol{w} \in U \, ,$$

where $J_{\mathcal{M}}$ is the Jacobian matrix of the map $\mathcal{M}$.

Moreover, it can be seen that the previous definition of symplecticity, for a map $\mathcal{M}$ acting on the canonical variables, is equivalent to the preservation of the fundamental Poisson bracket [Dra97, Section 6.1.2]. In fact, let $\widetilde{\boldsymbol{w}} = \mathcal{M}(\boldsymbol{w})$, the Poisson brackets (3.8) applied to a generic component can be written as:

$$[\widetilde{\boldsymbol{w}}, \, \widetilde{\boldsymbol{w}}] = J_{\mathcal{M}} \, \mathbf{J} \, J_{\mathcal{M}}{}^T = \mathbf{J} = [\boldsymbol{w}, \, \boldsymbol{w}].$$

3.1 Canonical transformations

Canonical transformations act on the canonical variables preserving the form of the Hamilton equations (3.5). Consider two sets of canonical variables $(\boldsymbol{q}, \boldsymbol{p})^T$, $(\boldsymbol{Q}, \boldsymbol{P})^T$, both with fixed values at the extrema t_0 and t_f, with the associated Hamiltonians $\mathcal{H}(\boldsymbol{q}, \boldsymbol{p})$ and $\mathcal{K}(\boldsymbol{Q}, \boldsymbol{P})$. The evolution of the system for both coordinates should obey the Hamilton principle

$$\delta \int_{t_0}^{t_f} \boldsymbol{p} \cdot \dot{\boldsymbol{q}} - \mathcal{H} \, \mathrm{d}t = 0 \quad \text{and} \quad \delta \int_{t_0}^{t_f} \boldsymbol{P} \cdot \dot{\boldsymbol{Q}} - \mathcal{K} \, \mathrm{d}t = 0 \,. \tag{3.10}$$

If the canonical variables are stationary points for these actions, also the variation of the following action is null:

$$\delta \int_{t_0}^{t_f} \lambda[\boldsymbol{p} \cdot \dot{\boldsymbol{q}} - \mathcal{H}] - \frac{\mathrm{d}F}{\mathrm{d}t} \, \mathrm{d}t = 0 \,, \tag{3.11}$$

where F is a smooth function of the canonical variables $(\boldsymbol{q}, \boldsymbol{p})^T$ and $(\boldsymbol{Q}, \boldsymbol{P})^T$. So the two set of canonical variables and Hamiltonians can be related comparing the integrands of the actions (3.10) and (3.11), thus leading to

$$\lambda[\boldsymbol{p} \cdot \dot{\boldsymbol{q}} - \mathcal{H}] = \boldsymbol{P} \cdot \dot{\boldsymbol{Q}} - \mathcal{K} + \frac{\mathrm{d}F}{\mathrm{d}t} \,, \tag{3.12}$$

where $\lambda \neq 0$ is a scaling factor that is often taken to be equal to 1, in which case the transformation that links $(\boldsymbol{q}, \boldsymbol{p})^T$ to $(\boldsymbol{Q}, \boldsymbol{P})^T$ is called canonical transformation. The transformations of the canonical variables for which $\lambda \neq 1$ are sometimes called extended canonical transformations. It is always possible to consider canonical transformations using a scaling $\boldsymbol{Q} = \mu \boldsymbol{q}$, $\boldsymbol{P} = \nu \boldsymbol{p}$, $\mathcal{K}(\boldsymbol{Q}, \boldsymbol{P}) = \mu\nu \, \mathcal{H}(\boldsymbol{q}, \boldsymbol{p})$ with $\mu\nu = \lambda$ so that

$$\lambda[\boldsymbol{p} \cdot \dot{\boldsymbol{q}} - \mathcal{H}] = \boldsymbol{P} \cdot \dot{\boldsymbol{Q}} - \mathcal{K} \,.$$

The function $F(\boldsymbol{q}, \boldsymbol{p}, \boldsymbol{Q}, \boldsymbol{P}, t)$ in (3.12) is called generating function. There are four basic types of generating functions, which are expressed using auxiliary functions F_i that depends on either $\boldsymbol{q}$ or $\boldsymbol{p}$ and either $\boldsymbol{Q}$ or $\boldsymbol{P}$:

$$\begin{aligned} F &= F_1(\boldsymbol{q}, \boldsymbol{Q}, t) \,, \\ F &= F_2(\boldsymbol{q}, \boldsymbol{P}, t) - \boldsymbol{Q} \cdot \boldsymbol{P} \,, \\ F &= F_3(\boldsymbol{p}, \boldsymbol{Q}, t) + \boldsymbol{q} \cdot \boldsymbol{p} \,, \\ F &= F_4(\boldsymbol{p}, \boldsymbol{P}, t) + \boldsymbol{q} \cdot \boldsymbol{p} - \boldsymbol{Q} \cdot \boldsymbol{P} \,. \end{aligned} \tag{3.13}$$

The explicit transformation that links $(\boldsymbol{q}, \boldsymbol{p})^T$ to $(\boldsymbol{Q}, \boldsymbol{P})^T$ is then obtained expanding the total time derivative in (3.12) and imposing equality. For example for (3.13), (3.12) reads

$$\begin{aligned}\boldsymbol{p}\cdot\dot{\boldsymbol{q}} - \mathcal{H} &= \boldsymbol{P}\cdot\dot{\boldsymbol{Q}} - \mathcal{K} + \frac{\partial F}{\partial \boldsymbol{q}}\cdot\dot{\boldsymbol{q}} + \frac{\partial F}{\partial \boldsymbol{p}}\cdot\dot{\boldsymbol{p}} + \frac{\partial F}{\partial \boldsymbol{Q}}\cdot\dot{\boldsymbol{Q}} + \frac{\partial F}{\partial \boldsymbol{P}}\cdot\dot{\boldsymbol{P}} + \frac{\partial F}{\partial t} \\ &= -\mathcal{K} + \frac{\partial F_2}{\partial \boldsymbol{q}}\cdot\dot{\boldsymbol{q}} + \left[\frac{\partial F_2}{\partial \boldsymbol{P}} - \boldsymbol{Q}\right]\cdot\dot{\boldsymbol{P}} + \frac{\partial F_2}{\partial t}\,,\end{aligned}$$

from which, equating the terms, we obtain the relations

$$p_i = \frac{\partial F_2}{\partial q_i}\,, \qquad Q_i = \frac{\partial F_2}{\partial P_i} \quad \text{and} \quad \mathcal{K} = \mathcal{H} + \frac{\partial F_2}{\partial t}\,. \tag{3.14}$$

It is possible to show that a transformation is canonical if and only if it is symplectic [Dra97, Section 6.1.2] [GPS02, Section 9.3]. For the case of an extended canonical transformation $\mathcal{M}$, the symplectic condition is substituted by the requirement that its Jacobian matrix satisfies the condition

$$J_{\mathcal{M}}{}^T\,\mathbf{J}\,J_{\mathcal{M}} = \lambda\,\mathbf{J}\,.$$

Another way to produce canonical transformations is using Lie transformations (3.9). In fact, it can be shown that these generate symplectic maps and thus, canonical transformations [Dra97, Section 7.1].
Given a function $g(\boldsymbol{w}, t)$, the new dynamical variables $\widetilde{\boldsymbol{w}}$ can be obtained in this case applying

$$\widetilde{\boldsymbol{w}}(\boldsymbol{w}, t) = \exp\left(: g(\boldsymbol{w}, t) : \right)\boldsymbol{w}$$

and the inverse of this transformation is

$$\boldsymbol{w}(\widetilde{\boldsymbol{w}}, t) = \exp\left(-: g(\widetilde{\boldsymbol{w}}, t) : \right)\widetilde{\boldsymbol{w}}\,.$$

3.2 Relativistic charged particle Hamiltonian

In this section, we present the specific Hamiltonian describing a relativistic charged particle in an electromagnetic field. Having in mind the application to high-energy particle accelerators and to magnetic quadrupoles, we will first introduce the concepts in a general framework and we will then consider the magnetostatic case with a particle travelling at high speed along the longitudinal direction z. This latter assumption regarding the preferred direction of the motion allows, on one side, to use the longitudinal variable

z as independent variable (instead of the time t) and, on the other, to further simplify the form of the Hamiltonian describing the system, using the so called paraxial approximation [Wol14, Chapter 3].

Consider the motion of a particle with charge C and rest m, whose position in Cartesian coordinates $\boldsymbol{r}(\boldsymbol{q}, t)$ is expressed in terms of generalized coordinates. In this case the velocity of this particle $\boldsymbol{v}(\boldsymbol{q}, \dot{\boldsymbol{q}}, t)$ is defined as the derivative its position with respect to time, *i.e.*

$$\boldsymbol{v} = \dot{\boldsymbol{r}} = \frac{\partial \boldsymbol{r}}{\partial q_i}\dot{q}_i + \frac{\partial \boldsymbol{r}}{\partial t}\,.$$

For example, using Cartesian coordinates for $\boldsymbol{q} = (x, y, z)^T$ as well, the velocity is simply given by

$$\boldsymbol{v} = (\dot{x}, \dot{y}, \dot{z})^T\,,$$

while in cylindrical coordinates $\boldsymbol{q} = (\rho, \theta, z)^T$ we have that the velocity in the Cartesian reference system is given by

$$\boldsymbol{v} = \Big(\cos(\theta)\,\dot{\rho} - \rho\sin(\theta)\,\dot{\theta},\ \sin(\theta)\,\dot{\rho} + \rho\cos(\theta)\,\dot{\theta},\ \dot{z}\Big)^T\,.$$

The kinetic energy of a particle moving at relativistic speed, which takes into account also its rest energy, is given by:

$$T(\|\boldsymbol{v}\|^2) = \gamma\big(\|\boldsymbol{v}\|^2\big) m\, c^2\,,$$

where c is the speed of light and γ is the Lorentz factor

$$\gamma\big(\|\boldsymbol{v}\|^2\big) = \frac{1}{\sqrt{1 - \|\boldsymbol{v}\|^2/c^2}} = \frac{1}{\sqrt{1-\beta^2}}\,. \tag{3.15}$$

The field information enters in the Hamiltonian formulation through the elctromagnetic potentials (2.10) and (2.9), already introduced in Chapter 2, that we recall here

$$\boldsymbol{E} = -\partial_t \boldsymbol{A} - \mathbf{grad}\,\phi\,, \qquad \boldsymbol{B} = \mathbf{curl}\,\boldsymbol{A}\,.$$

The generalized potential energy of an electromagnetic field is then given by

$$U = C\,\phi - C\,\boldsymbol{v}\cdot\boldsymbol{A}\,,$$

where both the potentials, in general, can depend on positions and time. The generalized forces, in the case of Cartesian coordinates, can be computed using (3.2) and coincide with the Lorentz force

$$\boldsymbol{F} = C(\boldsymbol{E} + \boldsymbol{v}\times\boldsymbol{B})\,.$$

The Lagrangian for a charged particle in an electromagnetic field is given by

$$\mathcal{L} = -\frac{m\,c^2}{\gamma(\|\boldsymbol{v}\|^2)} - C\,\phi + C\,\boldsymbol{v}\cdot\boldsymbol{A}\,.$$

If we choose the Cartesian coordinates $\boldsymbol{q}(t) = (x,\, y,\, z)^T$ as generalized coordinates, we can obtain the corresponding conjugate momenta $\boldsymbol{p}(t) = (p_x,\, p_y,\, p_z)^T$

$$\boldsymbol{p} = m\,\gamma\,\boldsymbol{v} + C\,\boldsymbol{A}\,,$$

which are related to the mechanical momenta $\boldsymbol{p}^M = m\,\gamma\,\boldsymbol{v}$ by the following relationship:

$$\boldsymbol{p} = \boldsymbol{p}^M + C\,\boldsymbol{A}.$$

The corresponding Hamiltonian is then [PP62, Equation (23–18)]

$$\mathcal{H}(\boldsymbol{q},\,\boldsymbol{p},\,t) = \sqrt{m^2c^4 + c^2\,\|\boldsymbol{p} - C\,\boldsymbol{A}(\boldsymbol{q},\,t)\|^2} + C\,\phi(\boldsymbol{q},\,t)\,. \tag{3.16}$$

3.2.1 Scaled deviation variables

In particle accelerators it is often convenient to scale the different quantities and to work with dimensionless variables. To this end, we choose a reference length L, a reference momentum module p^0, a reference magnitude for the electric field intensity E and a reference magnitude for the magnetic flux density B, we rescale

$$\boldsymbol{Q} = \frac{\boldsymbol{q}}{L}\,,\quad \boldsymbol{P} = \frac{\boldsymbol{p}}{p^0}\,,\quad T = \frac{c}{L}\,t\,,\quad \widetilde{\boldsymbol{A}} = \frac{\boldsymbol{A}}{B\,L}\,,\quad \widetilde{\phi} = \frac{\phi}{E\,L} \tag{3.17}$$

and we consider the resulting dimensionless action $\widetilde{\mathcal{A}} = \mathcal{A}/(L\,p^0)$ to which is associated the dimensionless Hamiltonian

$$\widetilde{\mathcal{H}}(\boldsymbol{Q},\,\boldsymbol{P},\,T) = \frac{\mathcal{H}}{p^0\,c} = \sqrt{\frac{1}{D_1^2} + \left\|\boldsymbol{P} - D_2\,\widetilde{\boldsymbol{A}}\right\|^2} + D_3\,\widetilde{\phi}\,, \tag{3.18}$$

where D_1, D_2 and D_3 are dimensionless coefficients given by

$$D_1 = \frac{p^0}{m\,c}\,,\qquad D_2 = \frac{C\,B\,L}{p^0}\,,\qquad D_3 = \frac{C\,E\,L}{p^0\,c}\,.$$

In this case, the relativistic Hamilton equations can be written as (3.6)

$$\dot{\boldsymbol{w}} = \mathbf{J}\,\nabla\widetilde{\mathcal{H}}(\boldsymbol{w},\,T) = \\ = \begin{bmatrix} \dfrac{\boldsymbol{P} - D_2\widetilde{\boldsymbol{A}}}{\sqrt{1/D_1^2 + \left\|\boldsymbol{P} - D_2\,\widetilde{\boldsymbol{A}}\right\|^2}} \\ \dfrac{D_2}{\sqrt{1/D_1^2 + \left\|\boldsymbol{P} - D_2\,\widetilde{\boldsymbol{A}}\right\|^2}}\, J_{\widetilde{\boldsymbol{A}}}{}^T\left(\boldsymbol{P} - D_2\,\widetilde{\boldsymbol{A}}\right) - \nabla_{\boldsymbol{Q}}\widetilde{\phi} \end{bmatrix},$$

where $\nabla_{\boldsymbol{Q}}$ denote the gradient with respect only to the generalized coordinates $\boldsymbol{Q}$. If the considered potentials $\boldsymbol{A}$ and ϕ are stationary, *i.e.* independent of time t, then we have that the Hamiltonians (3.16), (3.18) are as well independent of time and constant.

Absence of electric scalar potential

We will now consider the absence of an electric scalar potential, *i.e.* $\widetilde{\phi} \equiv 0$, and we will derive some other Hamiltonians used in practice. In some applications the particle moves almost at the speed of light along a given direction that we will associate to Z. In these cases it is useful to describe the particle trajectory using Z as independent variable instead of T. The change of variable can be done considering the action

$$\widetilde{\mathcal{A}} = \int_{T_0}^{T_f} \left[P_x\frac{\mathrm{d}X}{\mathrm{d}T} + P_y\frac{\mathrm{d}Y}{\mathrm{d}T} + P_z\frac{\mathrm{d}Z}{\mathrm{d}T} - \widetilde{\mathcal{H}}\right]\mathrm{d}T\,,$$

and, since for a particle travelling at high speed in the Z direction $\dfrac{\mathrm{d}Z}{\mathrm{d}T} \neq 0$, changing the integration variable:

$$\int_{Z_0}^{Z_f} \left[P_x\frac{\mathrm{d}X}{\mathrm{d}Z} + P_y\frac{\mathrm{d}Y}{\mathrm{d}Z} + P_z - \widetilde{\mathcal{H}}\frac{\mathrm{d}T}{\mathrm{d}Z}\right]\mathrm{d}Z\,.$$

Using (3.18) in absence of an electric scalar potential $\widetilde{\phi}$, it is possible to express P_z as a function of the other variables with the following formula:

$$P_z = \sqrt{\widetilde{\mathcal{H}}^2 - \frac{1}{D_1^2} - \left(P_x - D_2\,\widetilde{A}_x\right)^2 - \left(P_y - D_2\,\widetilde{A}_y\right)^2} + D_2\,\widetilde{A}_z$$

and to consider $-P_z$ as a new Hamiltonian $\mathcal{G}$ and $\left(T,\,-\widetilde{\mathcal{H}}\right)$ as a canonical pair.

It is possible to introduce another quantity δ, which is the relative deviation of the mechanical momentum module with respect to the reference momentum p^0

$$\delta = \frac{\left\|\boldsymbol{p}^M\right\| - p^0}{p^0}\,. \tag{3.19}$$

Expressing the mechanical momenta in terms of the Lorentz factor (3.15), it is possible to see that

$$(\delta+1)^2 = \frac{\left\|\boldsymbol{p}^M\right\|^2}{(p^0)^2} = \frac{\gamma^2\,\beta^2}{D_1^2} = \frac{\gamma^2-1}{D_1^2}\,,$$

and that, considering (3.18) in absence of electric scalar potential, we have:

$$\frac{\gamma}{D_1} = \widetilde{\mathcal{H}}\,.$$

For our purposes, we will use the the momentum deviation variable δ (3.19) instead of $-\widetilde{\mathcal{H}}$. We therefore apply a canonical transformation using the following generating function (3.13):

$$F_2(X,\,Y,\,T,P_x,P_y,\delta;Z) = X\,P_x + Y\,P_y + \delta\left(Z - \frac{\gamma}{D_1\,\delta}\,T\right).$$

Applying the relations (3.14)

$$\begin{aligned}
\gamma &= \sqrt{D_1^2(\delta+1)^2+1}\,,\\
-\widetilde{\mathcal{H}} &= \frac{\partial F_2}{\partial T} = -\frac{\gamma}{D_1}\,,\\
\ell &= \frac{\partial F_2}{\partial \delta} = Z - \frac{D_1(\delta+1)}{\gamma}\,T = Z - \beta\,T\,,\\
\mathcal{G}_2 &= \mathcal{G} + \frac{\partial F_2}{\partial Z} = \mathcal{G} + \delta\,,
\end{aligned}$$

we end up with a system ruled by the Hamiltonian

$$\begin{aligned}
\mathcal{G}_2(\boldsymbol{w},\,Z) = -\sqrt{(\delta+1)^2 - \left(P_x - D_2\,\widetilde{A}_x\right)^2 - \left(P_y - D_2\,\widetilde{A}_y\right)^2}\\
- D_2\,\widetilde{A}_z\ + \delta\,,
\end{aligned}$$

where $\boldsymbol{w} = (X,\,Y,\,\ell,P_x,P_y,\delta)$ are the new canonical variables. The system associated to the Hamiltonian $\mathcal{G}_2$ is not autonomous, since such Hamiltonian explicitly depends on the independent variable Z through the vector potential

$\widetilde{\boldsymbol{A}}(X, Y, Z, T)$. In order to study an equivalent autonomous system, we can use a trivial change of independent variable $\sigma(Z) = Z$ and introduce another action

$$\mathcal{C}[\boldsymbol{w}] = \int_{\sigma_0}^{\sigma_f} \left[P_x \frac{\mathrm{d}X}{\mathrm{d}\sigma} + P_y \frac{\mathrm{d}Y}{\mathrm{d}\sigma} + \delta \frac{\mathrm{d}\ell}{\mathrm{d}\sigma} + P_z \frac{\mathrm{d}Z}{\mathrm{d}\sigma} - \widetilde{\mathcal{K}} \right] \mathrm{d}\sigma \,,$$

where

$$\begin{aligned} \widetilde{\mathcal{K}}(\boldsymbol{w};\, \sigma) = &-\sqrt{(\delta+1)^2 - \left(P_x - D_2\, \widetilde{A}_x\right)^2 - \left(P_y - D_2\, \widetilde{A}_y\right)^2} \\ &- D_2\, \widetilde{A}_z + P_z + \delta \end{aligned} \tag{3.20}$$

and $\boldsymbol{w} = (X,\, Y,\, \ell,\, Z,\, P_x,\, P_y,\, \delta,\, P_z)$.

Paraxial approximation

For a particle moving at high speed in an accelerator, the momenta in the transversal plane are much smaller than the total momentum module, *i.e.*

$$(1+\delta)^2 \gg \left(P_x - \widetilde{A}_x\right)^2 + \left(P_y - \widetilde{A}_y\right)^2 ,$$

we can therefore introduce the so called paraxial approximation [Wol14, Chapter 3], that amounts to substituting the square root in equation (3.20) with its Taylor expansion truncated at the first order:

$$\begin{aligned} \widetilde{\mathcal{K}} &= -\sqrt{(\delta+1)^2 - \left(P_x - D_2\, \widetilde{A}_x\right)^2 - \left(P_y - D_2\, \widetilde{A}_y\right)^2} - D_2\, \widetilde{A}_z + P_z + \delta \\ &= -(\delta+1)\sqrt{1 - \frac{\left(P_x - D_2\, \widetilde{A}_x\right)^2}{(\delta+1)^2} - \frac{\left(P_y - D_2\, \widetilde{A}_y\right)^2}{(\delta+1)^2}} - D_2\, \widetilde{A}_z + P_z + \delta \\ &\approx -(\delta+1)\left(1 - \frac{\left(P_x - D_2\, \widetilde{A}_x\right)^2}{2(\delta+1)^2} - \frac{\left(P_y - D_2\, \widetilde{A}_y\right)^2}{2(\delta+1)^2}\right) - D_2\, \widetilde{A}_z + P_z + \delta \\ &= -1 + \frac{\left(P_x - D_2\, \widetilde{A}_x\right)^2}{2(\delta+1)} + \frac{\left(P_y - D_2\, \widetilde{A}_y\right)^2}{2(\delta+1)} - D_2\, \widetilde{A}_z + P_z \,. \end{aligned}$$

The resulting Hamiltonian with the paraxial approximation is therefore

$$\mathcal{K} = -1 + \frac{\left(P_x - D_2\, \widetilde{A}_x\right)^2}{2(\delta+1)} + \frac{\left(P_y - D_2\, \widetilde{A}_y\right)^2}{2(\delta+1)} - D_2\, \widetilde{A}_z + P_z \,. \tag{3.21}$$

For the Hamiltonian (3.21) we have that, for stationary fields, it is independent on the variable ℓ and therefore, the corresponding canonical momentum δ is constant. We also note that the term -1 in (3.21) does not affect the Hamilton equations and can therefore be neglected.

The Hamiltonian formulation described here, together with the associated numerical methods that will be introduced in the next chapter, will be used to compute the particle trajectories in the Section 5.1, devoted to the application to magnetic quadrupoles.

Chapter 4

Numerical approximations for electromagnetic problems

The solution of the problems introduced in the first two chapters is often not expressible in a closed form. We have therefore to employ numerical methods to approximate the analytic solution. This chapter is devoted to the presentation of the methods that will be applied in this thesis for this purpose. We will mainly focus on the numerical methods for the resolution of the Maxwell equations in a Galerkin framework and we will then discuss, in the last part of the chapter, the methods used to solve the Hamilton equations that will be applied to the computation of particle trajectories. Regarding the former task, we will consider well-posed problems involving a bilinear form which can be expressed as

Problem 4.1. *Find $x \in U$ such that, for $F \in U'$, we have that*

$$B(x, y) = F(y)\,, \quad y \in U\,,$$

where U, depending on the problem, is formed by one or two spaces V^k, belonging to an exact sequence (e.g. (2.35) or (2.50)).

The objective is then to build a conforming discretization, *i.e.* a set of finite-dimensional spaces, depending on a parameter h, such that $U_h \subset U$. Moreover, we require that the discrete spaces V_h^k form a subcomplex of the continuous one, meaning that they are conforming and that satisfy

$$d^k V_h^k \subset V_h^{k+1}\,. \tag{4.1}$$

The subscript h historically refers to a characteristic mesh size, but we will just consider it as a scalar discretization parameter with the property that the dimension of U_h is increasing for decreasing h. Moreover, we will also use the

subscript h to indicate quantities related to the finite-dimensional approximations. Since U is formed by one or two spaces V^k, we will build conforming discretizations for the spaces in the sequence, $V_h^k \subset V^k$, which lead to a conforming discretization for $U_h \subset U$. Thanks to the subcomplex property (4.1), we have that for each value of h the following finite-dimensional problem is well-posed [Arn18, Section 5.2.3]

Problem 4.2. *Find $x_h \in U_h$ such that, for $F \in U'$, we have that:*

$$B(x_h,\, y_h) = F(y_h)\,, \quad y_h \in U_h\,.$$

We would then like to have that the discrete solution x_h approximates the continuous one x for $h \to 0$. In this context, a crucial role is played by the following inequality [XZ03, Theorem 2]:

$$\|x - x_h\|_U \leq \frac{C}{\gamma_h} \inf_{y_h \in U_h} \|x - y_h\|_U\,. \tag{4.2}$$

where the γ_h is the discrete inf-sup constant [Arn18, Section 5.2.3]

$$\gamma_h = \inf_{0 \neq x \in U_h} \sup_{0 \neq y_h \in U_h} \frac{B(x_h,\, y_h)}{\|x_h\|_U \, \|y_h\|_U}\,. \tag{4.3}$$

From (4.2), we see that we are able to approximate the continuous solution x if we have a uniform lower bound for the discrete inf-sup constant (4.3) $\gamma_h \geq \gamma_0 > 0$ and we have the approximation property, *i.e.*

$$\lim_{h \to 0} \inf_{y_h \in U_h} \|x - y_h\|_U = 0\,, \quad x \in U\,. \tag{4.4}$$

Throughout the first part of this chapter, we will mainly deal with discretizations arising in IGA [CHB09], with a particular focus on a new method, proposed in this thesis, for the resolution of Maxwell equations in axisymmetric domains, which extends the strategy presented in [Oh15]. The key ingredients for this paradigm are the B-spline and the Non-Uniform Rational Basis Spline (NURBS) functions which are widely used in Computer Aided Design (CAD). The choice of the same functions used in CAD allows to exactly represent the domain geometry already at the coarsest discretization level and simplifies the step from design to computation, which is crucial since meshing and preprocessing steps take up to 80% of the time of the entire simulation workflow [Bog+05]. Moreover, B-splines allow a great flexibility in the choice of regularity, ensuring very good approximation properties and an efficient representation of smooth functions. We will therefore begin this chapter introducing B-splines and NURBS which will be used to describe the

geometry and the finite-dimensional approximation spaces. We will underline the main properties of these spaces both in Cartesian and cylindrical coordinates. Finally, we will describe two methods tailored to solve the Laplace problem in cylindrical domains, which will be used in a practically relevant application. The first one is used in the accelerator physics community and it is based on the classical solution via Bessel functions [Dra97, Section 15.3], while the second one is proposed in this thesis and it motivated by the need of handling a non-uniform behaviour of the solution in the longitudinal direction z. It is therefore based on the use of a B-spline basis in the longitudinal direction and of a spectral basis in the radial one.

In the final part of the chapter we focus instead on the presentation of some numerical methods for the resolution of Ordinary Differential Equations (ODEs), which often arise in the resolution of time-dependent problems, and, in particular, we consider the important class of Hamilton equations introduced in Chapter 3.

4.1 B-spline and NURBS

In this section, we briefly introduce the basic concepts of IGA in the context of electromagnetism following [Vei+16]. We will start with the definition of B-splines on a reference unit interval (0, 1) in the univariate case and we will introduce two standard type of projectors together with some error estimates, needed for the subsequent analysis. We will then introduce the extension of the above concepts, via tensor product, to the multivariate case and we will finally describe how to define B-spline and NURBS geometries.

Let us define the so called knot vector $\boldsymbol{\Xi}$, which is a sequence of ordered values that we consider, without loss of generality, between 0 and 1. In this thesis, we will consider only open knot vectors, which are characterized by the fact that the first $p+1$ knots are equal to 0 and the last $p+1$ knots are equal to 1, *i.e.*

$$\boldsymbol{\Xi} = \{\xi_1 = \ldots = \xi_{p+1} < \ldots < \xi_{n+1} = \ldots = \xi_{n+p+1}\}\,, \tag{4.5}$$

where n is an integer. B-splines are piecewise polynomials of degree p used to build the finite element spaces and the geometries that will be used in this thesis. They can be defined recursively using the well-known Cox-DeBoor formula. Starting from piecewise constant polynomials ($p = 0$)

$$\widehat{B}_i^0(\widehat{x}) = \begin{cases} 1 & \xi_i \leq \widehat{x} < \xi_{i+1} \\ 0 & \text{otherwise} \end{cases},$$

the higher degree polynomials ($p \geq 1$) are defined by

$$\widehat{B}_i^p(\widehat{x}) = \frac{\widehat{x} - \xi_i}{\xi_{i+p} - \xi_i} \widehat{B}_i^{p-1}(\widehat{x}) + \frac{\xi_{i+p+1} - \widehat{x}}{\xi_{i+p+1} - \xi_{i+1}} \widehat{B}_{i+1}^{p-1}(\widehat{x}) \,, \tag{4.6}$$

with the convention that $0/0$ is equal to 0. The number of B-splines obtained using this procedure is the number n in the definition of the knot vector (4.5). It is possible to describe the knot vector $\boldsymbol{\Xi}$ using other two vectors: a vector containing the knots without repetition (sometimes called breakpoints), that we indicate with $\boldsymbol{\zeta} \in \mathbb{R}^\ell$, and a vector containing the number of times each knot is repeated $1 \leq r_i \leq p$, $2 \leq i \leq \ell - 1$, with $r_1 = r_\ell = p + 1$. The number $\alpha_i = p - r_i$ denotes the regularity of the B-spline function at the knot ζ_i. In analogy to the standard Finite Element Method, we can use the breakpoints to define elements $I_i = (\zeta_i, \zeta_{i+1})$ of a mesh with the corresponding mesh size $h_i = \zeta_{i+1} - \zeta_i$, $1 \leq i \leq \ell - 1$. We say that the mesh, or the partition, defined by $\boldsymbol{\zeta}$ is locally quasi uniform if there exists a constant $\eta \geq 1$ such that

$$\eta^{-1} \leq \frac{h_i}{h_{i+1}} \leq \eta, \qquad 1 \leq i \leq \ell - 2. \tag{4.7}$$

The n B-spline polynomials generated by (4.6) are non-negative, *i.e.* $\widehat{B}_i^p(\widehat{x}) \geq 0$, they form a partition of unity, meaning that

$$\sum_{i=1}^{n} \widehat{B}_i^p(\widehat{x}) = 1 \,, \tag{4.8}$$

and they have local support. In particular, the support of the i-th B-spline is contained in the interval $[\xi_i, \xi_{i+p+1}]$, so the size of the support is reduced by knot repetitions (see Figure 4.2):

$$\widehat{B}_i^p(\widehat{x}) = 0 \qquad \widehat{x} \notin [\xi_i, \xi_{i+p+1}] \,.$$

Conversely, in each interval (ξ_j, ξ_{j+1}) there are exactly $p + 1$ B-splines which are different from 0:

$$\widehat{B}_i^p(\widehat{x}) = 0 \qquad \widehat{x} \in (\xi_j, \xi_{j+1}),\ i \notin \{j, j-1, \ldots, j-p\} \,.$$

Note that for each element I_i there exists a unique index k such that $I_i = (\zeta_i, \zeta_{i+1}) = (\xi_k, \xi_{k+1})$. This remark is useful to define the so called support extension $\widetilde{I}_i$, that is the interval formed by the interior of the union of the supports of the basis functions which have a non-empty intersection with I_i (see Figure 4.1):

$$\widetilde{I}_i = (\xi_{k-p}, \xi_{k+p+1}) \,. \tag{4.9}$$

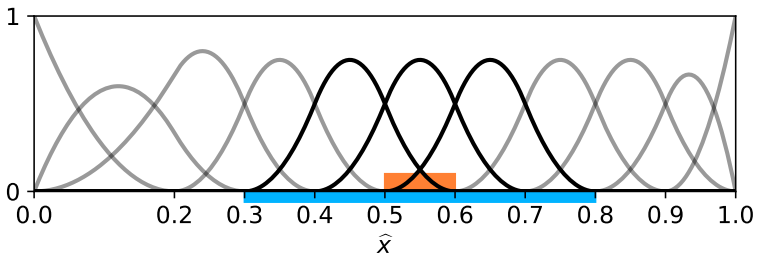

Figure 4.1: Representation of the support extension $\widetilde{I}_5 = (0.3, 0.8)$ (blue) of $I_5 = (0.5, 0.6)$ (orange). The support extension contains the support of all the basis functions that do not vanish on I_5.

We can now define the B-spline spaces as

$$S^p_{\boldsymbol{\alpha}}(\boldsymbol{\zeta}) = \text{span}\left\{\widehat{B}^p_i,\, i = 1,\, \ldots,\, n\right\}.$$

Note that B-spline spaces can be completely characterized either by the open knot vector $\boldsymbol{\Xi}$ or by the degree p, the mesh $\boldsymbol{\zeta}$ and the regularity $\boldsymbol{\alpha}$ (or the knot repetitions). For this reason we can use the two different notations $S^p_{\boldsymbol{\alpha}}(\boldsymbol{\zeta})$ and $S(\boldsymbol{\Xi})$ to indicate the same space. Figure 4.2 shows two sets of quadratic B-spline basis functions generated by two different knot vectors with the same elements but different regularity. To a B-spline space $S(\boldsymbol{\Xi})$

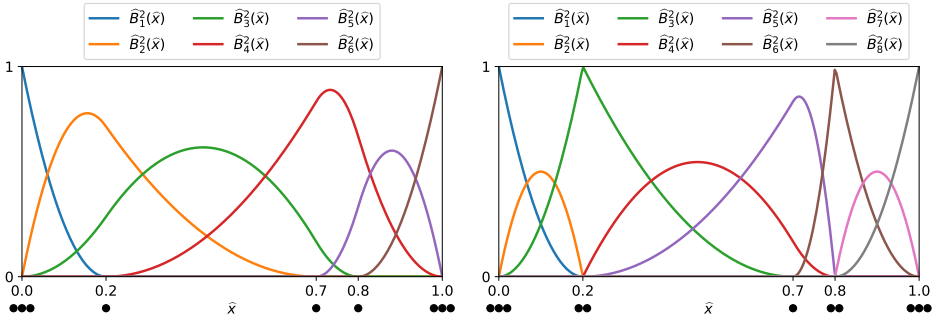

Figure 4.2: Two set of quadratic B-spline basis functions generated, respectively, from the knots $\boldsymbol{\Xi}^a = (0, 0, 0, 0.2, 0.7, 0.8, 1, 1, 1)$ (left) and $\boldsymbol{\Xi}^b = (0, 0, 0, 0.2, 0.2, 0.7, 0.8, 0.8, 1, 1, 1)$ (right). The dots below the ζ-axis indicate the knots repetitions. The two spaces are defined on the same mesh $\boldsymbol{\zeta} = (0, 0.2, 0.7, 0.8, 1)$, but the space on the left has higher regularity and less basis functions. Note that the support of the less regular B-splines (right) is smaller that the ones with higher regularity (left).

it is possible to associate a dual basis, *i.e.* a set of dual functionals $\lambda_{i,\,p}$,

$i = 1, \ldots, n$, which satisfy the property

$$\lambda_{i,p}(\widehat{B}_j^p) = \delta_{ij}\,, \qquad j = 1, \ldots, n$$

and that are stable, in the sense that

$$|\lambda_{i,p}(f)| \leq C\frac{1}{\sqrt{h_i}}\,\|f\|_{L^2(I_i)}\,.$$

An explicit construction of a dual basis with the proof of the aforementioned properties can be found in [Sch81, Section 4.6]. Using the dual basis, it is possible to define projectors

$$\begin{aligned} \Pi_{\boldsymbol{\Xi}} : L^2([0,\,1]) &\to S(\boldsymbol{\Xi}) \\ f &\mapsto \sum_{i=1}^{n} \lambda_{i,p}(f)\widehat{B}_i^p \end{aligned} \tag{4.10}$$

for which

$$\Pi_{\boldsymbol{\Xi}} v = v\,, \quad v \in S(\boldsymbol{\Xi})\,.$$

The defined projectors (4.10) are stable [Vei+16, Proposition 2.4], *i.e.*

$$\|\Pi_{\boldsymbol{\Xi}} u\|_{L^2(I_i)} \leq C_1\,\|u\|_{L^2(\widetilde{I}_i)}\,,$$

where C_1 depends only on p and, for a locally quasi-uniform partition, we have that

$$|\Pi_{\boldsymbol{\Xi}} u|_{H^1(I_i)} \leq C_2 |u|_{H^1(\widetilde{I}_i)}\,,$$

where C_2 depends only on p and η. In order to build proper discretizations for the de Rham complexes, it is important to see how the derivative operator acts on the B-spline spaces and to build projectors that commute with it. Concerning the former issue, we have that the derivative operator maps B-spline spaces onto B-spline spaces of lower degree. In particular, for $p \geq 1$ and $\alpha_i > 0$ on the internal break points $i = 2, \ldots, \ell - 1$, we have that

$$\left\{ \frac{\mathrm{d}}{\mathrm{d}\zeta} v :\ v \in S^p_{\boldsymbol{\alpha}}(\boldsymbol{\zeta}) \right\} \equiv S^{p-1}_{\boldsymbol{\alpha}-1}(\boldsymbol{\zeta})\,,$$

or, equivalently,

$$\left\{ \frac{\mathrm{d}}{\mathrm{d}\zeta} v :\ v \in S(\boldsymbol{\Xi}) \right\} \equiv S(\boldsymbol{\Xi}')\,, \tag{4.11}$$

where $\boldsymbol{\Xi}'$ is the knot vector obtained from $\boldsymbol{\Xi}$ removing the first and the last knots: $\{\xi_2, \ldots, \xi_{n+p}\}$. Given a projector in the form (4.10), it is possible to build another projector $\Pi^c_{\boldsymbol{\Xi}'}$, given by

$$\Pi^c_{\boldsymbol{\Xi}'} g = \frac{\mathrm{d}}{\mathrm{d}\zeta}\Pi_{\boldsymbol{\Xi}} \int_0^\zeta g(s)\mathrm{d}s\,, \quad g \in L^2(0,\,1)\,, \tag{4.12}$$

such that it commutes with the derivative operator, that is

$$\Pi^c_{\Xi'} \frac{\mathrm{d}}{\mathrm{d}\zeta} f = \frac{\mathrm{d}}{\mathrm{d}\zeta} \Pi_{\Xi} f \,, \quad f \in H^1(0,\,1)\,. \tag{4.13}$$

We have that (4.12) is indeed a projector, *i.e.*

$$\Pi^c_{\Xi'} v = v \,, \quad \in S(\Xi')\,.$$

and that it is stable on a quasi-uniform partition [Vei+16, Proposition 5.3]:

$$\|\Pi^c_{\Xi'} v\|_{L^2(I_i)} \leq C \|v\|_{L^2(\widetilde{I}_i)}\,. \tag{4.14}$$

The B-spline spaces are conforming in $H^1(0,\,1)$, *i.e.* without essential boundary conditions. Since the only non-vanishing basis functions on the left and right boundaries are, respectively, $\widehat{B}^p_1$ and $\widehat{B}^p_n$, it is possible to define conforming B-spline spaces and commuting projectors with analogous properties for $H^1_0(0,\,1)$ as well and for spaces with essential boundary conditions only on one extremum [Buf+11, Lemma 3.3, 3.5].

The analogous multivariate spaces are defined via tensor product. For a space of dimension d, we consider d knot vectors $\boldsymbol{\Xi}_s$, $s = 1,\,\ldots,\,d$, with the corresponding break points $\boldsymbol{\zeta}_s$, degrees p_s, regularity $\boldsymbol{\alpha}_s$ and univariate B-spline spaces $S(\boldsymbol{\Xi}_s)$. Assuming that each univariate partition, defined by $\boldsymbol{\zeta}_s$, is locally quasi uniform (4.7), we can defined the so called Bézier mesh on $\widehat{\Omega} = (0,\,1)^d$ given by

$$\widehat{\mathcal{Q}}_h = \{Q_{\boldsymbol{j}} = I_{j_1} \times \ldots \times I_{j_d}\,, 1 \leq j_s \leq \ell_s\,, s = 1,\,\ldots\,,d\},$$

where $\boldsymbol{j} = (j_1,\,\ldots,\,j_d)$ and $h = \max\left\{\mathrm{diam}(Q),\, Q \in \widehat{\mathcal{Q}}_h\right\}$ is the global mesh size. We will denote the the coarsest mesh with the subscript 0: $\widehat{\mathcal{Q}}_0$. In a straightforward manner, it is possible to define the support extension in the multivariate case, exploiting the definition in the univariate case (4.9):

$$\widetilde{Q}_{\boldsymbol{j}} = \widetilde{I}_{j_1} \times \ldots \times \widetilde{I}_{j_d}\,.$$

A multivariate B-spline is then defined as the product of the univariate ones:

$$\widehat{B}^{\boldsymbol{p}}_{\boldsymbol{i}}(\widehat{\boldsymbol{x}}) = \widehat{B}^{p_1}_{i_1}(\widehat{x}_1) \cdots \widehat{B}^{p_d}_{i_d}(\widehat{x}_d)\,,$$

and, consequently, the multivariate B-spline space is defined as

$$S(\boldsymbol{\Xi}_1,\,\ldots,\,\boldsymbol{\Xi}_d) = \mathrm{span}\left\{\widehat{B}^{\boldsymbol{p}}_{\boldsymbol{i}},\, 1 \leq i_s \leq n_s,\, s = 1,\,\ldots,\,d\right\}.$$

NURBS functions are a generalization of B-spline functions which can be built considering a set of weights $w_{\boldsymbol{i}} \geq 0,\ 1 \leq i_s \leq n_s,\ s = 1, \ldots, d$ such that they sum to one and using the following formula:

$$\widehat{N}^{\boldsymbol{p}}_{\boldsymbol{i}}(\widehat{\boldsymbol{x}}) = \frac{w_{\boldsymbol{i}} \widehat{B}^{\boldsymbol{p}}_{\boldsymbol{i}}(\widehat{\boldsymbol{x}})}{\sum_{\boldsymbol{i}} w_{\boldsymbol{i}} \widehat{B}^{\boldsymbol{p}}_{\boldsymbol{i}}(\widehat{\boldsymbol{x}})}\,.$$

Note that, if all the weights equal to one, the denominator is identically one as well, thanks to the property (4.8), and the obtained NURBS is actually simply a B-spline, proving the fact that NURBS are indeed a generalization of the B-splines, as stated above. Gathering the weights in a vector $\mathbf{W}$, the associated NURBS space is simply defined as

$$N(\boldsymbol{\Xi}_1, \ldots, \boldsymbol{\Xi}_d, \mathbf{W}) = \text{span}\left\{\widehat{N}^{\boldsymbol{p}}_{\boldsymbol{i}},\ 1 \leq i_s \leq n_s,\ s = 1, \ldots, d\right\}.$$

B-splines and NURBS can be used to define complex geometric shapes, they are indeed the main tool used in CAD. We will explain how a geometry is described considering NURBS since B-splines are a particular case. A geometric entity Ω, to which we will often refer as physical domain, is described using a parametrization $\boldsymbol{F}$ defined using a NURBS space and a set of vectorial coefficients $\mathbf{c}_{\boldsymbol{i}} \in \mathbb{R}^r\,,\ r \geq d$, called control points, which multiply each NURBS basis function:

$$\begin{aligned} \boldsymbol{F} : \widehat{\Omega} = (0,\ 1)^d &\to \Omega \subset \mathbb{R}^r \\ \boldsymbol{F}(\widehat{\boldsymbol{x}}) &= \sum_{\boldsymbol{i}} \mathbf{c}_{\boldsymbol{i}} \widehat{N}^{\boldsymbol{p}}_{\boldsymbol{i}}(\widehat{\boldsymbol{x}}) \end{aligned}$$

The dimension of the space d determines the dimension of the object: a curve ($d = 1$), a surface ($d = 2$) or a volume ($d = 3$). The number of the components $r \geq d$ of each coefficient $\mathbf{c}_{\boldsymbol{i}}$ determines instead the dimension of the ambient space, so, for example, if $d = 1$, $r = 2$ the geometry represents a curve on the plane and if $d = 2$ and $r = 3$ represents a surface in the three-dimensional space. In the following we will always consider $r = d$. The set of control points is called control grid or control mesh and the parametric Bézier mesh induces, through the parametrization $\boldsymbol{F}$, the physical Bézier mesh (see Figure 4.3):

$$\mathcal{Q}_h = \left\{K = \boldsymbol{F}(Q)\,,\ Q \in \widehat{\mathcal{Q}}_h\right\}.$$

We will now specify the types of parametrizations we will consider introducing the following assumption.

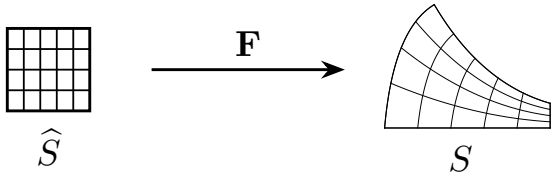

Figure 4.3: Representation of a parametric and physical Bézier mesh obtained through a parametrization $\boldsymbol{F}$, $(d = r = 2)$.

Assumption 4.1. *The parametrization $\boldsymbol{F}$ is defined on the coarsest level $\widehat{\mathcal{Q}}_0$ and its associated regularity vectors are $\boldsymbol{\beta}_i$, $i = 1, \dots, d$. We assume that $\boldsymbol{F}|_{\overline{Q}} \in C^\infty(\overline{Q})$, $Q \in \widehat{\mathcal{Q}}_0$ and $\boldsymbol{F}^{-1}|_{\overline{K}} \in C^\infty(\overline{K})$, $K \in \mathcal{Q}_0$. Moreover, when we will consider B-spline spaces, we assume that the regularity of the parametrization is higher than the regularity of the spaces. Finally, we assume that the Bésier meshes we will encounter are shape-regular, meaning that the ratio between the smallest edge and the diameter of each element $Q \in \widehat{\mathcal{Q}}_h$ is uniformly bounded with respect to h and Q [Buf+11, Section 3.4].*

4.1.1 Discrete spaces in Cartesian coordinates

In the previous section, we introduced the univariate B-spline spaces together with their multivariate extensions via tensor product on a reference, or parametric, domain $\widehat{\Omega}$ and we explained how NURBS geometries are defined through a parametrization $\boldsymbol{F}$. In this section, we will consider the de Rham complex (2.26) of spaces defined on a three-dimensional parametric domain $\widehat{\Omega} = (0, 1)^3$ and we will define the suitable B-spline discrete spaces that share some crucial properties of the continuous ones. We will then consider a regular parametrization of the three-dimensional physical domain Ω, described by a B-spline or by a NURBS volume, and we recall the results that allow to define discrete spaces corresponding to the spaces defined on the physical domain exploiting the ones defined on the reference one. Finally, we simply state the results for approximation of the two-dimensional de Rham complex in Cartesian coordinates, which follow from the three-dimensional ones, but this will be useful to set the notation which will then be used in the following section.

Consider the de Rham complex in Cartesian coordinates (2.34) defined on the parametric domain [Buf+11, Section 2]:

$$\mathbb{R} \longrightarrow \widehat{X}^0 \xrightarrow{\widehat{\mathbf{grad}}} \widehat{X}^1 \xrightarrow{\widehat{\mathbf{curl}}} \widehat{X}^2 \xrightarrow{\widehat{\mathrm{div}}} \widehat{X}^3 \longrightarrow 0 \ ,$$

where we have used the following compact notation to indicate the spaces:

$$\widehat{X}^0 = H^1(\widehat{\Omega})\,, \qquad \widehat{X}^1 = H(\widehat{\mathbf{curl}};\,\widehat{\Omega})\,,$$
$$\widehat{X}^2 = H(\widehat{\mathrm{div}};\,\widehat{\Omega})\,, \qquad \widehat{X}^3 = L^2(\widehat{\Omega})\,.$$

The first objective is to define a sequence of discrete spaces $\widehat{X}_h^k$, $k = 0, \ldots, 3$ with the subcomplex property (4.1), *i.e.* $\widehat{X}_h^k \subset X^k$ and

$$d^k(\widehat{X}_h^k) \subset \widehat{X}_h^{k+1}\,.$$

To this end we consider three know vectors $\boldsymbol{\Xi}_1$, $\boldsymbol{\Xi}_2$ and $\boldsymbol{\Xi}_3$ which define B-spline spaces with degree $p \geq 1$ which are at least continuous in the internal breakpoints $\alpha_i \geq 0$ and we introduce the following discrete spaces:

$$\begin{aligned}
\widehat{X}_h^0 &= S(\boldsymbol{\Xi}_1,\, \boldsymbol{\Xi}_2,\, \boldsymbol{\Xi}_3)\,,\\
\widehat{X}_h^1 &= S(\boldsymbol{\Xi}_1',\, \boldsymbol{\Xi}_2,\, \boldsymbol{\Xi}_3) \times S(\boldsymbol{\Xi}_1,\, \boldsymbol{\Xi}_2',\, \boldsymbol{\Xi}_3) \times S(\boldsymbol{\Xi}_1,\, \boldsymbol{\Xi}_2,\, \boldsymbol{\Xi}_3')\,,\\
\widehat{X}_h^2 &= S(\boldsymbol{\Xi}_1,\, \boldsymbol{\Xi}_2',\, \boldsymbol{\Xi}_3') \times S(\boldsymbol{\Xi}_1',\, \boldsymbol{\Xi}_2,\, \boldsymbol{\Xi}_3') \times S(\boldsymbol{\Xi}_1',\, \boldsymbol{\Xi}_2',\, \boldsymbol{\Xi}_3)\,,\\
\widehat{X}_h^3 &= S(\boldsymbol{\Xi}_1',\, \boldsymbol{\Xi}_2',\, \boldsymbol{\Xi}_3')\,.
\end{aligned} \tag{4.15}$$

Thanks to the B-spline property (4.11), it is easy to see check that each differential operator maps a B-spline space into the following one and, since B-spline spaces are piecewise polynomials, it is also clear that they are conforming, so that the discrete spaces form a subcomplex of the original one. Another important ingredient that ensures the stability of the Galerkin method and the fact that the discrete subcomplex has the same cohomology of the continuous one is the presence of bounded cochain projectors $\widehat{\Pi}^k$ [Arn18, Section 5.2.2], *i.e.* a set of projectors that satisfy

$$\|\widehat{\Pi}^k \widehat{v}\|_{\widehat{X}^k} \leq C \|\widehat{v}\|_{\widehat{X}^k}\,, \qquad \widehat{v} \in \widehat{X}^k$$

and that commute with the differential operators:

$$(d^k \circ \widehat{\Pi}^k)\widehat{v} = (\widehat{\Pi}^{k+1} \circ d^k)\widehat{v}\,, \qquad \widehat{v} \in \widehat{X}^k\,.$$

Using the subcomplex property and a set of commuting projectors we can draw the following commuting diagram (a representation of the complex formed by the discrete spaces (4.15) of maximum degree $p = 2$ is drawn in Figure 4.4):

$$\begin{array}{ccccccccccc}
\mathbb{R} & \longrightarrow & \widehat{X}^0 & \xrightarrow{\widehat{\mathbf{grad}}} & \widehat{X}^1 & \xrightarrow{\widehat{\mathbf{curl}}} & \widehat{X}^2 & \xrightarrow{\widehat{\mathrm{div}}} & \widehat{X}^3 & \longrightarrow & 0\\
 & & \downarrow{\scriptstyle \widehat{\Pi}^0} & & \downarrow{\scriptstyle \widehat{\Pi}^1} & & \downarrow{\scriptstyle \widehat{\Pi}^2} & & \downarrow{\scriptstyle \widehat{\Pi}^3} & & \\
\mathbb{R} & \longrightarrow & \widehat{X}_h^0 & \xrightarrow{\widehat{\mathbf{grad}}} & \widehat{X}_h^1 & \xrightarrow{\widehat{\mathbf{curl}}} & \widehat{X}_h^2 & \xrightarrow{\widehat{\mathrm{div}}} & \widehat{X}_h^3 & \longrightarrow & 0
\end{array} \tag{4.16}$$

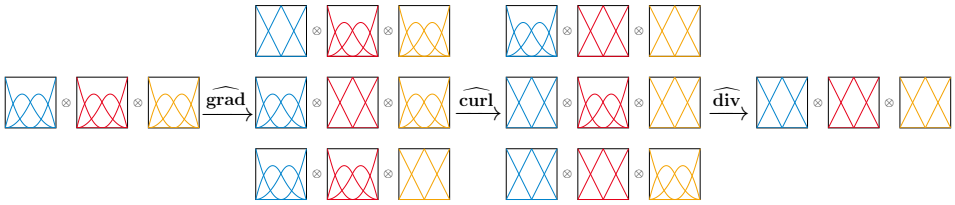

Figure 4.4: Representation of the complex formed by the discrete spaces with maximum degree $p = 2$.

Such projectors can be defined from (4.10) and (4.12) in the following way

$$\begin{aligned}
\widehat{\Pi}^0 &= \Pi_{\Xi_1} \otimes \Pi_{\Xi_2} \otimes \Pi_{\Xi_3}\,, \\
\widehat{\Pi}^1 &= (\Pi^c_{\Xi'_1} \otimes \Pi_{\Xi_2} \otimes \Pi_{\Xi_3}) \times (\Pi_{\Xi_1} \otimes \Pi^c_{\Xi'_2} \otimes \Pi_{\Xi_3}) \\
&\quad \times (\Pi_{\Xi_1} \otimes \Pi_{\Xi_2} \otimes \Pi^c_{\Xi'_3})\,, \\
\widehat{\Pi}^2 &= (\Pi_{\Xi_1} \otimes \Pi^c_{\Xi'_2} \otimes \Pi^c_{\Xi'_3}) \times (\Pi^c_{\Xi'_1} \otimes \Pi_{\Xi_2} \otimes \Pi^c_{\Xi'_3}) \\
&\quad \times (\Pi^c_{\Xi'_1} \otimes \Pi^c_{\Xi'_2} \otimes \Pi_{\Xi_3})\,, \\
\widehat{\Pi}^3 &= \Pi^c_{\Xi'_1} \otimes \Pi^c_{\Xi'_2} \otimes \Pi^c_{\Xi'_3}\,.
\end{aligned} \tag{4.17}$$

where the tensor product has to be interpreted as the composition of the various univariate projectors, as explained in [Vei+14, Section 2.2.2]. Thanks to the commuting property (4.13) of the univariate projectors (4.10) and (4.12), we have that the ones defined in (4.17) commute too [Vei+16, Lemma 5.7]:

$$\begin{aligned}
\widehat{\mathbf{grad}}\left(\widehat{\Pi}^0\,\widehat{v}\right) &= \widehat{\Pi}^1\left(\widehat{\mathbf{grad}}\,\widehat{v}\right), \\
\widehat{\mathbf{curl}}\left(\widehat{\Pi}^1\,\widehat{\boldsymbol{v}}\right) &= \widehat{\Pi}^2\left(\widehat{\mathbf{curl}}\,\widehat{\boldsymbol{v}}\right), \\
\widehat{\mathrm{div}}\left(\widehat{\Pi}^2\,\widehat{\boldsymbol{v}}\right) &= \widehat{\Pi}^3\left(\widehat{\mathrm{div}}\,\widehat{\boldsymbol{v}}\right).
\end{aligned} \tag{4.18}$$

Moreover, the stability of the projectors $\widehat{\Pi}^k$, on three-dimensional Bézier mesh obtained from quasi-uniform partitions, follows from the stability of the univariate ones (4.14) [Vei+16, Lemma 5.6]:

$$\begin{aligned}
\|\widehat{\Pi}^0\,\widehat{v}\|_{L^2(Q)} &\leq C\|\widehat{v}\|_{L^2(\widetilde{Q})}\,, & \widehat{v} &\in \widehat{X}^0\,, & Q &\in \widehat{\mathcal{Q}}\,, \\
\|\widehat{\Pi}^1\,\widehat{\boldsymbol{v}}\|_{L^2(Q;\mathbb{R}^3)} &\leq C\|\widehat{\boldsymbol{v}}\|_{L^2(\widetilde{Q};\mathbb{R}^3)}\,, & \widehat{\boldsymbol{v}} &\in \widehat{X}^1\,, & Q &\in \widehat{\mathcal{Q}}\,, \\
\|\widehat{\Pi}^2\,\widehat{\boldsymbol{v}}\|_{L^2(Q;\mathbb{R}^3)} &\leq C\|\widehat{\boldsymbol{v}}\|_{L^2(\widetilde{Q};\mathbb{R}^3)}\,, & \widehat{\boldsymbol{v}} &\in \widehat{X}^2\,, & Q &\in \widehat{\mathcal{Q}}\,, \\
\|\widehat{\Pi}^3\,\widehat{v}\|_{L^2(Q)} &\leq C\|\widehat{v}\|_{L^2(\widetilde{Q})}\,, & \widehat{v} &\in \widehat{X}^3\,, & Q &\in \widehat{\mathcal{Q}}\,.
\end{aligned} \tag{4.19}$$

Now that we have built a discretization for the spaces in the parametric domain, we would like to extend it to the spaces defined on the physical domain Ω. To this end, let us introduce the following notation to indicate the continuous spaces in the physical domain:

$$\begin{aligned} X^0 &= H^1(\Omega)\,, & X^1 &= H(\mathbf{curl};\,\Omega)\,, \\ X^2 &= H(\mathrm{div};\,\Omega)\,, & X^3 &= L^2(\Omega)\,. \end{aligned} \tag{4.20}$$

where the geometry Ω is described by a regular NURBS parametrization $\boldsymbol{F}$, in the sense specified in Assumption 4.1. Thanks to the regularity of the parametrization we can relate the functions in the parametric and physical domains by means of the following pull-backs:

$$\begin{aligned} \iota^0(v) &= v \circ \boldsymbol{F}\,, & & v \in X^0\,, \\ \iota^1(\boldsymbol{v}) &= {J_{\boldsymbol{F}}}^T(\boldsymbol{v} \circ \boldsymbol{F})\,, & & \boldsymbol{v} \in X^1\,, \\ \iota^2(\boldsymbol{v}) &= \det(J_{\boldsymbol{F}}){J_{\boldsymbol{F}}}^{-1}(\boldsymbol{v} \circ \boldsymbol{F})\,, & & \boldsymbol{v} \in X^2\,, \\ \iota^3(v) &= \det(J_{\boldsymbol{F}})(v \circ \boldsymbol{F})\,, & & v \in X^3\,. \end{aligned} \tag{4.21}$$

The pull-backs defined are such that the following diagram commutes:

$$\begin{array}{ccccccccccc} \mathbb{R} & \longrightarrow & X^0 & \xrightarrow{\mathbf{grad}} & X^1 & \xrightarrow{\mathbf{curl}} & X^2 & \xrightarrow{\mathrm{div}} & X^3 & \longrightarrow & 0 \\ & & \downarrow{\scriptstyle \iota^0} & & \downarrow{\scriptstyle \iota^1} & & \downarrow{\scriptstyle \iota^2} & & \downarrow{\scriptstyle \iota^3} & & \\ \mathbb{R} & \longrightarrow & \widehat{X}^0 & \xrightarrow{\widehat{\mathbf{grad}}} & \widehat{X}^1 & \xrightarrow{\widehat{\mathbf{curl}}} & \widehat{X}^2 & \xrightarrow{\widehat{\mathrm{div}}} & \widehat{X}^3 & \longrightarrow & 0 \end{array} \tag{4.22}$$

At this point the discrete spaces in the physical domain are simply induced by the ones in the parametric domain through the application of the corresponding push-forwards:

$$\begin{aligned} v &= \widehat{v} \circ \boldsymbol{F}^{-1}\,, & & v \in X^0\,,\ \widehat{v} \in \widehat{X}^0\,, \\ \boldsymbol{v} &= {J_{\boldsymbol{F}}}^{-T}\left(\widehat{\boldsymbol{v}} \circ \boldsymbol{F}^{-1}\right), & & \boldsymbol{v} \in X^1\,,\ \widehat{\boldsymbol{v}} \in \widehat{X}^1\,, \\ \boldsymbol{v} &= \frac{J_{\boldsymbol{F}}}{\det(J_{\boldsymbol{F}})}\left(\widehat{\boldsymbol{v}} \circ \boldsymbol{F}^{-1}\right), & & \boldsymbol{v} \in X^2\,,\ \widehat{\boldsymbol{v}} \in \widehat{X}^2\,, \\ v &= \frac{1}{\det(J_{\boldsymbol{F}})}\left(\widehat{v} \circ \boldsymbol{F}^{-1}\right), & & v \in X^2\,,\ \widehat{v} \in \widehat{X}^3\,. \end{aligned} \tag{4.23}$$

Consequently, the following relations between the differential operators in the parametric and in the physical domain hold:

$$\begin{aligned} \mathbf{grad}\ v &= {J_{\boldsymbol{F}}}^{-T}\left(\left(\widehat{\mathbf{grad}}\ \widehat{v}\right) \circ \boldsymbol{F}^{-1}\right), & & v \in X^0\,,\ \widehat{v} \in \widehat{X}^0 \\ \mathbf{curl}\ \boldsymbol{v} &= \frac{J_{\boldsymbol{F}}}{\det(J_{\boldsymbol{F}})}\left(\left(\widehat{\mathbf{curl}}\ \widehat{\boldsymbol{v}}\right) \circ \boldsymbol{F}^{-1}\right), & & \boldsymbol{v} \in X^1\,,\ \widehat{\boldsymbol{v}} \in \widehat{X}^1 \\ \mathrm{div}\ \boldsymbol{v} &= \frac{1}{\det(J_{\boldsymbol{F}})}\left(\left(\widehat{\mathrm{div}}\ \widehat{\boldsymbol{v}}\right) \circ \boldsymbol{F}^{-1}\right), & & \boldsymbol{v} \in X^2\,,\ \widehat{\boldsymbol{v}} \in \widehat{X}^2\,. \end{aligned} \tag{4.24}$$

The projectors as well are uniquely determined by the following relations:

$$\begin{aligned}
\Pi^0(v) &= \widehat{\Pi}^0\big(\iota^0(v)\big)\,, \quad v \in X^0\,,\\
\Pi^1(v) &= \widehat{\Pi}^1\big(\iota^1(v)\big)\,, \quad v \in X^1\,,\\
\Pi^2(v) &= \widehat{\Pi}^2\big(\iota^2(v)\big)\,, \quad v \in X^2\,,\\
\Pi^3(v) &= \widehat{\Pi}^3\big(\iota^3(v)\big)\,, \quad v \in X^3\,.
\end{aligned} \tag{4.25}$$

Moreover, we have that the following diagram for the physical domain commutes:

$$\begin{array}{ccccccccccc}
\mathbb{R} & \longrightarrow & X^0 & \xrightarrow{\textbf{grad}} & X^1 & \xrightarrow{\textbf{curl}} & X^2 & \xrightarrow{\text{div}} & X^3 & \longrightarrow & 0\\
 & & \downarrow{\scriptstyle \Pi^0} & & \downarrow{\scriptstyle \Pi^1} & & \downarrow{\scriptstyle \Pi^2} & & \downarrow{\scriptstyle \Pi^3} & & \\
\mathbb{R} & \longrightarrow & X_h^0 & \xrightarrow{\textbf{grad}} & X_h^1 & \xrightarrow{\textbf{curl}} & X_h^2 & \xrightarrow{\text{div}} & X_h^3 & \longrightarrow & 0
\end{array} \tag{4.26}$$

Finally, we define

$$p = \min\left(\{p_1,\, p_2,\, p_3\}\right)$$

and, with the Assumption 4.1 ensuring that the regularity of the parametrization $\boldsymbol{\beta}_i$ is higher than the one of the basis functions in (4.15) $\boldsymbol{\alpha}_i$, we have the following approximation estimates [Buf+11, Remark 5.1]:

$$\begin{aligned}
\|v - \Pi^0 v\|_{H^1(\Omega)} &\leq C\, h^s\, \|v\|_{H^{s+1}(\Omega)}\,, && v \in H^{s+1}(\Omega)\,,\\
\|\boldsymbol{v} - \Pi^1 \boldsymbol{v}\|_{H(\mathbf{curl};\,\Omega)} &\leq C\, h^s\, \|\boldsymbol{v}\|_{H^s(\mathbf{curl};\,\Omega)}\,, && \boldsymbol{v} \in H^s(\mathbf{curl};\,\Omega)\,,\\
\|\boldsymbol{v} - \Pi^2 \boldsymbol{v}\|_{H(\mathrm{div};\,\Omega)} &\leq C\, h^s\, \|\boldsymbol{v}\|_{H^s(\mathrm{div};\,\Omega)}\,, && \boldsymbol{v} \in H^s(\mathrm{div};\,\Omega)\,,\\
\|v - \Pi^3 v\|_{L^2(\Omega)} &\leq C\, h^s\, \|v\|_{H^s(\Omega)}\,, && v \in H^s(\Omega)\,,
\end{aligned} \tag{4.27}$$

where $0 \leq s \leq p$ and C is a constant independent on h. At this point, all the requirements to apply the theory presented in [Arn18] are fulfilled and we obtain the bound for the discrete inf-sup constant γ_h [Arn18, Theorem 5.4] which ensures the stability of the method. We are then able to properly approximate the solution of the problems presented in Section 2.2 and the estimates for the approximation error in (4.4) are obtained from (4.27) choosing, as finite-dimensional functions, the projection of the exact solution. The results presented in this section apply to a wider class of problems in which the considered sequences are not exact. The interested reader can found further details in [Arn18].

Two dimensional discrete spaces

Following the same passages we can state analogous results for the two-dimensional de Rham complexes in Cartesian coordinates (2.38). In this

case the parametrization that describes the geometry is the following:

$$\boldsymbol{F} : (0,\,1)^2 = \widehat{S} \to S \subset \mathbb{R}^2\,. \tag{4.28}$$

The B-spline spaces that approximate the de Rham complex in the parametric domain are

$$\begin{aligned}
\widehat{Y}_h^0 &= S(\Xi_1,\,\Xi_2)\,,\\
\widehat{Y}_h^1 &= S(\Xi_1',\,\Xi_2,\,) \times S(\Xi_1,\,\Xi_2')\,,\\
\widehat{Y}_h^{1*} &= S(\Xi_1,\,\Xi_2') \times S(\Xi_1',\,\Xi_2)\,,\\
\widehat{Y}_h^2 &= S(\Xi_1',\,\Xi_2')\,.
\end{aligned} \tag{4.29}$$

The relations (4.21) for the pull-back hold also in this case:

$$\begin{aligned}
\iota^0(v) &= v \circ \boldsymbol{F}\,, && v \in Y^0\,,\\
\iota^1(\boldsymbol{v}) &= {J_{\boldsymbol{F}}}^T(\boldsymbol{v} \circ \boldsymbol{F})\,, && \boldsymbol{v} \in Y^1\,,\\
\iota^{1*}(\boldsymbol{v}) &= \det\left(J_{\boldsymbol{F}}\right){J_{\boldsymbol{F}}}^{-1}(\boldsymbol{v} \circ \boldsymbol{F})\,, && \boldsymbol{v} \in Y^{1*}\,,\\
\iota^2(v) &= \det\left(J_{\boldsymbol{F}}\right)(v \circ \boldsymbol{F})\,, && v \in Y^2\,.
\end{aligned} \tag{4.30}$$

Thanks to the isomorphism between Y^1 and Y^{1*} (2.38), we have the following relations between ι^1 and ι^{1*}:

$$\begin{aligned}
\iota^1(\boldsymbol{v}) &= \mathbf{P}^{-1}\,\iota^{1*}(\mathbf{P}\,\boldsymbol{v})\,, && \boldsymbol{v} \in Y^1\,,\\
\iota^{1*}(\boldsymbol{v}) &= \mathbf{P}\,\iota^1(\mathbf{P}^{-1}\,\boldsymbol{v})\,, && \boldsymbol{v} \in Y^{1*}\,.
\end{aligned}$$

The discrete spaces in the physical domain are obtained through the application of the corresponding push-forwards:

$$\begin{aligned}
v &= \widehat{v} \circ \boldsymbol{F}^{-1}\,, && v \in Y^0\,,\ \widehat{v} \in \widehat{Y}^0\,,\\
\boldsymbol{v} &= {J_{\boldsymbol{F}}}^{-T}\left(\widehat{\boldsymbol{v}} \circ \boldsymbol{F}^{-1}\right), && \boldsymbol{v} \in Y^1\,,\ \widehat{\boldsymbol{v}} \in \widehat{Y}^1\,,\\
\boldsymbol{v} &= \frac{J_{\boldsymbol{F}}}{\det\left(J_{\boldsymbol{F}}\right)}\left(\widehat{\boldsymbol{v}} \circ \boldsymbol{F}^{-1}\right), && \boldsymbol{v} \in Y^{1*}\,,\ \widehat{\boldsymbol{v}} \in \widehat{Y}^{1*}\,,\\
v &= \frac{1}{\det\left(J_{\boldsymbol{F}}\right)}\left(\widehat{v} \circ \boldsymbol{F}^{-1}\right), && v \in Y^2\,,\ \widehat{v} \in \widehat{Y}^2\,.
\end{aligned} \tag{4.31}$$

The differential operators are related, analogously to the ones in the three-dimensional spaces (4.24), by the following equations:

$$\begin{aligned}
\mathbf{grad}\ v &= {J_{\boldsymbol{F}}}^{-T}\left(\left(\widehat{\mathbf{grad}}\ \widehat{v}\right) \circ \boldsymbol{F}^{-1}\right), && v \in Y^0\,,\ \widehat{v} \in \widehat{Y}^0\,,\\
\mathbf{rot}\ v &= \frac{J_{\boldsymbol{F}}}{\det\left(J_{\boldsymbol{F}}\right)}\left(\left(\widehat{\mathbf{rot}}\ \widehat{v}\right) \circ \boldsymbol{F}^{-1}\right), && v \in Y^0\,,\ \widehat{v} \in \widehat{Y}^0\,,\\
\operatorname{curl}\ \boldsymbol{v} &= \frac{1}{\det\left(J_{\boldsymbol{F}}\right)}\left(\left(\widehat{\operatorname{curl}}\ \widehat{\boldsymbol{v}}\right) \circ \boldsymbol{F}^{-1}\right), && \boldsymbol{v} \in Y^1\,,\ \widehat{\boldsymbol{v}} \in \widehat{Y}^1\,,\\
\operatorname{div}\ \boldsymbol{v} &= \frac{1}{\det\left(J_{\boldsymbol{F}}\right)}\left(\left(\widehat{\operatorname{div}}\ \widehat{\boldsymbol{v}}\right) \circ \boldsymbol{F}^{-1}\right), && \boldsymbol{v} \in Y^{1*}\,,\ \widehat{\boldsymbol{v}} \in \widehat{Y}^{1*}\,.
\end{aligned} \tag{4.32}$$

Analogous approximation estimates hold for the two-dimensional case:

$$\begin{aligned}
&\|v - \Pi^0 v\|_{H^1(S)} && \leq C\, h^s\, \|v\|_{H^{s+1}(S)}\,, && v \in H^{s+1}(S)\,,\\
&\|\boldsymbol{v} - \Pi^1 \boldsymbol{v}\|_{H(\mathrm{curl};\, S)} && \leq C\, h^s\, \|\boldsymbol{v}\|_{H^s(\mathrm{curl};\, S)}\,, && \boldsymbol{v} \in H^s(\mathrm{curl};\, S)\,,\\
&\|\boldsymbol{v} - \Pi^{1*} \boldsymbol{v}\|_{H(\mathrm{div};\, S)} && \leq C\, h^s\, \|\boldsymbol{v}\|_{H^s(\mathrm{div};\, S)}\,, && \boldsymbol{v} \in H^s(\mathrm{div};\, S)\,,\\
&\|v - \Pi^2 v\|_{L^2(S)} && \leq C\, h^s\, \|v\|_{H^s(S)}\,, && v \in H^s(S)\,.
\end{aligned} \tag{4.33}$$

The results presented in this sections applies also to the discretization of spaces in which essential boundary conditions are imposed on whole edges ($d = 2$) or faces ($d = 3$) of the parametrized domain [Buf+11] and on multipatch domains which allows to describe more complex domains [Vei+16, Section 3.3].

4.1.2 Discrete spaces in axisymmetric domains

In this section, we present one of the main contributions of this thesis, which is the extension of the results presented in [Oh15] to the IGA framework, defining proper discrete spaces of high order B-splines for the de Rham complex (2.50) when $m \neq 0$. Other works that studied numerical methods for the solution of specific problems in axisymmetric domains are, for example, [Ber+99; HL05; Lac00; MR82; Nke05; Per+17]. The main idea is to exploit the two-dimensional spaces in Cartesian coordinates (2.36), for which we are able to build proper discretizations with bounded cochain projectors and we have approximation estimates, to build a proper discretizations for the complex (2.50) by means of suitable operators. In the following, we will use the notation introduced in Section 2.3, *i.e.*

$$\|\cdot\| = \|\cdot\|_{L^2(S)} \quad \text{and} \quad \|\cdot\|_\rho = \|\cdot\|_{L^2_\rho(S)}\,.$$

In particular, the domain S will be the two-dimensional cross-section of our axisymmetric domain $\breve{\Omega}$ and we assume it is described through a regular NURBS parametrization $\boldsymbol{F}$ (4.28) that satisfies Assumption 4.1. The strategy to define the discrete counterparts of (2.49) is based on the use of operators that link the spaces in cylindrical coordinates to the standard spaces in Cartesian coordinates. The definition of the discrete spaces and of the projectors, together with error estimates, are then deduced from the ones defined for the spaces in Cartesian coordinates. A diagram summarizing the general strategy for the discretization that will be explained in the following

is depicted here:

$$
\begin{array}{ccccccc}
Z^{m,0} & \xrightarrow{\mathbf{grad}^m} & Z^{m,1} & \xrightarrow{\mathbf{curl}^m} & Z^{m,2} & \xrightarrow{\mathrm{div}^m} & Z^{m,3} \\
\downarrow{\scriptstyle \eta_{m,0}} & & \downarrow{\scriptstyle \eta_{m,1}} & & \downarrow{\scriptstyle \eta_{m,2}} & & \downarrow{\scriptstyle \eta_{m,3}} \\
Y^0 & \xrightarrow{\boldsymbol{G}} & Y^1 \times Y^0 & \xrightarrow{\boldsymbol{C}} & Y^{1*} \times Y^2 & \xrightarrow{D} & Y^2 \\
\downarrow{\scriptstyle \Pi^0} & & \downarrow{\scriptstyle \Pi^1 \times \Pi^0} & & \downarrow{\scriptstyle \Pi^{1*} \times \Pi^2} & & \downarrow{\scriptstyle \Pi^2} \\
Y_h^0 & \xrightarrow{\boldsymbol{G}} & Y_h^1 \times Y_h^0 & \xrightarrow{\boldsymbol{C}} & Y_h^{1*} \times Y_h^2 & \xrightarrow{D} & Y_h^2 \\
\downarrow{\scriptstyle \eta_{m,0}^{-1}} & & \downarrow{\scriptstyle \eta_{m,1}^{-1}} & & \downarrow{\scriptstyle \eta_{m,2}^{-1}} & & \downarrow{\scriptstyle \eta_{m,3}^{-1}} \\
Z_h^{m,0} & \xrightarrow{\mathbf{grad}^m} & Z_h^{m,1} & \xrightarrow{\mathbf{curl}^m} & Z_h^{m,2} & \xrightarrow{\mathrm{div}^m} & Z_h^{m,3}
\end{array}
\tag{4.34}
$$

The first step is the definition of a set of operators $\eta_{m,k},\ k = 0,\ 1,\ 2,\ 3$ that maps functions from $Z^{m,k}$ onto the functional spaces defined in Cartesian coordinates:

$$\eta_{m,0} : Z^{m,0} \to Y^0, \qquad u \mapsto \frac{m}{\rho} u, \tag{4.35}$$

$$\eta_{m,1} : Z^{m,1} \to Y^1 \times Y^0, \qquad \boldsymbol{u} \mapsto \begin{bmatrix} \dfrac{1}{\rho}(m\, u_\rho + u_\theta) \\ \dfrac{m}{\rho} u_z \\ u_\theta \end{bmatrix}, \tag{4.36}$$

$$\eta_{m,2} : Z^{m,2} \to Y^{1*} \times Y^2, \qquad \boldsymbol{u} \mapsto \begin{bmatrix} u_\rho \\ u_z \\ \dfrac{1}{\rho}(m u_\theta - u_\rho) \end{bmatrix}, \tag{4.37}$$

$$\eta_{m,3} : Z^{m,3} \to Y^2, \qquad u \mapsto u. \tag{4.38}$$

These operators are chosen such that $\boldsymbol{G}$, $\boldsymbol{C}$ and D are both well-defined and make the top part of the diagram (4.34) commutative. From the general strategy depicted in (4.34) and from the operators defined above, it is clear how the meridian and azimuthal components are treated differently and how the uncommon ordering of the components simplifies the notation. Note that, if $\Gamma^0 \neq \emptyset$ (2.42), these operators are well-defined only on regular subspaces

$\widetilde{Z}^{m,k} \subset Z^{m,k}$:

$$\begin{aligned}
\widetilde{Z}^{m,0} &= \left\{u \in Z^{m,0} : \ \eta_{m,0}(u) \in Y^0\right\} , \\
\widetilde{Z}^{m,1} &= \left\{\boldsymbol{u} \in Z^{m,1} : \ \eta_{m,1}(\boldsymbol{u}) \in Y^1 \times Y^0\right\} , \\
\widetilde{Z}^{m,2} &= \left\{\boldsymbol{u} \in Z^{m,2} : \ \eta_{m,2}(\boldsymbol{u}) \in Y^{1*} \times Y^2\right\} , \\
\widetilde{Z}^{m,3} &= \left\{u \in Z^{m,3} : \ \eta_{m,3}(u) \in Y^2\right\} .
\end{aligned} \tag{4.39}$$

Then, since proper conforming discretizations are known for the spaces in Cartesian coordinates (2.36), the discrete spaces $Z_h^{m,k}$ are built from the Cartesian discrete spaces using $\eta_{m,k}^{-1}$:

$$\begin{aligned}
Z_h^{m,0} &= \left\{u_h \mid u_h = \eta_{m,0}^{-1}(\widetilde{u}_h), \ \widetilde{u}_h \in Y_h^0\right\} , \\
Z_h^{m,1} &= \left\{\boldsymbol{u}_h \mid \boldsymbol{u}_h = \eta_{m,1}^{-1}(\widetilde{\boldsymbol{u}}_h), \ \widetilde{\boldsymbol{u}}_h \in Y_h^1 \times Y_h^0\right\} , \\
Z_h^{m,2} &= \left\{\boldsymbol{u}_h \mid \boldsymbol{u}_h = \eta_{m,2}^{-1}(\widetilde{\boldsymbol{u}}_h), \ \widetilde{\boldsymbol{u}}_h \in Y_h^{1*} \times Y_h^2\right\} , \\
Z_h^{m,3} &= \left\{u_h \mid u_h = \eta_{m,3}^{-1}(\widetilde{u}_h), \ \widetilde{u}_h \in Y_h^2\right\}.
\end{aligned} \tag{4.40}$$

Consistently with this definition, in the following we will denote functions defined on spaces in Cartesian coordinates with a tilde. Moreover, we will often treat differently the meridian and azimuthal components of a vector-valued functions and thus we will use the compact notation $\boldsymbol{u}_{\rho z} = (u_\rho, \, u_z)^T$, already introduced in Section 2.3, to indicate the former. In order to apply the differential operators to the discrete functions, it is useful to define, by composition, the following operators that act directly on the continuous spaces defined in Cartesian coordinates:

$$\begin{aligned}
\mathbf{grad}_\star^m &= \eta_{m,0}^{-1} \circ \mathbf{grad}^m : Y^0 \to Z^{m,1} , \\
\mathbf{grad}_\star^m \left(\widetilde{u}\right) &= \begin{bmatrix} \dfrac{1}{m}(\widetilde{u} + \rho \, \partial_\rho \widetilde{u}) \\ \dfrac{\rho}{m} \partial_z \widetilde{u} \\ -\widetilde{u} \end{bmatrix} ,
\end{aligned} \tag{4.41}$$

$$\begin{aligned}
\mathbf{curl}_\star^m &= \eta_{m,1}^{-1} \circ \mathbf{curl}^m : Y^1 \times Y^0 \to Z^{m,2} , \\
\mathbf{curl}_\star^m \left(\widetilde{\boldsymbol{u}}\right) &= \begin{bmatrix} -\widetilde{u}_z - \partial_z \widetilde{u}_\theta \\ \widetilde{u}_\rho + \partial_\rho \widetilde{u}_\theta \\ \dfrac{1}{m}(\partial_z(\rho \, \widetilde{u}_\rho) - \partial_\rho(\rho \, \widetilde{u}_z) - \partial_z \widetilde{u}_\theta) \end{bmatrix} ,
\end{aligned} \tag{4.42}$$

$$\begin{aligned}
\mathrm{div}_\star^m &= \eta_{m,2}^{-1} \circ \mathrm{div}^m : Y^{1*} \times Y^2 \to Z^{m,3} , \\
\mathrm{div}_\star^m \left(\widetilde{\boldsymbol{u}}\right) &= \partial_\rho \widetilde{u}_\rho - \widetilde{u}_\theta + \partial_z \widetilde{u}_z \ .
\end{aligned} \tag{4.43}$$

Note that, due to the choice of the spaces in Cartesian coordinates, all the differential operators (4.41)−(4.43) are well-defined. Moreover, since the discrete spaces in Cartesian coordinates are conforming, we have the following result:

Lemma 4.1. *The discrete spaces* (4.40) *are conforming in the spaces defined in* (2.49).

Proof. We have to show that $Z_h^{m,k} \subset Z^{m,k}$, $k = 0, \ldots, 3$. Due to the boundness of S, there exist $R > 0$ such that $0 < \rho < R$, $(\rho, z) \in S$. Considering $\widetilde{u}_h \in Y_h^0$, we have that $\widetilde{u}_h \in Y^0$ because of the conforming discretization of the Cartesian complexes (2.36). So $u_h \in Z^{m,0}$, in fact:

$$\|u_h\|_\rho^2 = \|\rho \widetilde{u}_h\|_\rho^2 \leq R^3 \, \|\widetilde{u}_h\|^2 < \infty$$

and

$$\begin{aligned} \|\mathbf{grad}^m \, u_h\|_\rho^2 = \|\mathbf{grad}_\star^m \, \widetilde{u}_h\|_\rho^2 &\leq R \, \|\mathbf{grad}_\star^m \, \widetilde{u}_h\|^2 \\ &\leq 3R \, \|\widetilde{u}_h\|^2 + 2R^3 \, \|\mathbf{grad} \, \widetilde{u}_h\|^2 < \infty \end{aligned}$$

since $\widetilde{u}_h \in Y^0$.
The proofs of the other cases are similar. For $Z_h^{m,1} \subset Z^{m,1}$, given $\boldsymbol{u}_h \in Z_h^{m,1}$ we have:

$$\begin{aligned} \|\boldsymbol{u}_h\|_\rho^2 = \left\| \frac{1}{m} (\rho \, \widetilde{u}_{\rho,h} - \widetilde{u}_{\theta,h}) \right\|_\rho^2 + \left\| \frac{\rho}{m} \widetilde{u}_{z,h} \right\|_\rho^2 + \|\widetilde{u}_{\theta,h}\|_\rho^2 \\ \leq 2R^3 \, \|\widetilde{u}_{\rho,h}\|^2 + R^3 \, \|\widetilde{u}_{z,h}\|^2 + 3R \, \|\widetilde{u}_{\theta,h}\|^2 < \infty \end{aligned}$$

and

$$\begin{aligned} \|\mathbf{curl}^m \, \boldsymbol{u}_h\|_\rho^2 &= \|\mathbf{curl}_\star^m \, \widetilde{\boldsymbol{u}}_h\|_\rho^2 \\ &= \|\widetilde{\boldsymbol{u}}_{\rho z,h} + \mathbf{grad} \, \widetilde{u}_{\theta,h}\|_\rho^2 \\ &+ \left\| \frac{1}{m} (-\rho \, \mathrm{curl} \, \widetilde{\boldsymbol{u}}_{\rho z,h} - \widetilde{u}_{z,h} - \partial_z \widetilde{u}_{\theta,h}) \right\|_\rho^2 \\ &\leq 6 \, \|\widetilde{\boldsymbol{u}}_{\rho z,h}\|_\rho^2 + 4 \, \|\rho \, \mathrm{curl} \, \widetilde{\boldsymbol{u}}_{\rho z,h}\|_\rho^2 + 4 \, \|\mathbf{grad} \, \widetilde{u}_{\theta,h}\|_\rho^2 \\ &\leq 6R \, \|\widetilde{\boldsymbol{u}}_{\rho z,h}\|^2 + 4R^3 \, \|\mathrm{curl} \, \widetilde{\boldsymbol{u}}_{\rho z,h}\|^2 + 4R \, \|\mathbf{grad} \, \widetilde{u}_{\theta,h}\|^2 < \infty \end{aligned}$$

since $\widetilde{\boldsymbol{u}}_{\rho z,h} \in Y^1$ and $\widetilde{u}_{\theta,h} \in Y^0$.
For $Z_h^{m,2} \subset Z^{m,2}$, given $\boldsymbol{u}_h \in Z_h^{m,2}$ we have:

$$\begin{aligned} \|\boldsymbol{u}_h\|_\rho^2 = \|\widetilde{\boldsymbol{u}}_{\rho z,h}\|_\rho^2 + \left\| \frac{1}{m} (\rho \, \widetilde{u}_{\theta,h} + \widetilde{u}_{\rho,h}) \right\|_\rho^2 \\ \leq 3R \, \|\widetilde{\boldsymbol{u}}_{\rho z,h}\|^2 + 2R^3 \, \|\widetilde{u}_{\theta,h}\|^2 < \infty \end{aligned}$$

and

$$\begin{aligned}\|\mathrm{div}^m \boldsymbol{u}_h\|_\rho^2 = \|\mathrm{div}_\star^m \widetilde{\boldsymbol{u}}_h\|_\rho^2 &\leq 2\ \|\mathrm{div}\, \widetilde{\boldsymbol{u}}_{\rho z,\,h}\|_\rho^2 + 2\ \|\widetilde{u}_{\theta,\,h}\|_\rho^2 \\ &\leq 2R\ \|\mathrm{div}\, \widetilde{\boldsymbol{u}}_{\rho z,\,h}\|^2 + 2R\ \|\widetilde{u}_{\theta,\,h}\|^2 < \infty\end{aligned}$$

since $\widetilde{\boldsymbol{u}}_{\rho z,\,h} \in Y^{1*}$ and $\widetilde{u}_{\theta,\,h} \in Y^2$.
Finally, $Z_h^{m,3} \subset Z^{m,3}$, given $u_h \in Z_h^{m,3}$, we have:

$$\|u_h\|_\rho^2 = \|\widetilde{u}_h\|_\rho^2 \leq R\ \|\widetilde{u}_h\|^2 < \infty$$

since $\widetilde{u}_h \in Y^2$. □

The projectors $\breve{\Pi}^{m,k} : \widetilde{Z}^{m,k} \to Z_h^{m,k}$ are defined as in [Oh15], exploiting those used in the spaces in Cartesian coordinates (2.36):

$$\begin{aligned}
\breve{\Pi}^{m,0} u &= \big(\eta_{m,0}^{-1} \circ \Pi^0 \circ \eta_{m,0}\big)(u)\ , && u \in \widetilde{Z}^{m,0}\ , \\
\breve{\Pi}^{m,1} \boldsymbol{u} &= \big(\eta_{m,1}^{-1} \circ \big(\Pi^1 \times \Pi^0\big) \circ \eta_{m,1}\big)(\boldsymbol{u})\ , && \boldsymbol{u} \in \widetilde{Z}^{m,1}\ , \\
\breve{\Pi}^{m,2} \boldsymbol{u} &= \big(\eta_{m,2}^{-1} \circ \big(\Pi^{1*} \times \Pi^2\big) \circ \eta_{m,2}\big)(\boldsymbol{u})\ , && \boldsymbol{u} \in \widetilde{Z}^{m,2}\ , \\
\breve{\Pi}^{m,3} u &= \big(\eta_{m,3}^{-1} \circ \Pi^2 \circ \eta_{m,3}\big)(u) = \Pi^2(u)\ , && u \in \widetilde{Z}^{m,3}\ .
\end{aligned} \tag{4.44}$$

The following lemma shows that they are actually projectors.

Lemma 4.2. *The interpolators* (4.44) *are projectors, that is*

$$\breve{\Pi}^k u_h = u_h\ , \qquad u_h \in Z_h^k\ , \qquad k = 0,\, \ldots,\, 3\ . \tag{4.45}$$

Proof. For $k = 3$ the result is immediate since the projector coincides with the one defined on the Cartesian space.
Also the result for $k = 0,\, \ldots,\, 2$ follows easily from the definition of the spaces and the results in Cartesian coordinates. Taking, for example, $u_h \in Z_h^0$, we have that

$$\breve{\Pi}^0 u_h = \eta_{m,0}^{-1}\big(\Pi^0(\widetilde{u}_h)\big) = \eta_{m,0}^{-1}(\widetilde{u}_h) = u_h\ , \quad \widetilde{u}_h \in Y_h^0\ .$$

□

We want now to show that the continuous and discrete spaces, together with the projectors, form a commutative diagram. We start proving the commutativity of the top part of the diagram (4.34).

Lemma 4.3. *The following diagram commutes:*

$$\begin{array}{ccccccc}
\widetilde{Z}^{m,0} & \xrightarrow{\mathbf{grad}^m} & \widetilde{Z}^{m,1} & \xrightarrow{\mathbf{curl}^m} & \widetilde{Z}^{m,2} & \xrightarrow{\mathrm{div}^m} & \widetilde{Z}^{m,3} \\
\downarrow{\scriptstyle \eta_{m,0}} & & \downarrow{\scriptstyle \eta_{m,1}} & & \downarrow{\scriptstyle \eta_{m,2}} & & \downarrow{\scriptstyle \eta_{m,3}} \\
Y^0 & \xrightarrow{\boldsymbol{G}} & Y^1 \times Y^0 & \xrightarrow{\boldsymbol{C}} & Y^{1*} \times Y^2 & \xrightarrow{D} & Y^2
\end{array}$$

Proof. For the first part involving the gradient, we have that $(\eta_{m,1} \circ \mathbf{grad}^m)u = (\mathbf{G} \circ \eta_{m,0})u$, $u \in \widetilde{Z}^{m,0}$. In fact, in the left-hand side we have that

$$\begin{aligned}
\mathbf{grad}^m u &= \left(\partial_\rho u,\, \partial_z u,\, -\frac{m}{\rho}u\right)^T, \\
\eta_{m,1} \circ \mathbf{grad}^m u &= \left(\frac{1}{\rho}\left(m\,\partial_\rho u - \frac{m}{\rho}u\right),\, \frac{m}{\rho}\partial_z u,\, -\frac{m}{\rho}u\right)^T \\
&= \left(\partial_\rho\left(\frac{m}{\rho}u\right),\, \partial_z\left(\frac{m}{\rho}u\right),\, -\frac{m}{\rho}u\right)^T,
\end{aligned}$$

which is clearly equal to the right-hand side, since $\eta_{m,0}u = \frac{m}{\rho}u \in Y^0$, and belongs to $Y^1 \times Y^0$.
For the part involving the curl $(\eta_{m,2} \circ \mathbf{curl}^m)\boldsymbol{u} = (\mathbf{C} \circ \eta_{m,1})\boldsymbol{u}$, $\boldsymbol{u} \in \widetilde{Z}^{m,1}$. In fact, in the left-hand side we have

$$\begin{aligned}
\mathbf{curl}^m \boldsymbol{u} &= \begin{bmatrix} -\dfrac{m}{\rho}u_z - \partial_z u_\theta \\ \dfrac{1}{\rho}(\partial_\rho(\rho\, u_\theta) + m\, u_\rho) \\ \partial_z u_\rho - \partial_\rho u_z \end{bmatrix}, \\
\eta_{m,2} \circ \mathbf{curl}^m \boldsymbol{u} &= \begin{bmatrix} -\dfrac{m}{\rho}u_z - \partial_z u_\theta \\ \dfrac{1}{\rho}(u_\theta + m\, u_\rho) + \partial_\rho u_\theta \\ \dfrac{1}{\rho}\left(m\partial_z u_\rho - m\partial_\rho u_z + \dfrac{m}{\rho}u_z + \partial_z u_\theta\right) \end{bmatrix} \\
&= \begin{bmatrix} -\dfrac{m}{\rho}u_z - \partial_z u_\theta \\ \dfrac{1}{\rho}(u_\theta + m\, u_\rho) + \partial_\rho u_\theta \\ -\partial_\rho\left(\dfrac{m}{\rho}u_z\right) + \partial_z\left(\dfrac{1}{\rho}(m\, u_\rho + u_\theta)\right) \end{bmatrix},
\end{aligned} \tag{4.46}$$

which is equal to the right-hand side $\mathbf{C} \circ \eta_{m,1}\boldsymbol{u}$ which belongs to $Y^{1*} \times Y^2$.
Finally, for the divergence part, we have that $(\eta_{m,3} \circ \mathrm{div}^m)\boldsymbol{u} = (D \circ \eta_{m,2})\boldsymbol{u}$, $\boldsymbol{u} \in \widetilde{Z}^{m,2}$. In fact, in the left-hand side we have:

$$\eta_{m,3} \circ \mathrm{div}^m \boldsymbol{u} = \mathrm{div}^m \boldsymbol{u} = \partial_\rho u_\rho + \partial_z u_z - \frac{1}{\rho}(m\, u_\theta - u_\rho)$$

which belongs to Y^2 and is clearly equal to the right-hand side, since

$$\eta_{m,2}\boldsymbol{u} = \left(u_\rho,\, u_z,\, \frac{1}{\rho}(m\, u_\theta - u_\rho)\right)^T.$$

□

We have an analogous result for also for the bottom part of the diagram (4.34):

Lemma 4.4. *The following diagram commutes:*

$$\begin{array}{ccccccc} Y_h^0 & \xrightarrow{\boldsymbol{G}} & Y_h^1 \times Y_h^0 & \xrightarrow{\boldsymbol{C}} & Y_h^{1*} \times Y_h^2 & \xrightarrow{D} & Y_h^2 \\ \downarrow{\scriptstyle \eta_{m,0}^{-1}} & & \downarrow{\scriptstyle \eta_{m,1}^{-1}} & & \downarrow{\scriptstyle \eta_{m,2}^{-1}} & & \downarrow{\scriptstyle \eta_{m,3}^{-1}} \\ Z_h^{m,0} & \xrightarrow{\mathbf{grad}^m} & Z_h^{m,1} & \xrightarrow{\mathbf{curl}^m} & Z_h^{m,2} & \xrightarrow{\mathrm{div}^m} & Z_h^{m,3} \end{array}$$

Proof. The proof is analogous to the one of Lemma 4.3. □

The next step is to prove that the middle part of the diagram (4.34), formed by the spaces in Cartesian coordinates and the corresponding projectors, commutes.

Lemma 4.5. *The following diagram commutes:*

$$\begin{array}{ccccccc} Y^0 & \xrightarrow{\boldsymbol{G}} & Y^1 \times Y^0 & \xrightarrow{\boldsymbol{C}} & Y^{1*} \times Y^2 & \xrightarrow{D} & Y^2 \\ \downarrow{\scriptstyle \Pi^0} & & \downarrow{\scriptstyle \Pi^1 \times \Pi^0} & & \downarrow{\scriptstyle \Pi^{1*} \times \Pi^2} & & \downarrow{\scriptstyle \Pi^2} \\ Y_h^0 & \xrightarrow{\boldsymbol{G}} & Y_h^1 \times Y_h^0 & \xrightarrow{\boldsymbol{C}} & Y_h^{1*} \times Y_h^2 & \xrightarrow{D} & Y_h^2 \end{array}$$

Proof. For the gradient and divergence part the result is an immediate consequence of the commutativity of the standard two-dimensional Cartesian diagrams (2.36). For the curl part, we need to show that $\mathbf{C} \circ (\boldsymbol{\Pi}^1 \times \Pi^0) = (\boldsymbol{\Pi}^{1*} \times \Pi^2) \circ \mathbf{C}$. For the rotor and the curl the result is immediate:

$$\begin{aligned} \mathbf{rot}\left(\Pi^0 \widetilde{u}_\theta\right) &= \boldsymbol{\Pi}^{1*}(\mathbf{rot}\, \widetilde{u}_\theta) \\ \mathrm{curl}\left(\boldsymbol{\Pi}^1 \widetilde{\boldsymbol{u}}_{\rho z}\right) &= \Pi^2(\mathrm{curl}\, \widetilde{\boldsymbol{u}}_{\rho z}) \ . \end{aligned} \tag{4.47}$$

Concerning the other components we have:

$$\mathbf{P}\boldsymbol{\Pi}^1(\widetilde{\boldsymbol{u}}_{\rho z}) = \boldsymbol{\Pi}^{1*}(\mathbf{P}\widetilde{\boldsymbol{u}}_{\rho z}) \tag{4.48}$$

since $Y^{1*} = \mathbf{P}Y^1$ and $Y_h^{1*} = \mathbf{P}Y_h^1$. □

Finally, Lemmas 4.3, 4.4 and 4.5 lead to the following result:

Theorem 4.1. *The following diagram commutes:*

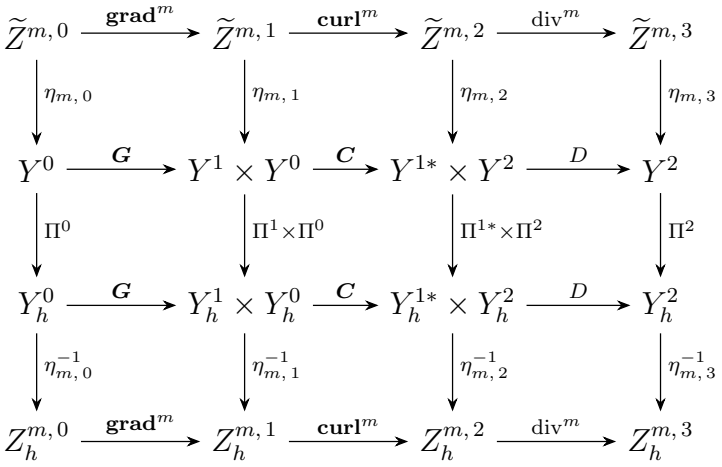

Proof. The proof is a direct consequence of Lemmas 4.3–4.5. For example, we have

$$\begin{aligned}
\breve{\Pi}^{m,2}(\mathbf{curl}^m \boldsymbol{u}) &= \left(\eta_{m,2}^{-1} \circ \left(\Pi^{1*} \times \Pi^2\right) \circ \eta_{m,2} \circ \mathbf{curl}^m\right)\boldsymbol{u} = \\
&= \left(\eta_{m,2}^{-1} \circ \left(\Pi^{1*} \times \Pi^2\right) \circ \mathbf{C} \circ \eta_{m,1}\right)\boldsymbol{u} = && \text{Lemma 4.3} \\
&= \left(\eta_{m,2}^{-1} \circ \mathbf{C} \circ \left(\Pi^1 \times \Pi^0\right) \circ \eta_{m,1}\right)\boldsymbol{u} = && \text{Lemma 4.5} \\
&= \left(\mathbf{curl}^m \circ \eta_{m,1}^{-1} \circ \left(\Pi^1 \times \Pi^0\right) \circ \eta_{m,1}\right)\boldsymbol{u} = && \text{Lemma 4.4} \\
&= \mathbf{curl}^m \left(\breve{\Pi}^{m,1}\boldsymbol{u}\right)
\end{aligned} \tag{4.49}$$

□

Another important property that can be deduced from the spaces in Cartesian coordinates is the exactness of the discrete sequence:

Theorem 4.2. *The discrete sequence*

$$0 \longrightarrow Z_h^{m,0} \xrightarrow{\mathbf{grad}^m} Z_h^{m,1} \xrightarrow{\mathbf{curl}^m} Z_h^{m,2} \xrightarrow{\mathrm{div}^m} Z_h^{m,3} \longrightarrow 0$$

is exact for $m \neq 0$.

Proof. If $u_h \in Z_h^{m,3}$, then $\widetilde{u}_h \in Y_h^2$. So the function

$$\boldsymbol{v}_h = \eta_{m,2}^{-1}\left(\left(\mathbf{0}^T, -\widetilde{u}_h\right)^T\right) \in Z_h^{m,2}$$

is such that $\mathrm{div}^m \boldsymbol{v}_h = u_h$. Similarly, if $\boldsymbol{u}_h \in Z_h^{m,2}$ is such that $\mathrm{div}^m \boldsymbol{u}_h = \mathbf{0}$, we have that

$$0 = \mathrm{div}^m \boldsymbol{u}_h = \mathrm{div}_\star^m \widetilde{\boldsymbol{u}}_h = \mathrm{div}\, \widetilde{\boldsymbol{u}}_{h,\rho z} - \widetilde{u}_{h,\theta}\ , \tag{4.50}$$

with $\widetilde{u}_{h,\theta} \in Y_h^2$. Choosing

$$\boldsymbol{v}_h = \eta_{m,1}^{-1}\left(\begin{bmatrix}\mathbf{P}\widetilde{\boldsymbol{u}}_{h,\rho z}\\ 0\end{bmatrix}\right) \in Z_h^{m,1} \tag{4.51}$$

we have that

$$\begin{aligned}\mathbf{curl}^m \boldsymbol{v}_h = \eta_{m,2}^{-1}(\boldsymbol{C}\widetilde{\boldsymbol{v}}_h) &= \eta_{m,2}^{-1}\left(\begin{bmatrix}-\mathbf{P}\mathbf{P}\widetilde{\boldsymbol{u}}_{h,\rho z}\\ -\operatorname{curl}(\mathbf{P}\widetilde{\boldsymbol{u}}_{h,\rho z})\end{bmatrix}\right)\\ &= \eta_{m,2}^{-1}\left(\begin{bmatrix}\widetilde{\boldsymbol{u}}_{h,\rho z}\\ \operatorname{div}\widetilde{\boldsymbol{u}}_{h,\rho z}\end{bmatrix}\right) = \eta_{m,2}^{-1}\left(\begin{bmatrix}\widetilde{\boldsymbol{u}}_{h,\rho z}\\ \widetilde{u}_{h,\theta}\end{bmatrix}\right) = \boldsymbol{u}_h\ .\end{aligned}$$

If $\boldsymbol{u}_h \in Z_h^{m,1}$ is such that $\mathbf{curl}^m \boldsymbol{u}_h = \mathbf{0}$, we have that $\mathbf{curl}_\star^m \widetilde{\boldsymbol{u}}_h = \mathbf{0}$ and so that (see (4.42)) $-\mathbf{P}\widetilde{\boldsymbol{u}}_{h,\rho z} = \mathbf{rot}\,\widetilde{u}_{h,\theta} = \mathbf{P}\,\mathbf{grad}\,\widetilde{u}_{h,\theta}$. These previous relations imply that the third component is identically null. Moreover, we can also see that $\widetilde{\boldsymbol{u}}_{h,\rho z} = -\,\mathbf{grad}\,\widetilde{u}_{h,\theta}$ so, choosing $v_h = \eta_{m,0}^{-1}(-\widetilde{u}_{h,\theta})$ we have that $\mathbf{grad}^m v_h = \boldsymbol{u}_h$. Finally, we see that the equation corresponding to the third component in $\mathbf{grad}^m u_h = \mathbf{0}$ implies that $u_h \equiv 0$. □

In order to prove error estimates, let us define the following spaces:

$$\begin{aligned}H_\rho^s(\widetilde{\mathbf{grad}}^m) &= \left\{u \in H(\mathbf{grad}^m) :\ \eta_{m,0}(u) \in H_\rho^s,\ \widetilde{\mathbf{grad}}^m u \in H_\rho^s\right\},\\ H_\rho^s(\widetilde{\mathbf{curl}}^m) &= \left\{\boldsymbol{u} \in H(\mathbf{curl}^m) :\ \eta_{m,1}(\boldsymbol{u}) \in H_\rho^s,\ \widetilde{\mathbf{curl}}^m \boldsymbol{u} \in H_\rho^s\right\},\\ H_\rho^s(\widetilde{\operatorname{div}}^m) &= \left\{\boldsymbol{u} \in H(\operatorname{div}^m) :\ \eta_{m,2}(\boldsymbol{u}) \in H_\rho^s,\ \widetilde{\operatorname{div}}^m \boldsymbol{u} \in H_\rho^s\right\}\ ,\end{aligned} \tag{4.52}$$

where

$$\begin{aligned}\widetilde{\mathbf{grad}}^m u &= \eta_{m,1}(\mathbf{grad}^m u)\\ \widetilde{\mathbf{curl}}^m \boldsymbol{u} &= \eta_{m,2}(\mathbf{curl}^m \boldsymbol{u})\\ \widetilde{\operatorname{div}}^m \boldsymbol{u} &= \eta_{m,3}(\operatorname{div}^m \boldsymbol{u}).\end{aligned} \tag{4.53}$$

The proof of the following estimates is analogous to that of [Oh15, Theorem 4.1]:

Lemma 4.6. *For $s \geq 0$, we have the error estimates:*

$$\left\| u - \breve{\Pi}^{m,0} u \right\|_{H(\mathbf{grad}^m)} \leq C h^s \Big(\|\eta_{m,0}(u)\|_{H^{2+s}_\rho} + \|\eta_{m,1}(\mathbf{grad}^m u)\|_{H^{2+s}_\rho} \Big), \quad u \in H^{s+2}_\rho(\widetilde{\mathbf{grad}}^m), \tag{4.54}$$

$$\left\| \boldsymbol{u} - \breve{\Pi}^{m,1} \boldsymbol{u} \right\|_{H(\mathbf{curl}^m)} \leq C h^s \Big(\|\eta_{m,1}(\boldsymbol{u})\|_{H^{2+s}_\rho} + \|\eta_{m,2}(\mathbf{curl}^m \boldsymbol{u})\|_{H^{2+s}_\rho} \Big), \quad \boldsymbol{u} \in H^{s+2}_\rho(\widetilde{\mathbf{curl}}^m), \tag{4.55}$$

$$\left\| \boldsymbol{u} - \breve{\Pi}^{m,2} \boldsymbol{u} \right\|_{\boldsymbol{H}(\mathrm{div}^m)} \leq C h^s \Big(\|\eta_{m,2}(\boldsymbol{u})\|_{H^{2+s}_\rho} + \|\eta_{m,3}(\mathrm{div}^m \boldsymbol{u})\|_{H^{2+s}_\rho} \Big), \quad \boldsymbol{u} \in H^{s+2}_\rho(\widetilde{\mathrm{div}}^m), \tag{4.56}$$

$$\left\| u - \breve{\Pi}^{m,3} u \right\|_{L^2_\rho} \leq C h^s \|u\|_{H^{2+s}_\rho} \qquad u \in H^{s+2}_\rho. \tag{4.57}$$

Proof. Since the domain is bounded we have that $0 < \rho < R$. Moreover, we have the continuous embedding $H^{s+2}_\rho \hookrightarrow H^s$ [MR82] and so, for $s \geq 2$ we have that $H^s_\rho(\widetilde{\mathbf{grad}}^m) \subset \widetilde{Z}^{m,0}$, $H^s_\rho(\widetilde{\mathbf{curl}}^m) \subset \widetilde{Z}^{m,1}$, $H^s_\rho(\widetilde{\mathrm{div}}^m) \subset \widetilde{Z}^{m,2}$ and $H^s_\rho \subset \widetilde{Z}^{m,3}$. The procedure to derive the estimates is analogous for all the cases and can be summarized as follows, for $k = 1, 2, 3$:

$$\begin{aligned}
\left\| u - \breve{\Pi}^k u \right\|_\rho &= \left\| u - \big(\eta^{-1}_{m,k} \circ \Pi^k \circ \eta_{m,k}\big) u \right\|_\rho \\
&= \left\| \big(\eta^{-1}_{m,k} \circ \eta_{m,k}\big) u - \big(\eta^{-1}_{m,k} \circ \Pi^k \circ \eta_{m,k}\big) u \right\|_\rho \\
&= \left\| \eta^{-1}_{m,k} \big(\eta_{m,k}(u) - \Pi^k(\eta_{m,k}(u))\big) \right\|_\rho \\
&\leq C \left\| \eta^{-1}_{m,k} \big(\eta_{m,k}(u) - \Pi^k(\eta_{m,k}(u))\big) \right\| \\
&\leq C \left\| \eta_{m,k}(u) - \Pi^k(\eta_{m,k}(u)) \right\| \\
&\leq C\, h^s \left\| \eta_{m,k}(u) \right\|_{H^s} \\
&\leq C\, h^s \left\| \eta_{m,k}(u) \right\|_{H^{s+2}_\rho} ,
\end{aligned}$$

where the constant C is different for each inequality, but is independent on u and can depend on h only through the ratio between the biggest and the smallest element h_{max}/h_{min}. The estimates for the terms involving the differential operators are reduced to the previous ones exploiting the com-

mutativity of the projectors. Consider $u \in H^{s+2}_\rho$, we have that

$$\left\|u - \breve{\Pi}^{m,3} u\right\|_\rho \leq \left\|\sqrt{\frac{R}{\rho}}\left(u - \Pi^2 u\right)\right\|_\rho = \sqrt{R}\left\|u - \Pi^2 u\right\| \\ \leq \sqrt{R}\, C\, h^s \left\|u\right\|_{H^s} \leq \widetilde{C} h^s \left\|u\right\|_{H^{s+2}_\rho} \quad .$$

This proves (4.57). Considering a function $u \in H^{s+2}_\rho(\widetilde{\mathbf{grad}}^m)$, then

$$\left\|u - \breve{\Pi}^{m,0} u\right\|_\rho = \left\|u - \frac{\rho}{m}\Pi^0\left(\frac{m}{\rho}u\right)\right\|_\rho \\ = \left\|\frac{\rho}{m}\left(\frac{m}{\rho}u\right) - \Pi^0\left(\frac{m}{\rho}u\right)\right\|_\rho \\ \leq R\left\|\frac{m}{\rho}u - \Pi^0\left(\frac{m}{\rho}u\right)\right\|_\rho \leq Ch^s\left\|\frac{m}{\rho}u\right\|_{H^{s+2}_\rho} .$$

So, we have that

$$\left\|u - \breve{\Pi}^{m,0} u\right\|_\rho \leq Ch^s\left\|\frac{m}{\rho}u\right\|_{H^{s+2}_\rho} = Ch^s\left\|\eta_{m,0}(u)\right\|_{H^{s+2}_\rho} \quad . \tag{4.58}$$

Consider now a function $\boldsymbol{u} \in H^{s+2}_\rho(\widetilde{\mathrm{div}}^m)$, the estimate (4.56) involves the norm

$$\left\|\boldsymbol{u}\right\|^2_{H_\rho(\mathrm{div}^m)} = \left\|\boldsymbol{u}\right\|^2_{L^2_\rho} + \left\|\mathrm{div}^m \boldsymbol{u}\right\|^2_{L^2_\rho} . \tag{4.59}$$

For the first term we have that

$$\left\|\boldsymbol{u} - \breve{\Pi}^{m,2}\boldsymbol{u}\right\|^2_\rho = \left\|\boldsymbol{u}_{\rho z} - \Pi^{1*}\boldsymbol{u}_{\rho z}\right\|^2_\rho \\ + \left\|u_\theta - \frac{\rho}{m}\Pi^2\left(\frac{m\,u_\theta - u_\rho}{\rho}\right) - \frac{1}{m}\left[\Pi^{1*}\boldsymbol{u}_{\rho z}\right]_\rho\right\|^2_\rho .$$

Adding and subtracting $\frac{u_\rho}{m}$ in the second term we obtain

$$\left\|\boldsymbol{u} - \breve{\Pi}^{m,2}\boldsymbol{u}\right\|^2_\rho \leq \left\|\boldsymbol{u}_{\rho z} - \Pi^{1*}\boldsymbol{u}_{\rho z}\right\|^2_\rho \\ + 2\left\|\frac{\rho}{m}\left(\frac{m\,u_\theta - u_\rho}{\rho} - \Pi^2\left(\frac{m\,u_\theta - u_\rho}{\rho}\right)\right)\right\|^2_\rho \\ + 2\left\|\frac{1}{m}\left(u_\rho - \left[\Pi^{1*}\boldsymbol{u}_{\rho z}\right]_\rho\right)\right\|^2_\rho \\ \leq 3\left\|\boldsymbol{u}_{\rho z} - \Pi^{1*}\boldsymbol{u}_{\rho z}\right\|^2_\rho + R^2\left\|\left(\widetilde{u}_\theta - \Pi^2\widetilde{u}_\theta\right)\right\|^2_\rho \\ \leq Ch^{2s}\left(\left\|\boldsymbol{u}\right\|^2_{H^{s+2}_\rho} + \left\|\widetilde{u}\right\|^2_{H^{s+2}_\rho}\right) = Ch^{2s}\left\|\eta_{m,2}(\boldsymbol{u})\right\|^2_{H^{s+2}_\rho} .$$

So, we have that

$$\left\|\boldsymbol{u}-\breve{\Pi}^{m,2}\boldsymbol{u}\right\|_{L^2_\rho}\leq Ch^s\left\|\eta_{m,2}(\boldsymbol{u})\right\|_{H^{s+2}_\rho}. \tag{4.60}$$

The estimate for $\|\mathrm{div}^m\,\boldsymbol{u}\|^2_\rho$ follows from the commutativity property of the projectors and (4.57):

$$\left\|\mathrm{div}^m\left(\boldsymbol{u}-\breve{\Pi}^{m,2}\boldsymbol{u}\right)\right\|_\rho=\left\|\mathrm{div}^m\,\boldsymbol{u}-\breve{\Pi}^{m,3}(\mathrm{div}^m\,\boldsymbol{u})\right\|_\rho\leq Ch^s\left\|\mathrm{div}^m\,\boldsymbol{u}\right\|_{H^{s+2}_\rho}.$$

This concludes the proof of (4.56). The estimate (4.55) is proven analogously, considering the norm:

$$\|\boldsymbol{u}\|^2_{H_\rho(\mathbf{curl}^m)}=\|\boldsymbol{u}\|^2_{L^2_\rho}+\|\mathbf{curl}^m\,\boldsymbol{u}\|^2_{L^2_\rho}. \tag{4.61}$$

For the first term we have that

$$\begin{aligned}\left\|\boldsymbol{u}-\breve{\Pi}^{m,1}\boldsymbol{u}\right\|^2_\rho&=\left\|u_\theta-\Pi^0u_\theta\right\|^2_\rho\\&\quad+\left\|\boldsymbol{u}_{\rho z}-\frac{\rho}{m}\Pi^1(\widetilde{\boldsymbol{u}}_{\rho z})-\frac{1}{m}\begin{bmatrix}\Pi^0u_\theta\\0\end{bmatrix}\right\|^2_\rho.\end{aligned}$$

Adding and subtracting $\left(\frac{u_\theta}{m},\,0\right)^T$ in the second term we obtain

$$\begin{aligned}\left\|\boldsymbol{u}-\breve{\Pi}^{m,1}\boldsymbol{u}\right\|^2_\rho&\leq\left\|u_\theta-\Pi^0u\theta\right\|^2_\rho\\&\quad+2\left\|\frac{\rho}{m}\left(\widetilde{\boldsymbol{u}}_{\rho z}-\Pi^1(\widetilde{\boldsymbol{u}}_{\rho z})\right)\right\|^2_\rho+2\left\|u_\theta-\Pi^0u_\theta\right\|^2_\rho\\&\leq Ch^{2s}\left(\|u_\theta\|^2_{H^{s+2}_\rho}+\|\widetilde{\boldsymbol{u}}_{\rho z}\|^2_{H^{s+2}_\rho}\right)=Ch^{2s}\left\|\eta_{m,1}(\boldsymbol{u})\right\|^2_{H^{s+2}_\rho}.\end{aligned}$$

So we have that

$$\left\|\boldsymbol{u}-\breve{\Pi}^{m,1}\boldsymbol{u}\right\|_{L^2_\rho}\leq Ch^s\left\|\eta_{m,1}(\boldsymbol{u})\right\|_{H^{s+2}_\rho}. \tag{4.62}$$

The estimate for $\|\mathbf{curl}^m\,\boldsymbol{u}\|^2_\rho$ follows from the commutativity property of the projectors and (4.60):

$$\begin{aligned}\left\|\mathbf{curl}^m\left(\boldsymbol{u}-\breve{\Pi}^{m,1}\boldsymbol{u}\right)\right\|_\rho&=\left\|\mathbf{curl}^m\,\boldsymbol{u}-\breve{\Pi}^{m,2}(\mathbf{curl}^m\,\boldsymbol{u})\right\|_\rho\\&\leq Ch^s\left\|\eta_{m,2}(\mathbf{curl}^m\,\boldsymbol{u})\right\|_{H^{s+2}_\rho}.\end{aligned}$$

This concludes the proof of (4.56). Consider then a function $u \in H^{s+2}_{\rho}(\widetilde{\mathbf{grad}}^{\,m})$. The norm involved in (4.54) is

$$\|u\|^2_{H_\rho(\mathbf{grad}^m)} = \|u\|^2_{L^2_\rho} + \|\mathbf{grad}^m u\|^2_{L^2_\rho} . \tag{4.63}$$

For the first term, we already have the estimate given by (4.58). The estimate for the second term follows from the commutativity property of the projectors and (4.60):

$$\begin{aligned}\left\|\mathbf{grad}^m \left(u - \breve{\Pi}^{m,0} u\right)\right\|_\rho &= \left\|\mathbf{grad}^m u - \breve{\Pi}^{m,1}(\mathbf{grad}^m u)\right\|_\rho \\ &\leq C h^s \left\|\eta_{m,1}(\mathbf{grad}^m u)\right\|_{H^{s+2}_\rho} .\end{aligned}$$

This concludes the proof of (4.54). □

We want now to show that the finite-dimensional spaces approximate the continuous ones (2.50). To this end we use the fact that $\mathcal{D}_{\Gamma_0}(\overline{S})$, the space of smooth functions which vanish on the axis Γ_0, is dense in $Z^{m,k}$ [Lac00, Proposition 2], [Nke05, Lemma 2.3].

Lemma 4.7. *We have that*

$$\lim_{h\to 0} \inf_{v_h \in Z^{m,k}_h} \|v - v_h\|_{Z^{m,k}} = 0 \ , v \in Z^{m,k} \ , \quad k = 0, \ldots, 3 \tag{4.64}$$

Proof. For $\varepsilon > 0$, thanks to the density of $\mathcal{D}_{\Gamma_0}(\overline{S})$ in $Z^{m,k}$, we can choose a function $\widetilde{v} \in \mathcal{D}_{\Gamma_0}(\overline{S})$ such that $\|v - \widetilde{v}\|_{Z^{m,k}} \leq \varepsilon/2$. Since $\mathcal{D}_{\Gamma_0}(\overline{S}) \subset \widetilde{Z}^{m,k}$, we can use the estimates (4.54)-(4.57) and choose an $\widetilde{h}$, so that $\left\|\widetilde{v} - v_{\widetilde{h}}\right\|_{Z^{m,k}} \leq \varepsilon/2$ and then, the triangular inequality gives the result:

$$\left\|v - v_{\widetilde{h}}\right\|_{Z^{m,k}} \leq \varepsilon \ . \tag{4.65}$$

□

Since $\widetilde{Z}^{m,k} \subset Z^{m,k}$, the spaces $Z^{m,k}_h$ form a conforming discretization and Lemma 4.4 allows to deduce the subcomplex property. Moreover, in Theorem 4.2 it was proven that the discrete sequence is exact, as the continuous one (2.50). Thanks to the subcomplex property it is possible to obtain an inf-sup condition (4.3), where the constant γ_h might tend to 0 for $h \to 0$, leading to an unstable method. In the presence of a bounded cochain projector, as in the case of the spaces in Cartesian coordinates presented in Section 4.1.1, it is possible to give a lower bound for γ_h and to deduce the stability of the method [AFW10, Theorem 5.4]. Here, we limit ourselves to an empirical verification of the discrete inf-sup condition using the method

proposed in [CB93] for the bilinear form associated to the Problem 2.10, which amounts to estimating the constant γ_h and observing its behaviour for $h \to 0$. For this empirical verification we consider the material parameter ϵ and μ to be equal to one and the geometry of the cross-section as depicted in Figure 4.5. The kink on the axis is parametrized through the angle α, *i.e.*

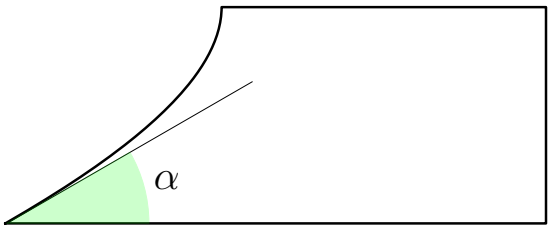

Figure 4.5: Family of geometries parametrized with respect to α, equal to 30° in this case.

the smaller the angle the sharper the resulting kink. Let us now consider the discrete spaces for a specific value of $m \neq 0$ with the corresponding basis functions

$$\text{span}\left(\{b_i\}_{i=1}^{N_0}\right) = Z_h^{m,0} \subset Z^{m,0} = H_\rho(\mathbf{grad}^m) \,, \tag{4.66}$$

$$\text{span}\left(\{\boldsymbol{c}_i\}_{i=1}^{N_1}\right) = Z_h^{m,1} \subset Z^{m,1} = H_\rho(\mathbf{curl}^m) \,, \tag{4.67}$$

where N_0 and N_1 indicate the dimension of the corresponding finite-dimensional space and we note that, even if it is not explicit in the notation, the basis functions are different for each value of m. The matrices arising from the discretization of Problem 2.10 are

$$[\mathbf{A}_m]_{i,\,j} = \int (\mathbf{curl}^m \boldsymbol{c}_j) \cdot (\mathbf{curl}^m \boldsymbol{c}_i)\, \rho \mathrm{d}\rho \mathrm{d}z \,,$$

$$[\mathbf{B}_m]_{i,\,j} = \int (\mathbf{grad}^m b_j) \cdot \boldsymbol{c}_i\, \rho \mathrm{d}\rho \mathrm{d}z \,,$$

$$[\mathbf{C}_m]_{i,\,j} = \int (\mathbf{grad}^m b_j) \cdot (\mathbf{grad}^m b_i)\, \rho \mathrm{d}\rho \mathrm{d}z \,.$$

It is then possible to estimate the discrete inf-sup constant γ_h as the square root of the first non-zero eigenvalue of the following problem [CB93, Proposition 2.2]:

$$\mathbf{H}_m \mathbf{q}_i = \lambda_i \mathbf{C}_m \mathbf{q}_i \,, \tag{4.68}$$

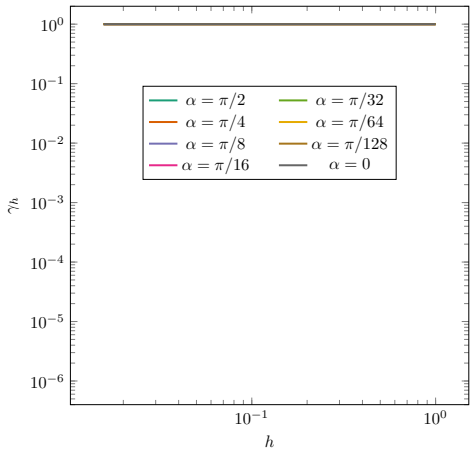

Figure 4.6: Estimations of the inf-sup constant γ_h for $m = -3$ and for $p = 3$. The lines appear all as superposed for all the values of the angle α. In the worst case, the difference $1 - \gamma_h$ is of the order of 1×10^{-4}.

where $\mathbf{H}_m = \mathbf{B}_m^T \mathbf{A}_m^{-1} \mathbf{B}_m$. In Figure 4.6, the results are reported for $m = -3$, $p = 3$ and different values of the geometry parametrization α. It can be noticed that the values remain close to 1 for the different values of refinement and for the different geometries.

An interesting future development is to obtain bounded cochain projectors onto $\widetilde{Z}^{m,k}$, for example through smoothing arguments, defined directly on $Z^{m,k}$. This would allow to directly obtain the stability results and the nice approximation properties applying the general theory of Arnold and Falk [Arn18].

4.2 The Laplace problem on a cylinder

In the previous section, we presented a method to solve different problems in electromagnetism with rather weak assumptions regarding the material parameters and the domains. In this section, we consider instead two specific numerical methods used to solve the Laplace problem on a cylinder using cylindrical coordinates. The range of applicability of the methods that we will present it is therefore smaller. Nevertheless, we consider this case because specific methods can be employed and it has a significant practical relevance in the context of particle accelerators, when we consider the vacuum region inside the magnets where the particles travel. This type of application will be discussed in Section 5.1. We consider a cylinder $\breve{\Omega}$ of radius R and length L and a Laplace problem where we set Neumann boundary data g on the

lateral surface Σ_N, but we postpone the choice of the boundary conditions on the bases Σ_D. In cylindrical coordinates the problem reads

$$\begin{aligned} -\Delta^c \psi = -\frac{1}{\rho}\partial_\rho(\rho\,\partial_\rho\psi) - \frac{1}{\rho^2}\partial_{\theta\theta}\psi - \partial_{zz}\psi = 0\,, \quad & \text{in } \Omega\,, \\ \partial_{\boldsymbol{\nu}}\psi = g\,, & \text{on } \Gamma_N\,. \end{aligned} \tag{4.69}$$

Employing the complex Fourier basis $\{e^{im\theta}\}$ to represent the angular dependence of the solution, we have that each Fourier coefficient has to satisfy

$$\begin{aligned} -\frac{1}{\rho}\partial_\rho(\rho\,\partial_\rho\psi^{(m)}) + \frac{m^2}{\rho^2}\psi^{(m)} + -\partial_{zz}\psi^{(m)} = 0\,, \quad & \text{in } \Omega\,, \\ \partial_{\boldsymbol{\nu}}\psi^{(m)} = g^{(m)}\,, & \text{on } \Gamma_N\,, \end{aligned} \tag{4.70}$$

where $S = (0,\, R) \times (0,\, L)$, $\Gamma_N = \{R\} \times (0,\, L)$ and $\Gamma_D = (0,\, L) \times \{0,\, L\}$. This is the starting point for both the methods that we will discuss. The first method, which we will call Bessel Fourier Fourier (BFF), is based on the classical method of separation of variables with the use of eigenfunctions for the Laplace operator in cylindrical coordinates with the assumption of periodic boundary conditions the longitudinal coordinate z [Jac07, Section 3.7-3.8]. A further approximation, based on the series representation for the Bessel functions, is then used [Dra97, Section 15.3]. The second one, which we will call Lobatto B-spline Fourier (LBF), is similar to the one presented in the previous sections and relies on the Galerkin formulation. We propose the use of discrete spaces built by means of a tensor product of Lobatto polynomials and univariate B-splines.The reason behind this choice is due to the need of describing fields that have a complicate behaviour along the longitudinal variable z, where we will use B-splines, while exploiting the good approximation properties of Lobatto polynomials in the radial direction, where we expect a very smooth field.

4.2.1 Bessel Fourier Fourier and generalized gradients

This method only applies to the case of periodic boundary conditions also for the z coordinates, which amounts to imposing on Σ_D the condition $\psi|_{z=0} = \psi|_{z=L}$. We then employ the Fourier basis to describe the z dependence of the solution:

$$\psi^{(m)}(\rho,\, z) = \sum_{k\in\mathbb{Z}} \psi^{(m,\,k)}(\rho)\, e^{i\frac{2\pi}{L}kz}\,. \tag{4.71}$$

Using this assumption, and setting $\omega_k = \frac{2\pi}{L}|k|$, problem (4.70) yields

$$\begin{aligned} -\frac{1}{\rho}\partial_\rho(\rho\,\partial_\rho\psi^{(m,k)}) + \left(\frac{m^2}{\rho^2} + \omega_k^2\right)\psi^{(m,k)} &= 0\,, \quad \text{in } (0,\,R)\,, \\ \partial_{\boldsymbol{\nu}}\psi^{(m,k)} &= g^{(m,k)}\,, \qquad\qquad \text{on } \{R\}\,. \end{aligned} \tag{4.72}$$

We have now a set of one-dimensional problems, one for each value of m and k, in which we have to find the solution $\psi^{(m,k)}(\rho)$. This is achieved by choosing proper functions that identically satisfy the first equation in (4.72) and match the boundary conditions at $\rho = R$. For $k = 0$, we have that $\omega_k = 0$ and any of the following functions identically satisfies the Laplace equation:

$$\begin{aligned} &\alpha_1\,\log\rho\,, \quad \alpha_2\,, \qquad m = 0 \\ &\alpha_3\,\rho^{|m|}\,, \;\; \alpha_4\,\rho^{-|m|}\,, \quad m \neq 0\,, \end{aligned} \tag{4.73}$$

where $\alpha_1,\, \alpha_2,\, \alpha_3,\, \alpha_4 \;\in\; \mathbb{R}$. Excluding the functions that are not bounded for $\rho = 0$, we set $\alpha_1 = \alpha_4 = 0$. With an abuse of notation we will denote with the same symbol the multiplicative coefficient and the function of ρ that identically satisfies the Laplace equation for the specific m, k pair, so that

$$\psi^{(0,0)}(\rho) = \psi^{(0,0)} \quad \text{and} \quad \psi^{(m,0)}(\rho) = \psi^{(m,0)}\,\rho^{|m|} \tag{4.74}$$

identically satisfy problem (4.72) for $k = 0$. For $k \neq 0$, we have that $\omega_k > 0$ and, with the change of variables $\widetilde{\rho} = \omega_k\rho$, we can rewrite the Laplace equation in (4.72) as:

$$-\frac{1}{\widetilde{\rho}}\partial_{\widetilde{\rho}}\big(\rho\,\partial_{\widetilde{\rho}}\psi^{(m,k)}\big) + \left(\frac{m^2}{\widetilde{\rho}^2} + 1\right)\psi^{(m,k)} = 0\,. \tag{4.75}$$

This is the modified Bessel equation [Nis, Equation 10.25.1], whose solutions are proportional to the modified Bessel functions of the first $I_{|m|}(\omega_k\,\rho)$ and second kind $K_{|m|}(\omega_k\,\rho)$ [Nis, Equation 10.25.2-3]. This latter solution is discarded since it is not bounded for $\rho = 0$ and, analogously to the case $k = 0$, we can set $\psi^{(m,k)}(\rho) = \psi^{(m,k)}\,I_{|m|}(\omega_k\,\rho)$. Therefore, a function in the form

$$\begin{aligned} \psi(\rho,\,z,\,\theta) = &\sum_{m\in\mathbb{Z}} \psi^{(m,0)}\rho^{|m|}\,e^{im\theta} \\ &+ \sum_{m\in\mathbb{Z}}\sum_{k\neq 0} \psi^{(m,k)} I_{|m|}(\omega_k\rho)\,e^{i\omega_k z}\,e^{im\theta} \end{aligned} \tag{4.76}$$

is a solution of the Laplace equations and the coefficients $\psi^{(m,k)}$ can be chosen to match the boundary conditions in (4.72):

$$\begin{aligned}\psi^{(m,0)} &= \frac{1}{|m|R^{|m|-1}}\, g^{(m,0)}\,,\\ \psi^{(m,k)} &= \frac{1}{\omega_k I'_{|m|}(\omega_k R)}\, g^{(m,k)}\,, \quad k \neq 0\,.\end{aligned} \tag{4.77}$$

The coefficient $\psi^{(0,0)}$ remains undefined and can be chosen arbitrarily, while $g^{(0,0)}$ must satisfy a compatibility condition and be equal to 0. This method is classical, and further details can be found, for example in [Jac07, Section 3.7, 3.8]. The discretization step amounts here to choosing a finite number of Fourier modes m and k.

Vector potential computation

We will now consider the case $m \neq 0$ and show a useful property of the method presented: defining the following azimuthal-free function (*i.e.* $A_\theta \equiv 0$):

$$\begin{aligned}A_\rho &= \sum_{m\neq 0} A_\rho^{(m)}\, e^{im\,\theta} = \sum_{m\neq 0} \frac{i}{m}\rho\,\partial_z\psi^{(m)}\, e^{im\,\theta}\,,\\ A_z &= \sum_{m\neq 0} A_z^{(m)}\, e^{im\,\theta} = \sum_{m\neq 0} -\frac{i}{m}\rho\partial_\rho\psi^{(m)}\, e^{im\,\theta}\,,\\ A_\theta &= 0\,.\end{aligned} \tag{4.78}$$

we have that $\mathbf{grad}^c\,\psi = \mathbf{curl}^c\,\boldsymbol{A}$. In fact, for the ρ component, we have:

$$\left(\frac{im}{\rho}A_z^{(m)} - \partial_z A_\theta^{(m)}\right) = -\frac{im}{\rho}\frac{i}{m}\rho\partial_\rho\psi^{(m)} = \partial_\rho\psi^{(m)}\,. \tag{4.79}$$

For the z component we have:

$$\left(\frac{1}{\rho}\partial_\rho(\rho A_\theta^{(m)}) - \frac{im}{\rho}A_\rho^{(m)}\right) = -\frac{im}{\rho}\frac{i}{m}\rho\partial_z\psi^{(m)} = \partial_z\psi^{(m)}\,. \tag{4.80}$$

Finally, for the θ component we have:

$$\begin{aligned}\left(\partial_z A_\rho^{(m)} - \partial_\rho A_z^{(m)}\right) = \frac{i}{m}\rho\sum_{k\neq 0} -\omega_k^2 I_m(\omega_k\rho)\,\psi^{(m,k)}\, e^{i\omega_k z}\\ + \frac{i}{m}\sum_{k\neq 0}\partial_\rho(\rho\partial_\rho I_m(\omega_k\rho))\,\psi^{(m,k)}\, e^{i\omega_k z}\\ + im\rho^{|m|-1}\psi^{(m,0)}\,.\end{aligned} \tag{4.81}$$

Thanks to the property of the modified Bessel function of the first kind, we have that the terms in the series can be simplified:

$$\begin{aligned}\left(\partial_z A_\rho^{(m)} - \partial_\rho A_z^{(m)}\right) &= \frac{i}{m}\rho \sum_{k\neq 0} \frac{m^2}{\rho^2} I_m(\omega_k \rho)\, \psi^{(m,k)}\, e^{i\omega_k z} \\ &+ im\rho^{|m|-1}\psi^{(m,0)} = \frac{im}{\rho}\psi^{(m)}\,.\end{aligned} \tag{4.82}$$

We have in this way showed a simple procedure to compute the magnetic vector potential $\boldsymbol{A}$ in the so called Azimuthal-Free (AF) gauge.
We now present a further approximation step used in accelerator physics and based on the approximation of the Bessel functions via its series expansion [Dra97, Section 15.3]. We start writing each $\psi^{(m)}(\rho,\, z)$, $m \neq 0$ using the Fourier coefficients computed from the data (4.77):

$$\psi^{(m)}(\rho,\, z) = \sum_{k\in\mathbb{Z}} \frac{g^{(m,k)}}{\omega_k I'_{|m|}(\omega_k R)} I_{|m|}(\omega_k \rho) e^{i\omega_k z}\,, \tag{4.83}$$

where the value for $k = 0$ corresponds to

$$\frac{g^{(m,0)}}{|m| R^{|m|-1}} \rho^{|m|} \tag{4.84}$$

and is obtained considering the limit for $k \to 0$, which can be computed considering the representation of the modified Bessel function of the first kind using series [Nis, Eq. 10.25.2]:

$$I_{|m|}(x) = \left(\frac{x}{2}\right)^{|m|} \sum_{\ell=0}^{\infty} \frac{x^{2\ell}}{2^{2\ell}\ell!\,(|m|+\ell)!}\,. \tag{4.85}$$

and the recurrence relation

$$I'_{|m|}(x) = \frac{I_{|m|-1}(x) + I_{|m|+1}(x)}{2}\,. \tag{4.86}$$

Generalized gradients

Substituting the series representation (4.85) in (4.83), we can obtain the following:

$$\psi^{(m)}(\rho,\, z) = \sum_{\ell=0}^{\infty} \frac{(-1)^\ell |m|!}{4^\ell \ell! (|m|+\ell)!}\, C_m^{[2\ell]}(z) \rho^{2\ell+|m|}\,, \tag{4.87}$$

where the functions $C_m^{[2\ell]}(z)$ are called generalized gradients and defined as follows:

$$C_m^{[2\ell]}(z) = \sum_{k\in\mathbb{Z}} \frac{(-1)^\ell}{2^{|m|}|m|!} \frac{\omega_k^{2\ell+|m|-1}}{I'_m(\omega_k R)} g^{(m,\,k)}\, e^{i\omega_k z}\,. \tag{4.88}$$

Note that the subscript m in the generalized gradients notation indicates the mode number which was typically placed as superscript, *e.g.* $\psi^{(m)}$. Moreover, we note that $C_m^{[n]}(z)$ can be seen as the n-th derivative with respect to z of the function $C_m^{[0]}(z)$:

$$C_m^{[n]}(z) = \frac{\partial^n}{\partial z^n} C_m^{[0]}(z)\,. \tag{4.89}$$

To conclude, we have that the solution of the Laplace problem, for $m \neq 0$, can be expressed as:

$$\psi(\rho,\, z,\, \theta) = \sum_{m\neq 0} \sum_{\ell=0}^{\infty} \frac{(-1)^\ell |m|!}{4^\ell \ell!(|m|+\ell)!}\, \rho^{2\ell+|m|}\, C_m^{[2\ell]}(z)\, e^{im\theta}\,, \tag{4.90}$$

where the boundary data are contained in the generalized gradients. The solution can also be expressed in terms of sine and cosine series using the generalized gradients $C_{m,\,c}^{[2\ell]}(z)$ and $C_{m,\,s}^{[2\ell]}(z)$ associated, respectively, to the cosine and sine terms. These can be obtained from $C_m^{[2\ell]}(z)$ simply using (2.47). In practice, for the solution in the form (4.90), the number of terms in the series involving the generalized gradients constitutes another discretization parameter. In view of (4.89), this is often set in terms of number of generalized gradients derivatives, *i.e.* $2\ell \leq ND$.

Horizontal-free Coulomb gauge

It is possible to use the relations (4.78) to obtain the vector potential expressed in terms of generalized gradients. We recall the fact that a vector potential is defined up to gradients of scalar functions. Consider $\boldsymbol{A}' = \boldsymbol{A} + \mathbf{grad}^c\,\lambda$, where λ, is a scalar function, we have that

$$\boldsymbol{B} = \mathbf{curl}^c\,(\boldsymbol{A}) = \mathbf{curl}^c\,(\boldsymbol{A} + \mathbf{grad}^c\,\lambda) = \mathbf{curl}\,(\boldsymbol{A}')$$

since $\mathbf{curl}^c\,\mathbf{grad}^c\,\lambda = 0$. If $\boldsymbol{A}$ is in a Coulomb gauge (2.19), requiring that $\boldsymbol{A}'$ is in the same gauge amounts to requiring that λ is harmonic, in fact

$$0 = \mathrm{div}^c\,\boldsymbol{A}' = \mathrm{div}^c\,(\boldsymbol{A} + \mathbf{grad}^c\,\lambda) = \Delta^c\,\lambda\,. \tag{4.91}$$

Thanks to the properties of the modified Bessel functions, given a set of generalized gradients, we know that (4.90) satisfies the Laplace equation. It is

therefore possible to choose a suitable set of generalized gradients to produce a function λ, in the form (4.90), which is harmonic and thus induces, through its gradient, a gauge transformation for a given vector potential $\boldsymbol{A}$. Moreover, the resulting vector potential $\boldsymbol{A}'$ will still be in a Coulomb gauge if the original one $\boldsymbol{A}$ was. This procedure can be exploited to speed up the computation of particle trajectories, presented in Chapter 3. In fact, considering the Hamiltonian (3.21), we have that a vector potential for which its horizontal component vanishes, *i.e.* $A_x \equiv 0$, will reduce the amounts of computation needed and thus will increase the speed of the computation [Sim+19a]. In Section 5.1, we will compute the particle trajectories in a magnetostatic field and we will see how type of gauge, called Horizontal-Free Coulomb (HFC), can be used to improve the efficiency of the method. The strategy to compute this gauge is presented [Dra97, Section 15.6] and we will describe it in the following exploiting the representation of the generalized gradients $C^{[n]}_{m,\,c}(z)$ and $C^{[n]}_{m,\,s}(z)$ associated, respectively, to the cosine and sine functions. Considering a magnetic vector potential in an AF gauge (4.78), it is possible to compute the A_x and A_y components simply using

$$A_x = A_\rho \cos(\theta) \quad \text{and} \quad A_y = A_\rho \sin(\theta)\,.$$

The splitting in terms associated to the sine and the cosine functions can be applied also to the vector potential. Considering the representation in terms of generalized gradients we have that the vector potential can be expressed as

$$\begin{aligned}
A_x^{m,\,s} &= \cos(\theta)\frac{\cos(m\,\theta)}{m}\sum_{\ell=0}^{\infty}\frac{(-1)^\ell m!}{2^{2\ell}\ell!(\ell+m)!}C^{[2\ell+1]}_{m,\,s}(z)\rho^{2\ell+m+1}\,,\\
A_x^{m,\,c} &= -\cos(\theta)\frac{\sin(m\,\theta)}{m}\sum_{\ell=0}^{\infty}\frac{(-1)^\ell m!}{2^{2\ell}\ell!(\ell+m)!}C^{[2\ell+1]}_{m,\,c}(z)\rho^{2\ell+m+1}\,,\\
A_y^{m,\,s} &= \sin(\theta)\frac{\cos(m\,\theta)}{m}\sum_{\ell=0}^{\infty}\frac{(-1)^\ell m!}{2^{2\ell}\ell!(\ell+m)!}C^{[2\ell+1]}_{m,\,s}(z)\rho^{2\ell+m+1}\,,\\
A_y^{m,\,c} &= -\sin(\theta)\frac{\sin(m\,\theta)}{m}\sum_{\ell=0}^{\infty}\frac{(-1)^\ell m!}{2^{2\ell}\ell!(\ell+m)!}C^{[2\ell+1]}_{m,\,c}(z)\rho^{2\ell+m+1}\,,\\
A_z^{m,\,s} &= -\frac{\cos(m\,\theta)}{m}\sum_{\ell=0}^{\infty}(2\ell+m)\frac{(-1)^\ell m!}{2^{2\ell}\ell!(\ell+m)!}C^{[2\ell]}_{m,\,s}(z)\rho^{2\ell+m}\,,\\
A_z^{m,\,c} &= \frac{\sin(m\,\theta)}{m}\sum_{\ell=0}^{\infty}(2\ell+m)\frac{(-1)^\ell m!}{2^{2\ell}\ell!(\ell+m)!}C^{[2\ell]}_{m,\,c}(z)\rho^{2\ell+m}\,.
\end{aligned} \tag{4.92}$$

The vector potential in this form is not in a Coulomb gauge, *i.e.* it is not divergence-free, but the following one, called Symmetric Coulomb (SC)

gauge [Dra97, Section 15.5], it is:

$$\begin{aligned}
\widehat{A}_x^{m,\,s} &= \frac{\cos\left((m+1)\theta\right)}{2}\sum_{\ell=0}^{\infty}\frac{(-1)^\ell m!}{2^{2\ell}\ell!(\ell+m+1)!}C_{m,\,s}^{[2\ell+1]}(z)\rho^{2\ell+m+1}\,,\\
\widehat{A}_x^{m,\,c} &= -\frac{\sin\left((m+1)\theta\right)}{2}\sum_{\ell=0}^{\infty}\frac{(-1)^\ell m!}{2^{2\ell}\ell!(\ell+m+1)!}C_{m,\,c}^{[2\ell+1]}(z)\rho^{2\ell+m+1}\,,\\
\widehat{A}_y^{m,\,s} &= \frac{\sin\left((m+1)\theta\right)}{2}\sum_{\ell=0}^{\infty}\frac{(-1)^\ell m!}{2^{2\ell}\ell!(\ell+m+1)!}C_{m,\,s}^{[2\ell+1]}(z)\rho^{2\ell+m+1}\,,\\
\widehat{A}_y^{m,\,c} &= \frac{\cos\left((m+1)\theta\right)}{2}\sum_{\ell=0}^{\infty}\frac{(-1)^\ell m!}{2^{2\ell}\ell!(\ell+m+1)!}C_{m,\,c}^{[2\ell+1]}(z)\rho^{2\ell+m+1}\,,\\
\widehat{A}_z^{m,\,s} &= -\cos\left(m\,\theta\right)\sum_{\ell=0}^{\infty}\frac{(-1)^\ell m!}{2^{2\ell}\ell!(\ell+m)!}C_{m,\,s}^{[2\ell]}(z)\rho^{2\ell+m}\,,\\
\widehat{A}_z^{m,\,c} &= \sin\left(m\,\theta\right)\sum_{\ell=0}^{\infty}\frac{(-1)^\ell m!}{2^{2\ell}\ell!(\ell+m)!}C_{m,\,c}^{[2\ell]}(z)\rho^{2\ell+m}\,.
\end{aligned}\tag{4.93}$$

The x and the y components can be equivalently written as follows

$$\begin{aligned}
\widehat{A}_x^{\widetilde{m},\,s} &= \cos\left(\widetilde{m}\,\theta\right)\sum_{\ell=0}^{\infty}\frac{(-1)^\ell \widetilde{m}!}{2^{2\ell}\ell!(\ell+\widetilde{m})!}B_{\widetilde{m},\,s}^{[2\ell]}(z)\rho^{2\ell+\widetilde{m}}\,,\\
\widehat{A}_x^{\widetilde{m},\,c} &= \sin\left(\widetilde{m}\,\theta\right)\sum_{\ell=0}^{\infty}\frac{(-1)^\ell \widetilde{m}!}{2^{2\ell}\ell!(\ell+\widetilde{m})!}B_{\widetilde{m},\,c}^{[2\ell]}(z)\rho^{2\ell+\widetilde{m}}\,,\\
\widehat{A}_y^{\widetilde{m},\,s} &= \sin\left(\widetilde{m}\,\theta\right)\sum_{\ell=0}^{\infty}\frac{(-1)^\ell \widetilde{m}!}{2^{2\ell}\ell!(\ell+\widetilde{m})!}B_{\widetilde{m},\,s}^{[2\ell]}(z)\rho^{2\ell+\widetilde{m}}\,,\\
\widehat{A}_y^{\widetilde{m},\,c} &= -\cos\left(\widetilde{m}\,\theta\right)\sum_{\ell=0}^{\infty}\frac{(-1)^\ell \widetilde{m}!}{2^{2\ell}\ell!(\ell+\widetilde{m})!}B_{\widetilde{m},\,c}^{[2\ell]}(z)\rho^{2\ell+\widetilde{m}}\,,
\end{aligned}\tag{4.94}$$

where $\widetilde{m} = m+1$ and

$$\begin{aligned}
B_{\widetilde{m},\,s}^{[2\ell]}(z) &= \frac{1}{2\widetilde{m}}\,C_{\widetilde{m}-1,\,s}^{[2\ell+1]}(z)\,,\\
B_{\widetilde{m},\,c}^{[2\ell]}(z) &= -\frac{1}{2\widetilde{m}}\,C_{\widetilde{m}-1,\,c}^{[2\ell+1]}(z)\,.
\end{aligned}$$

Finally, via a gauge transformation $\bar{\boldsymbol{A}} = \widehat{\boldsymbol{A}} + \mathbf{grad}\,\lambda$, a new form of the vector potential can be derived, such that $\bar{A}_x \equiv 0$. The derivation of this so called HFC gauge is described in detail [Dra97] and summarized in the following.

As it will be shown in Section 5.1, the property $\bar{A}_x \equiv 0$ implies that using this representation for the vector potential leads to a significant reduction in the computational cost for the determination of the particle trajectories.

Notice that a gauge transformation is equivalent to a canonical transformation, see *e.g.* [Kob88]. In particular, if we consider a Hamiltonian $\mathcal{K}$, similar to (3.21), with vector potential $\boldsymbol{A}$ and dynamical variables $\boldsymbol{q}$ and $\boldsymbol{p}$ then, using a new vector potential $\boldsymbol{A}' = \boldsymbol{A} + \mathbf{grad}\,\lambda$ we obtain a Hamiltonian $\mathcal{K}'$ in the same form of $\mathcal{K}$ with dynamical variables:

$$\begin{aligned} \boldsymbol{Q} &= \boldsymbol{q}\ ; \\ \boldsymbol{P} &= \boldsymbol{p} + C\,\mathbf{grad}\,\lambda\,, \end{aligned} \tag{4.95}$$

where C denotes, as usual, the particle charge. To derive the HFC gauge transformation, we build a harmonic function λ as

$$\lambda = \sum_{m=0}^{\infty} \left[\sin(m\,\theta)\lambda_{m,\,c} + \cos(m\,\theta)\lambda_{m,\,s}\right]\,, \tag{4.96}$$

where

$$\begin{aligned} \lambda_{m,\,c} &= \sum_{\ell=0}^{\infty} \frac{(-1)^{\ell} m!}{2^{2\ell}\ell!(\ell+m)!} L^{[2\ell]}_{m,\,c}(z)\rho^{2\ell+m}\,, \\ \lambda_{m,\,s} &= \sum_{\ell=0}^{\infty} \frac{(-1)^{\ell} m!}{2^{2\ell}\ell!(\ell+m)!} L^{[2\ell]}_{m,\,s}(z)\rho^{2\ell+m}\,, \end{aligned}$$

and the coefficients $L^{[2\ell]}_{m,\,s/c}(z)$ are related to the coefficients $C^{[2\ell]}_{m,\,s/c}(z)$ by the following relations

$$\begin{aligned} L^{[2\ell]}_{m+1,\,s}(z) &= \frac{1}{m+1}\left[\frac{1}{4m} L^{[2\ell+2]}_{m-1,\,s}(z) - B^{[2\ell]}_{m,\,s}(z)\right]\,, \\ L^{[2\ell]}_{m+1,\,c}(z) &= \frac{1}{m+1}\left[\frac{1}{4m} L^{[2\ell+2]}_{m-1,\,c}(z) - B^{[2\ell]}_{m,\,c}(z)\right] \end{aligned} \tag{4.97}$$

and $L^{[0]}_{m,\,s/c}(z) \equiv 0$ for $m \leq 2$. It is possible to show that $\partial_x \lambda_{s/c} = -\widehat{A}^{s/c}_x$ leading to the desired HFC gauge, *i.e.*

$$\begin{aligned} \bar{A}^s_x &= 0 \qquad \bar{A}^c_x = 0\,, \\ \bar{A}^s_y &= \widehat{A}^s_y + \partial_y \lambda_s\,, \\ \bar{A}^c_y &= \widehat{A}^c_y + \partial_y \lambda_c\,, \\ \bar{A}^s_z &= \widehat{A}^s_z + \partial_z \lambda_s\,, \\ \bar{A}^c_z &= \widehat{A}^c_z + \partial_z \lambda_c\,, \end{aligned} \tag{4.98}$$

where

$$\begin{aligned}\partial_y \lambda_{m,\,c} &= -\sum_{\ell=0}^{\infty} \frac{(-1)^{\ell}}{2^{2\ell}\ell!(\ell+m)!}\left\{(m+1)L^{[2\ell]}_{m+1,\,c} + \frac{1}{4m}L^{[2\ell+2]}_{m-1,\,c}\right\} \\ &\quad \times \rho^{2\ell+m}\cos(m\,\theta)\,, \\ \partial_y \lambda_{m,\,s} &= -\sum_{\ell=0}^{\infty} \frac{(-1)^{\ell}}{2^{2\ell}\ell!(\ell+m)!}\left\{(m+1)L^{[2\ell]}_{m+1,\,s} + \frac{1}{4m}L^{[2\ell+2]}_{m-1,\,s}\right\} \\ &\quad \times \rho^{2\ell+m}\sin(m\,\theta)\,,\end{aligned} \tag{4.99}$$

and $\partial_z \lambda$ is obtained from (4.96)

$$\begin{aligned}\partial_z \lambda = &\sum_{m=0}^{\infty} \sin(m\,\theta) \sum_{\ell=0}^{\infty} \frac{(-1)^{\ell} m!}{2^{2\ell}\ell!(\ell+m)!} L^{[2\ell+1]}_{m,\,c}(z)\rho^{2\ell+m} + \\ &+ \sum_{m=0}^{\infty} \cos(m\,\theta) \sum_{\ell=0}^{\infty} \frac{(-1)^{\ell} m!}{2^{2\ell}\ell!(\ell+m)!} L^{[2\ell+1]}_{m,\,s}(z)\rho^{2\ell+m}\,.\end{aligned} \tag{4.100}$$

4.2.2 Lobatto B-spline Fourier

We consider now instead homogeneous boundary conditions on Γ_D, *i.e.*

$$\psi^{(m)}\big|_{z=0} = \psi^{(m)}\big|_{z=L} = 0\,.$$

We consider for this problem a standard Galerkin method, we therefore introduce the weak formulation as in Section 2.3 which, taking into account the boundary conditions, reads

Problem 4.3. *Find $\psi^{(m)} \in V^m$ such that:*

$$\int_S \partial_\rho \psi^{(m)}\,\partial_\rho v^{(m)}\rho + \partial_z \psi^{(m)}\,\partial_z v^{(m)} + \frac{m^2}{\rho}\psi^{(m)}\,v^{(m)} = \int_{\Gamma_N} g^{(m)} v^{(m)}\rho\,, \quad v^{(m)} \in V^m\,.$$

Here, depending on whether $m = 0$ or not, we consider different V^m spaces. For the case $m = 0$, the third term on the left-hand side, containing $1/\rho$ vanishes, and we can use a standard discretization that matches the homogeneous boundary conditions on Γ_D. For, $m \neq 0$ we are in the framework presented in Section 2.3 (in particular, Problem 2.11 considering scaled quantities with respect to a homogeneous permeability μ) but, since we are just interested in the solution of the Laplace problem, instead of using a discretization that takes into account the whole sequence (2.50), we just chose a

standard discretization as for the case $m = 0$, with the additional constraint of having homogeneous boundary conditions on Γ_0. This is the so called pole condition [Can+06, Equation 3.9.7] which ensures the finiteness of the term

$$\int_S \frac{m^2}{\rho} \psi^{(m)} \, v^{(m)} \, . \tag{4.101}$$

Since the cross-section is a rectangle, there is no need of a NURBS parametrization and we can build a discretization just using, up to a scaling, the tensor product of univariate functions that match the boundary conditions. We choose the Lobatto polynomials $\mathcal{P}_i(\rho)$ to describe the radial dependence and the B-spline functions $B_k^i(z)$. The Lobatto polynomials [ŠSD03, Section 1.2.3] are a set of polynomials defined on $[-1, 1]$, derived from the Legendre polynomials [ŠSD03, Section 1.2.2]. This latter can be defined using the following recurrence relations

$$\begin{aligned} L_0(x) &= 1 \, , \\ L_1(x) &= x, \\ L_k(x) &= \frac{2k-1}{k} x \, L_{k-1}(x) - \frac{k-1}{k} \, L_{k-2}(x) \, , \quad k \geq 2 \, . \end{aligned} \tag{4.102}$$

Legendre polynomials have the nice property of being orthogonal [ŠSD03, Equation 1.42], *i.e.*

$$(L_i, \, L_j)_{L^2(-1,1)} = \frac{2}{2k+1} \delta_{ij} \tag{4.103}$$

but, due to the fact that none of them vanishes at the boundaries [ŠSD03, Equation 1.44], they are not well-suited for the imposition of boundary conditions. For this reason we will use Lobatto polynomials, which are defined combining the Legendre polynomials [ŠSD03, Equation 1.49]:

$$\begin{aligned} \mathcal{P}_0(\rho) &= \frac{1-\rho}{2} \, , \\ \mathcal{P}_1(\rho) &= \frac{\rho+1}{2} \, , \\ \mathcal{P}_k(\rho) &= \frac{1}{\|L_{k-1}\|} \int_{-1}^{\rho} L_{k-1}(x) \mathrm{d}x \, , \quad k \geq 2 \, . \end{aligned} \tag{4.104}$$

In this way the only non-vanishing polynomial on the left and right boundaries will be, respectively, $\mathcal{P}_0$ and $\mathcal{P}_1$, see Figure 4.7. The discretization parameters for this method are the maximum degree of the Lobatto polynomial I and the knot vector Ξ, defining the B-spline space. The discrete space for the Fourier coefficients is then built via tensor product with the proper

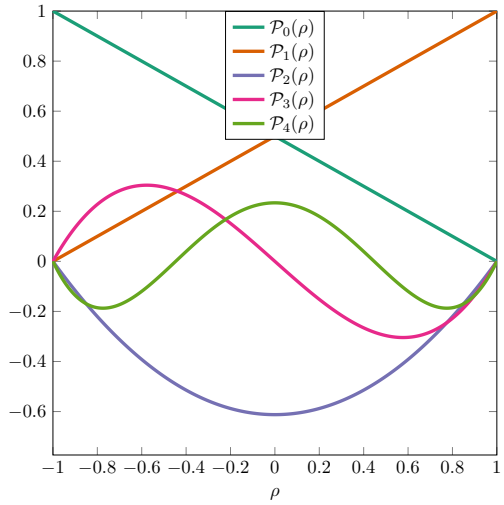

Figure 4.7: First 5 Lobatto polynomials on the reference domain $[-1, 1]$. It can be noticed that the only non-vanishing basis function on the left (right) extremum is $\mathcal{P}_0$ ($\mathcal{P}_1$).

pole condition and the homogeneous boundary conditions for the B-spline space:

$$\begin{aligned} V_h^0 &= \text{span}\left\{\mathcal{P}_i(\rho)B_k(z),\ i = 0, \ldots, I+1,\ k = 2, \ldots, n-1\right\}, \\ V_h^m &= \text{span}\{\mathcal{P}_i(\rho)B_k(z),\ i = 1, \ldots, I+1, \\ &\qquad\qquad k = 2, \ldots, n-1\}, \qquad m \neq 0\,. \end{aligned} \tag{4.105}$$

4.3 Numerical methods for ODEs

In this section, high order numerical methods for the solution of a first order system $\dot{\boldsymbol{w}}(t) = \boldsymbol{f}(t, \boldsymbol{w})$ will be reviewed, in view of their application to the solution of the Hamilton equations. A more detailed presentation of the relevant numerical methods can be found for example in [HLW06].

An important feature of Hamiltonian flows is their symplectic property (see Definition 3.1). When this property is preserved by the numerical method, *i.e.*, if the one-step map $\Phi_{\Delta t} : y_0 \mapsto \Phi_{\Delta t}(y_0) = y_1$ is symplectic, quadratic invariants of motion are preserved, thus ensuring in principle a good behaviour for long-term simulations.

4.3.1 Runge-Kutta methods

The first symplectic techniques that will be considered are Runge-Kutta methods, which can be written in general as

Definition 4.1. *Let b_i, a_{ij} $(i, j = 1, \ldots, s)$ be real numbers and let $c_i = \sum_{j=1}^{s} a_{ij}$. A s-stage Runge-Kutta method is given by:*

$$\begin{aligned} \boldsymbol{w}_{n+1} &= \boldsymbol{w}_n + \Delta t \sum_{i=1}^{s} b_i \, \boldsymbol{f}(t_n + \Delta t \, c_i, \boldsymbol{u}_i) \\ \boldsymbol{u}_i &= \boldsymbol{w}_n + \Delta t \sum_{j=1}^{s} a_{ij} \, \boldsymbol{f}(t_n + \Delta t \, c_j, \, \boldsymbol{u}_j), \quad i = 1, \ldots, s \ . \end{aligned} \tag{4.106}$$

Runge-Kutta methods are often summarized via the so called Butcher tableau, in which all the coefficients are arranged as:

$$\begin{array}{c|ccc} c_1 & a_{1,1} & \cdots & a_{1,s} \\ \vdots & \vdots & \ddots & \vdots \\ c_s & a_{s,1} & \cdots & a_{s,s} \\ \hline & b_1 & \cdots & b_s \end{array} \ .$$

A Runge-Kutta method is explicit if $a_{ij} = 0$ for $j \geq i$. The following theorem gives a sufficient condition for a Runge-Kutta method to be symplectic [HLW06, Theorem 4.3].

Theorem 4.3. *If the coefficients of a Runge-Kutta method satisfy:*

$$b_i \, a_{ij} + b_j \, a_{ji} = b_i \, b_j \quad \forall i, \, j = 1, \ldots, s \tag{4.107}$$

then the method is symplectic.

Gauss methods are particular implicit Runge-Kutta methods, some of which satisfy the condition of Theorem 4.3 and are thus symplectic. The midpoint method can be interpreted as the second-order Gauss method, characterized by the Butcher tableau

$$\begin{array}{c|c} \frac{1}{2} & \frac{1}{2} \\ \hline & 1 \end{array} \ .$$

The fourth-order Gauss method, considered in this paper, is characterized by the Butcher tableau

$$\begin{array}{c|cc} \frac{1}{2}-\frac{\sqrt{3}}{6} & \frac{1}{4} & \frac{1}{4}-\frac{\sqrt{3}}{6} \\ \frac{1}{2}+\frac{\sqrt{3}}{6} & \frac{1}{4}+\frac{\sqrt{3}}{6} & \frac{1}{4} \\ \hline & \frac{1}{2} & \frac{1}{2} \end{array} .$$

The sixth-order Gauss method is instead characterized by the Butcher tableau

$$\begin{array}{c|ccc} \frac{1}{2}-\frac{\sqrt{15}}{10} & \frac{5}{36} & \frac{2}{9}-\frac{\sqrt{15}}{15} & \frac{5}{36}-\frac{\sqrt{15}}{30} \\ \frac{1}{2} & \frac{5}{36}+\frac{\sqrt{15}}{24} & \frac{2}{9} & \frac{5}{36}-\frac{\sqrt{15}}{24} \\ \frac{1}{2}+\frac{\sqrt{15}}{10} & \frac{5}{36}+\frac{\sqrt{15}}{30} & \frac{2}{9}+\frac{\sqrt{15}}{15} & \frac{5}{36} \\ \hline & \frac{5}{18} & \frac{4}{9} & \frac{5}{18} \end{array} .$$

Implicit methods require the solution of a nonlinear system of equations at each time step. This can be done using either the Newton or the fixed-point method. Even though Newton's method is asymptotically superior, numerical results show that the latter is often faster in practice. This behaviour can be justified by the fact that, for the problems at hand, both methods require a small number of iterations to achieve convergence, but the Newton method implies higher initial costs related to the evaluation of Jacobian matrix, see *e.g.* the discussion in [HLW06, Section VIII.6.2]. Also the best known fourth-order explicit Runge-Kutta method has been considered in this work. This method is not symplectic and it is characterized by the Butcher

tableau

$$\begin{array}{c|cccc} 0 & & & & \\ \frac{1}{2} & \frac{1}{2} & & & \\ \frac{1}{2} & 0 & \frac{1}{2} & & \\ 1 & 0 & 0 & 1 & \\ \hline & \frac{1}{6} & \frac{1}{3} & \frac{1}{3} & \frac{1}{6} \end{array} .$$

4.3.2 Lie methods

If $\mathcal{H}$ is the Hamiltonian ruling the evolution of an autonomous system, then the exact solution of the Hamilton equations can be formally represented as

$$\boldsymbol{w}(t) = \exp\left(t : -\mathcal{H} :\right)\boldsymbol{w}_0 \,. \tag{4.108}$$

The methods based on Lie algebra techniques most widely applied in accelerator physics employ a second-order approximation of the Lie transformation. Higher order Lie methods are then built using the procedure introduced by Yoshida in [Yos90] and further discussed in [WFR03]. The first step is to split the Hamiltonian $\mathcal{H}$ in s solvable parts

$$\mathcal{H} = \sum_{i=1}^{s} \mathcal{H}_i$$

such that $\exp\left(: \mathcal{H}_i :\right)$ can be computed exactly for $i = 1, \ldots, s$. This is true if $: \mathcal{H}_i :$ is nilpotent of order two (*i.e.* $: \mathcal{H}_i :^k \boldsymbol{w} = \boldsymbol{0}$ for $k \geq 2$), because in this case the exponential series reduces to a finite sum. A second order approximation is then given by

$$\begin{aligned} &\exp\left(\Delta t : -\mathcal{H} :\right) = \\ &\quad = \exp\left(\frac{\Delta t}{2} : -\mathcal{H}_1 : \right)\exp\left(\frac{\Delta t}{2} : -\mathcal{H}_2 : \right)\ldots \\ &\quad \ldots \exp\left(\Delta t : -\mathcal{H}_s :\right)\exp\left(\frac{\Delta t}{2} : -\mathcal{H}_{s-1} : \right)\ldots \\ &\quad \ldots \exp\left(\frac{\Delta t}{2} : -\mathcal{H}_1 : \right) + o\big(\Delta t^2\big) \,. \end{aligned} \tag{4.109}$$

Denoting by $\mathcal{M}_2(\Delta t)$ the approximation (4.109) and by $\mathcal{M}_{2\ell}(\Delta t)$ an approximation of order 2ℓ, an approximation of order $2\ell+2$ can be built as follows

$$\mathcal{M}_{2\ell+2}(\Delta t) = \mathcal{M}_{2\ell}(\alpha_1\,\Delta t)\mathcal{M}_{2\ell}(\alpha_0\,\Delta t)\mathcal{M}_{2\ell}(\alpha_1\,\Delta t)\ , \tag{4.110}$$

where $\alpha_0 = -\dfrac{2^{1/2\ell+1}}{2-2^{1/(2\ell+1)}}$ and $\alpha_1 = \dfrac{1}{2-2^{1/(2\ell+1)}}$. In this work, methods of order 4 and 6 have been considered, with (α_0, α_1) pairs given by

$$\left(-\frac{2^{1/3}}{2-2^{1/3}}, \frac{1}{2-2^{1/3}}\right) \quad \text{and} \quad \left(-\frac{2^{1/5}}{2-2^{1/5}}, \frac{1}{2-2^{1/5}}\right),$$

respectively. In Table 4.1 we present an example of application of the map $\mathcal{M}_2$ to compute an integration step, from $\boldsymbol{w}_n$ to $\boldsymbol{w}_{n+1}$, for the Hamiltonian (3.21). The solvable parts associated to this system, which will be used in Section 5.1, are

$$\mathcal{K}_1 = P_z - 1, \quad \mathcal{K}_2 = -D_2\,\widetilde{A}_z, \quad \mathcal{K}_3 = \frac{(P_x - D_2\,\widetilde{A}_x)^2}{2(\delta+1)}, \quad \mathcal{K}_4 = \frac{(P_y - D_2\,\widetilde{A}_y)^2}{2(\delta+1)}.$$

$$
\begin{array}{rcl}
\boldsymbol{w}_{n+1/11} & = & \boldsymbol{w}_n + \dfrac{\sigma}{2}\left(0,\ 0,\ \dfrac{\partial \widetilde{A}_z}{\partial X},\ \dfrac{\partial \widetilde{A}_z}{\partial Y}\right)^T;\\
\boldsymbol{w}_{n+2/11} & = & \boldsymbol{w}_{n+1/11} + \left(0,\ 0,\ \widetilde{A}_x,\ \displaystyle\int \frac{\partial \widetilde{A}_x}{\partial Y}\,\mathrm{d}X\right)^T;\\
\boldsymbol{w}_{n+3/11} & = & \boldsymbol{w}_{n+2/11} + \dfrac{\sigma}{2}\left(\dfrac{P_x}{1+\delta_0},\ 0,\ 0,\ 0\right)^T;\\
\boldsymbol{w}_{n+4/11} & = & \boldsymbol{w}_{n+3/11} + \left(0,\ 0,\ -\widetilde{A}_x,\ -\displaystyle\int \frac{\partial \widetilde{A}_x}{\partial Y}\,\mathrm{d}X\right)^T;\\
\boldsymbol{w}_{n+5/11} & = & \boldsymbol{w}_{n+4/11} + \left(0,\ 0,\ +\displaystyle\int \frac{\partial \widetilde{A}_y}{\partial X}\,\mathrm{d}Y,\ +\widetilde{A}_y\right)^T;\\
\boldsymbol{w}_{n+6/11} & = & \boldsymbol{w}_{n+5/11} + \sigma\left(0,\ \dfrac{P_y}{1+\delta_0},\ 0,\ 0\right)^T;\\
\boldsymbol{w}_{n+7/11} & = & \boldsymbol{w}_{n+6/11} + \left(0,\ 0,\ -\displaystyle\int \frac{\partial \widetilde{A}_y}{\partial X}\,\mathrm{d}Y,\ -\widetilde{A}_y\right)^T;\\
\boldsymbol{w}_{n+8/11} & = & \boldsymbol{w}_{n+7/11} + \left(0,\ 0,\ \widetilde{A}_x,\ \displaystyle\int \frac{\partial \widetilde{A}_x}{\partial Y}\,\mathrm{d}X\right)^T;\\
\boldsymbol{w}_{n+9/11} & = & \boldsymbol{w}_{n+8/11} + \dfrac{\sigma}{2}\left(\dfrac{P_x}{1+\delta_0},\ 0,\ 0,\ 0\right)^T;\\
\boldsymbol{w}_{n+10/11} & = & \boldsymbol{w}_{n+9/11} + \left(0,\ 0,\ -\widetilde{A}_x,\ -\displaystyle\int \frac{\partial \widetilde{A}_x}{\partial Y}\,\mathrm{d}X\right)^T;\\
\boldsymbol{w}_{n+1} & = & \boldsymbol{w}_{n+10/11} + \dfrac{\sigma}{2}\left(0,\ 0,\ \dfrac{\partial \widetilde{A}_z}{\partial X},\ \dfrac{\partial \widetilde{A}_z}{\partial Y}\right)^T.
\end{array}
$$

Table 4.1: Application of the map $\mathcal{M}_2$ to $\boldsymbol{w}_n$ in the system (5.4) considering only the variables related to the transversal plane. The fractional index represent inner steps of the algorithm that allow to compute $\boldsymbol{w}_{n+1}$.

Chapter 5

Applications

In this chapter we will apply the methods presented above to several practical problems in the context of particle accelerators. For each case, we will briefly present the challenges regarding the specific application and motivate the choice of the numerical method used to face them.

5.1 Magnetic quadrupole

Magnetic quadrupoles are elements of a particle accelerator whose aim is to produce, in the trasversal plane, a quadrupolar field [Wol14]. They belong to the family of multipole magnets (together with dipoles, sextupoles, octupoles, ...) and have a rotational symmetry with respect to the longitudinal axis z. The effect of a quadrupole over the particles, depending on the orientation of the poles, is to focus them in one transversal direction and to defocus them in the other. The strength of this focusing-defocusing effect is proportional to the distance from the quadrupole centre. Quadrupoles can be described, in first approximation, as optical lenses and it is therefore possible to build a triplet of focusing-defocusing quadrupoles that focuses the particle beam at a specific position, for example, at the so called Interaction Point (IP), where two beams, travelling in opposite directions, collide.

In order to study the effect of the quadrupole on a beam, a first approximate model can be derived considering its field as uniform along the longitudinal direction z and describing it by a two-dimensional function [Wol14, Section 1.2]. This leads to a simple expression for its field. Moreover, considering only the main component of the field leads to a linear model for the description of the particle trajectories, which are, in the general case, described by the Hamilton equations presented in Section 3.2 [Wol14, Section 3.4]. These approximations and the resulting linear model are useful to

derive some stability conditions for the overall particle accelerator. Nevertheless, in certain cases, the two-dimensional model is not sufficiently accurate to describe the beam dynamics. Therefore, a three-dimensional description of the magnetic vector potential, obtained using for example the methods presented in Chapter 4, is needed. Due to the higher complexity of the field description, the integration of Hamilton equations does not lead to an expression for the particle trajectories in a closed-form and numerical methods, as the ones presented in Section 4.3, are needed. In order to evaluate the performance of a particle accelerator when more complicated and accurate models are used, the particle trajectories are simulated for a large number of revolutions inside the whole accelerator and then, relevant quantities for the measure of the overall beam stability and quality are estimated. Depending on the quantity one wants to estimate, a different number of revolutions, that can vary from $\sim 10^3$ to $\sim 10^5$, is used and such long-term simulations motivate the use of symplectic methods.

Another consequence of the large number of revolutions is the need of an efficient method to both describe the field and to compute the particle trajectories. Due to the large radius of the accelerator, quadrupoles are straight elements and, since the particle beams travel in the centre of the magnet, it is possible to represent the magnetic field in a cylindrical domain inside the quadrupole. In this simple geometry, it is possible to describe the magnetic vector potential, needed in the Hamiltonian formulation, using the generalized gradients presented in Section 4.2.1. One of the advantages of using the Fourier series to express the angular dependence of the field is that the rotational symmetry of the quadrupole (and of other multipole magnets) reduces the number of allowed Fourier modes. For example, if we rotate the quadrupole by an angle of $\pi/2$, we have that the magnetic field changes sign. This induces a constraint on the allowed Fourier modes, which are [Wol14, Section 1.2.3]

$$m = 2(2j + 1) \ , \quad j = 0, 1, \dots \ . \tag{5.1}$$

In the following, we will assume that $m \geq 1$. Given the rotational symmetry of the quadrupole, the assumption is justified by (5.1) and avoids the treatment of special cases like the solenoidal field, corresponding to $m = 0$. The interested reader can find further details concerning the description of the beam dynamics in *e.g.* [Dra97; Wol14].

The overall quality of the simulations of a quadrupole are influenced by the numerical method used to compute the particle trajectories and by the accuracy of the field itself. The data that allow to compute the vector potential in the beam region can be provided either by complex simulations of the whole machine [Rus98] or directly by measurements. In practical cases,

the former option is often chosen and the field reconstruction from measurements is used to validate the complex model of the whole magnet, to spot imperfections in the manufacturing process [Röm15] or to obtain the field in those magnets for which a numerical model is not available.

In the first part of this section, we will compare different numerical integrators for the computation of the particle trajectories [Sim+19a]. We mention that a preliminary study on the applicability of a second-order method based on the Lie algebra integrators, proposed in [WFR03], has already been carried out in [Dal+14]. We will first consider an analytical expression for the magnetic vector potential and then we will use sampled data, in the form of longitudinal harmonics, obtained from the simulations of a prototype developed for the HL-LHC project. In both cases, we will mainly consider quadrupolar fields and we will briefly discuss the results of the simulations on the whole accelerator obtained with the CERN tracking code SixTrack [DM+13].
In the second part of this section, we will deal with the problem of reconstructing the field from real measurements. We will model a measurement process and reconstruct the magnetic field solving an inverse problem in a Bayesian framework [IG19]. We will have, in this case, a random quadrupolar field and we can study how the uncertainty on the field affects the uncertainty on the particle trajectories. The results are obtained using synthetic measurement data representing the voltages induced on a spinning coil inside the quadrupole. The outlook is to apply the method to real measurements.

5.1.1 Particle trajectories

Throughout this section, we consider the approximate Hamiltonian (3.21) in the stationary case and without electric scalar potential, *i.e.* $\phi \equiv 0$. In particular, we consider a proton with charge $C \sim 1.602 \times 10^{-19}\,\mathrm{C}$, mass $m \sim 938\,\mathrm{MeV/c^2} \sim 1.67 \times 10^{-27}\,\mathrm{kg}$ and a reference total energy $E = 7\,\mathrm{TeV} \sim 1.12 \times 10^{-6}\,\mathrm{J}$ which corresponds to

$$p^0 = 7\,\mathrm{TeV}\beta/\mathrm{c} \sim 3.74 \times 10^{-15}\,\mathrm{kg\,m/s}\ . \tag{5.2}$$

We use a reference length $L = 1\,\mathrm{m}$ and a reference magnetic flux magnitude B so that $D_2 = 1$. The other dimensionless coefficient $D_1 = p^0/(m\,c)$ is then equal to $\sim 7.5 \times 10^3$.

We then obtain the following Hamilton equations:

$$\dot{\boldsymbol{w}} = \mathbf{J}\,\nabla\mathcal{K} = \begin{bmatrix} \dfrac{P_x - \widetilde{A}_x}{\delta+1} \\ \dfrac{P_y - \widetilde{A}_y}{\delta+1} \\ -\dfrac{\left(P_x - \widetilde{A}_x\right)^2}{2(\delta+1)^2} - \dfrac{\left(P_y - \widetilde{A}_y\right)^2}{2(\delta+1)^2} \\ 1 \\ \dfrac{\partial \widetilde{A}_x}{\partial X}\dfrac{\left(P_x - \widetilde{A}_x\right)}{\delta+1} + \dfrac{\partial \widetilde{A}_y}{\partial X}\dfrac{\left(P_y - \widetilde{A}_y\right)}{\delta+1} + \dfrac{\partial \widetilde{A}_z}{\partial X} \\ \dfrac{\partial \widetilde{A}_x}{\partial Y}\dfrac{\left(P_x - \widetilde{A}_x\right)}{\delta+1} + \dfrac{\partial \widetilde{A}_y}{\partial Y}\dfrac{\left(P_y - \widetilde{A}_y\right)}{\delta+1} + \dfrac{\partial \widetilde{A}_z}{\partial Y} \\ 0 \\ \dfrac{\partial \widetilde{A}_x}{\partial Z}\dfrac{\left(P_x - \widetilde{A}_x\right)}{\delta+1} + \dfrac{\partial \widetilde{A}_y}{\partial Z}\dfrac{\left(P_y - \widetilde{A}_y\right)}{\delta+1} + \dfrac{\partial \widetilde{A}_z}{\partial Z} \end{bmatrix} . \tag{5.3}$$

Moreover, it can be noticed that the Hamiltonian does not depend on ℓ, so that the partial derivative of $\mathcal{K}$ with respect to ℓ is zero. As a consequence, δ is a constant of motion, equal to its initial value, denoted by the subscript 0, *i.e.* δ_0. If the evolution of the variable ℓ is not needed, the canonical pair $(\ell,\, \delta)$ can be neglected, considering δ_0 as a parameter and reducing again the size of the phase space. In this case, the Hamiltonian is still given by (3.21) but, since the dynamical variables are now $\boldsymbol{w} = (X,\, Y, Z,\, P_x,\, P_y,\, P_z)$, the

Hamilton equations become

$$\dot{\boldsymbol{w}} = \mathbf{J}\,\nabla\mathcal{K} = \begin{bmatrix} \dfrac{P_x - \widetilde{A}_x}{\delta_0 + 1} \\ \dfrac{P_y - \widetilde{A}_y}{\delta_0 + 1} \\ 1 \\ \dfrac{\partial \widetilde{A}_x}{\partial X}\dfrac{\left(P_x - \widetilde{A}_x\right)}{\delta_0 + 1} + \dfrac{\partial \widetilde{A}_y}{\partial X}\dfrac{\left(P_y - \widetilde{A}_y\right)}{\delta_0 + 1} + \dfrac{\partial \widetilde{A}_z}{\partial X} \\ \dfrac{\partial \widetilde{A}_x}{\partial Y}\dfrac{\left(P_x - \widetilde{A}_x\right)}{\delta_0 + 1} + \dfrac{\partial \widetilde{A}_y}{\partial Y}\dfrac{\left(P_y - \widetilde{A}_y\right)}{\delta_0 + 1} + \dfrac{\partial \widetilde{A}_z}{\partial Y} \\ \dfrac{\partial \widetilde{A}_x}{\partial Z}\dfrac{\left(P_x - \widetilde{A}_x\right)}{\delta_0 + 1} + \dfrac{\partial \widetilde{A}_y}{\partial Z}\dfrac{\left(P_y - \widetilde{A}_y\right)}{\delta_0 + 1} + \dfrac{\partial \widetilde{A}_z}{\partial Z} \end{bmatrix} . \tag{5.4}$$

A further simplification can be achieved noticing that P_z is decoupled from the other dynamical variables, so that its computation can be neglected if we are only interested in the dynamics of the transversal variables, reducing the number of equations (5.4) to the four ones associated to X, Y, P_x and P_y.

Two-dimensional field description

Before presenting the results, we briefly explain the approximations that lead to the description of the quadrupole effect over a single particle (or a set of non-interacting particles) as a linear map acting on the dynamical variables. This preliminary step is useful to introduce the notation, which is typically introduced in the simple case and then extended to the general one. The interested reader is referred to [Wol14] for a more detailed presentation of linear and nonlinear beam dynamics.
Consider a magnetic flux, expressed in cylindrical coordinates, which is uniform along the longitudinal coordinate z and has no B_z component:

$$\boldsymbol{B}(\rho,\, \theta) = (B_\rho,\, 0,\, B_\theta)^T \,. \tag{5.5}$$

In a vacuum space region with no charges nor currents, the magnetic flux satisfies (see (2.7) and (2.8))

$$\mathbf{curl}^c\,(\mu_0^{-1}\,\boldsymbol{B}) = \mathbf{0} \quad \text{and} \quad \mathrm{div}^c\,\boldsymbol{B} = 0 \,,$$

where μ_0 is the vacuum permeability. With the simple form (5.5), a general solution can be expressed as

$$\begin{aligned} B_\rho(\rho,\,\theta) &= \sum_{m=1}^{\infty} \left(A_m \cos\left(m\theta\right) + B_m \sin\left(m\theta\right)\right)\rho^{m-1} \;, \\ B_\theta(\rho,\,\theta) &= \sum_{m=1}^{\infty} \left(-A_m \sin\left(m\theta\right) + B_m \cos\left(m\theta\right)\right)\rho^{m-1} \;, \end{aligned} \tag{5.6}$$

where A_m and B_m are called, respectively, skew and normal harmonics (or multipoles [Wol14, Section 1.2]). A vector potential that generates (5.6) is the following:

$$A_\rho = 0 \;, \quad A_z = -\Re\left[\sum_{m=1}^{\infty} \frac{1}{m}(B_m + i\,A_m)\,\rho^m\, e^{im\theta}\right] \;, \quad A_\theta = 0 \;. \tag{5.7}$$

The quantities used often in practice are the normal and skew normalized multipole strengths, defined as

$$\begin{aligned} k_m &= \quad \frac{C}{p^0}\, m!\, B_{m+1} \;, \\ k_m^{(s)} &= -\frac{C}{p^0}\, m!\, A_{m+1} \;. \end{aligned} \tag{5.8}$$

Considering a pure normal quadrupole, *i.e.* the only non-vanishing harmonic is B_2, we have a vector potential given by:

$$\boldsymbol{A} = \left(0,\, -\frac{1}{2}\, B_2\, \rho^2 \cos\left(2\theta\right),\, 0\right)^T \;, \tag{5.9}$$

which corresponds to the following magnetic flux:

$$\boldsymbol{B} = \left(B_2\, \rho \sin\left(2\theta\right),\, 0,\, B_2\, \rho \cos\left(2\theta\right)\right)^T \;. \tag{5.10}$$

With this simple expression for the vector potential, using the dimensionless variable (3.17), the Hamilton equations (5.4) for the transversal variables become:

$$\begin{bmatrix} \dot{X} \\ \dot{Y} \\ \dot{P}_x \\ \dot{P}_y \end{bmatrix} = \begin{bmatrix} \dfrac{P_x}{\delta_0 + 1} \\ \dfrac{P_y}{\delta_0 + 1} \\ -\dfrac{C}{p^0} B_2\, X \\ \dfrac{C}{p^0} B_2\, Y \end{bmatrix} = \widetilde{\mathbf{C}} \begin{bmatrix} X \\ Y \\ P_x \\ P_y \end{bmatrix} \;, \tag{5.11}$$

where

$$\widetilde{\mathbf{C}} = \begin{bmatrix} 0 & 0 & a & 0 \\ 0 & 0 & 0 & a \\ -k_1 & 0 & 0 & 0 \\ 0 & k_1 & 0 & 0 \end{bmatrix} , \tag{5.12}$$

with $a = 1/(\delta_0 + 1)$. This ODE system has an exact solution given by

$$\boldsymbol{w}(z_f) = \mathbf{M}\, \boldsymbol{w}_0 \ , \tag{5.13}$$

where $\mathbf{M} = \exp(\widetilde{\mathbf{C}}\,(z_f - z_0))$, $\boldsymbol{w} = (X,\, Y,\, P_x,\, P_y)^T$, the integration interval is delimited by z_0 and z_f, $\boldsymbol{w}_0$ are the initial conditions and

$$\exp\left(\mathbf{B}\right) = \sum_{n=0}^{\infty} \frac{\mathbf{B}^n}{n!} \, . \tag{5.14}$$

Due to the particular structure of $\widetilde{\mathbf{C}}$, $\mathbf{M}$ can be expressed as a matrix whose components are trigonometric and hyperbolic functions, describing, depending on the sign of k_1, the focusing and defocusing effect in each transversal direction. Equation (5.13) is precisely the linear model, also known as thick model [Bur+13], which allows to express the action of a quadrupole using the matrix $\widetilde{\mathbf{C}}$. Subsequent approximations of (5.13), such as the thin model or the teapot slicing [Bur+13], are developed to speed up the computation of the particle trajectories.

Three-dimensional field description

In practical cases, however, the quadrupole field has harmonics of higher order and, since the magnet has a finite length, it is not uniform along z, but decays toward 0 in the so called Fringe Field [Wol14, Section 3.3] region (see Figure 5.5). Of course, it is still possible to express the magnetic flux in terms of Fourier series, in which the radial component is given by

$$B_\rho(\rho,\, \theta,\, z) = \sum_{m=1}^{\infty} B_\rho^{(m)}(\rho,\, z) \cos\left(m\theta\right) + B_\rho^{(-m)}(\rho,\, z) \sin\left(m\theta\right) \ . \tag{5.15}$$

If the field is uniform along z and it is evaluated at a specific radius of analysis R_{an}, then we have the following relation with the multipole coefficients:

$$A_m = \frac{B_\rho^{(m)}(R_{an})}{R_{an}^{m-1}} \quad \text{and} \quad B_m = \frac{B_\rho^{(-m)}(R_{an})}{R_{an}^{m-1}} \ . \tag{5.16}$$

Motivated by this relation, we will refer to $B_\rho^{(m)}$ and to $B_\rho^{(-m)}$ as skew and normal longitudinal harmonics, respectively. We also extend the definition of

the normalized multipole strengths (5.8) to the case of non-uniformity along z:

$$\begin{aligned} k_m(z) &= \frac{C}{p^0}\, m!\, \frac{1}{R_{an}^m}\, B_\rho^{(-(m+1))}(R_{an},\, z)\ , \\ k_m^{(s)}(z) &= -\frac{C}{p^0}\, m!\, \frac{1}{R_{an}^m}\, B_\rho^{(m+1)}(R_{an},\, z)\ . \end{aligned} \tag{5.17}$$

Considering the three-dimensional field of a quadrupole, a two-dimensional description, called HE model [Dra97, Section 16.2.6], is obtained from the longitudinal harmonics considering the peak value and the integral along z of the normalized multipole strength (5.17) (see Figure 5.1) which are, respectively,

$$|k_1| = \max_{z\in\mathbb{R}} |k_1(z)| \quad \text{and} \quad L_1 = \frac{1}{|k_1|}\int_{\mathbb{R}} |k_1(z)|\, \mathrm{d}z\,. \tag{5.18}$$

The sign of k_1 is then chosen such that

$$sign(k_1) = sign\left(\int_{\mathbb{R}} k_1(z)\, \mathrm{d}z\right)\ . \tag{5.19}$$

Analogous quantities can be obtained for other values of m and lead to the

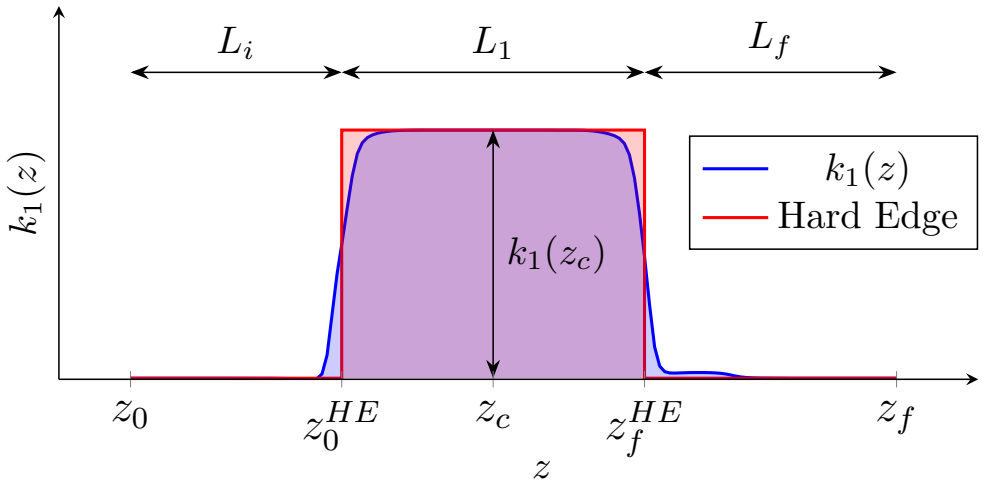

Figure 5.1: The z-dependent description of the field is approximated using the z-uniform HE model.

so called integrated multipoles. These quantities are used in some of the methods used to model the quadrupole effect such as, for example, the thin lens model used in SixTrack [CER].

Generalized gradients field

We will now consider a more complex field described by the generalized gradients (4.88) and compare different numerical integrators, described in Section 4.3, for the computation of the particle trajectories. A more extended presentation of the results shown here can be found in [Sim+19a]. At first, we consider a field generated from the pure quadrupolar generalized gradients given by an analytic expression and depicted in Figure 5.2. It is

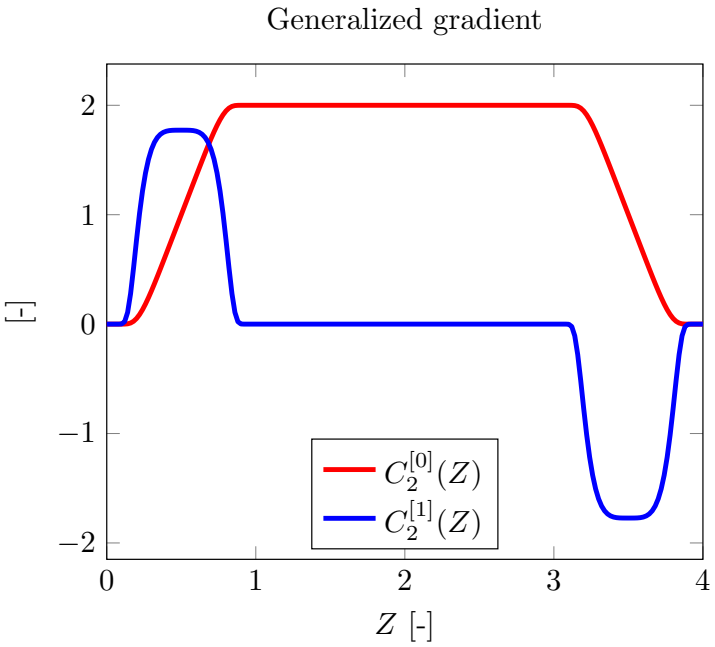

Figure 5.2: Analytic generalized gradient and its derivative.

then possible to compare the accuracy of the different numerical methods as shown in Figure 5.3. It can be noticed that the field limits the convergence rate of the high order methods, which can be achieved only if a sufficiently small integration step is chosen. Moreover, for high order methods and small integration steps, the round-off error limits the achievable accuracy. For the long-term simulations of the whole accelerator it is important to assess the efficiency of each method, measured as the CPU time required to reach a given magnitude of the error. In Figure 5.4, the efficiency comparison is shown. From this comparison on a simple analytical vector potential, it can be noticed that the fourth-order explicit Runge-Kutta method is the most efficient. However, its lack of symplecticity might lead to inaccurate results in long-term simulations. Among the symplectic methods, the second-order Lie method is the most efficient for low accuracy, while higher order methods

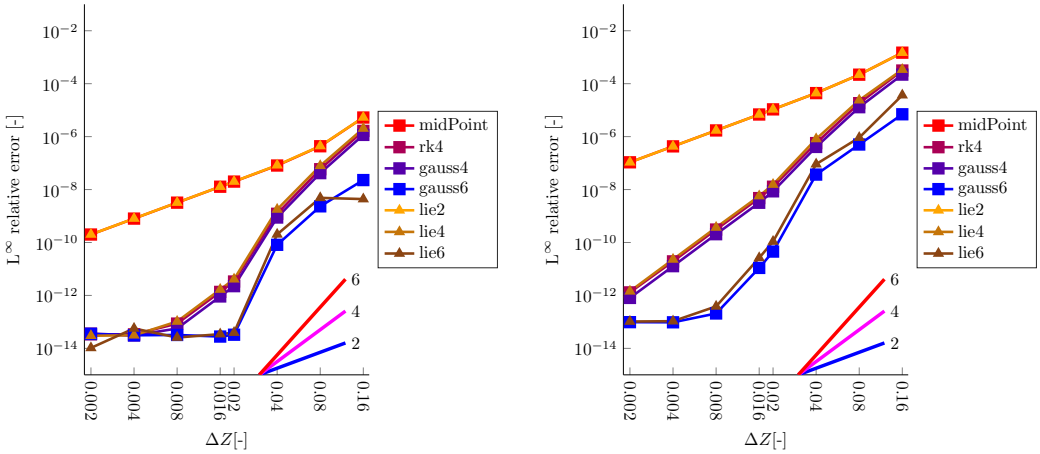

Figure 5.3: Test case with analytically defined vector potential. Convergence behaviour in the l_∞ norm of different ODE methods for X (left) and P_y (right). The straight lines in the bottom right corner denote theoretical slopes for different convergence orders.

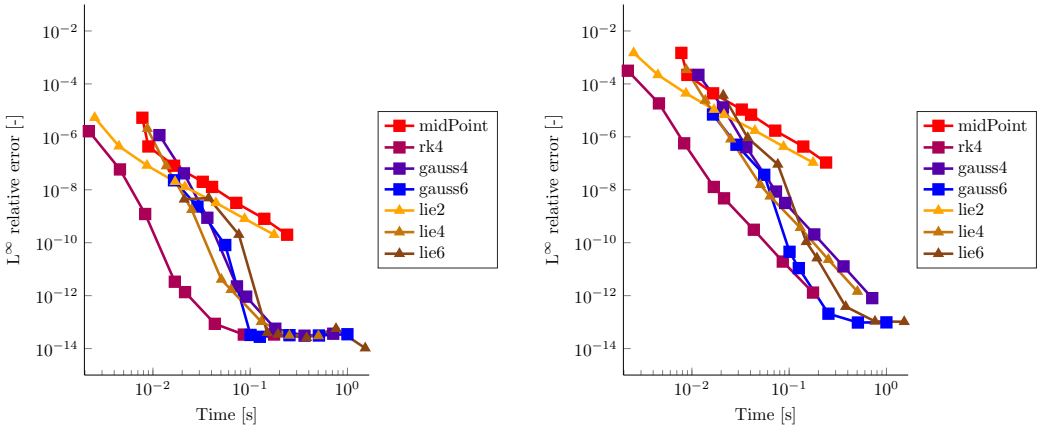

Figure 5.4: Analytic case. Efficiency comparison between ODE methods for X (left) and P_y (right).

such as the fourth-order Lie method or the sixth-order Gauss method become competitive for higher accuracies.

We then compare the method on realistic data coming from the design of a quadrupole for the HL-LHC project. The data are provided as longitudinal harmonics $m = 2, 6, 10, 14$, sampled with a uniform step of 2 cm at $R_{an} = 5$ cm and are depicted in Figure 5.5. The field description, in terms of vector potential, is obtained using the generalized gradients with $ND = 16$ derivatives (see Section 4.2). Moreover, in order to increase the efficiency, we

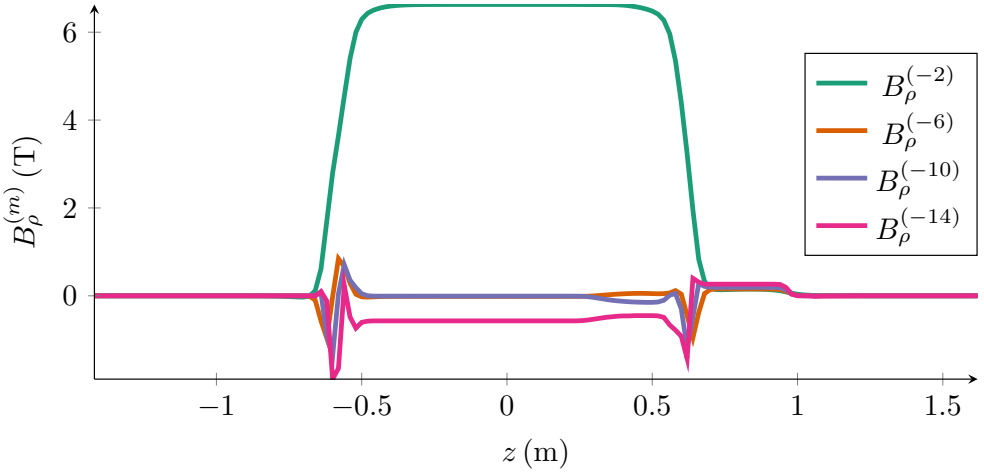

Figure 5.5: Longitudinal harmonics of a realistic design of a quadrupole. The field is uniform in the central part and decays toward 0 in the so called Fringe Field. Note that high order harmonics are stronger in the Fringe Field. (Courtesy of Ezio Todesco and Susana Izquierdo Bermùdez)

exploit the gauging strategy described in Section 4.2.1 using a HFC gauge. In Table 5.1, a speed comparison for the fourth-order Lie method with different gauges is shown and the results motivate the choice of the HFC gauge. The sampling step in the longitudinal direction z limits the accuracy of the field reconstruction and the reliability of the error and efficiency comparison, which can be seen in Figures 5.6 and 5.7, respectively. This is due to the fact that the field values required by the different integrators, including by the one used to compute the reference solution, were obtained through interpolation by means of cubic splines. In this case, as discussed before, the large sampling step in z of the input data limits the possibility of achieving high accuracies, therefore there is no clear advantage in the use of high order methods and the second-order Lie method is the most efficient.
For this realistic case, we present also the comparison of the different methods on a longer simulation. In particular, we simulate the motion of a particle, starting at $X_0 = -0.02$, $Y_0 = 0.01$, through a sequence of 50000 focusing-defocusing quadrupole couples. In Figures 5.8 and 5.9, the phase space trajectories computed, respectively, with the fourth-order Lie method and the fourth-order explicit Runge-Kutta method are shown. It is interesting to note that, in this simple test, the result of the non-symplectic explicit Runge-Kutta method is comparable with the one of the symplectic Lie method.

We will now consider the discrepancies between the particle trajectories computed in the three-dimensional field and those computed using the linear

	Time (s)		Ratio
ΔZ	AF	HFC	HFC/AF
0.02	0.0966	0.0548	0.5680
0.04	0.0474	0.0256	0.5401
0.08	0.0241	0.0132	0.5477
0.16	0.0118	0.0068	0.5726
		Average	**0.557**

Table 5.1: Realistic case. CPU time and speed-up obtained using the AF and the HFC vector potential gauges and the fourth-order Lie method.

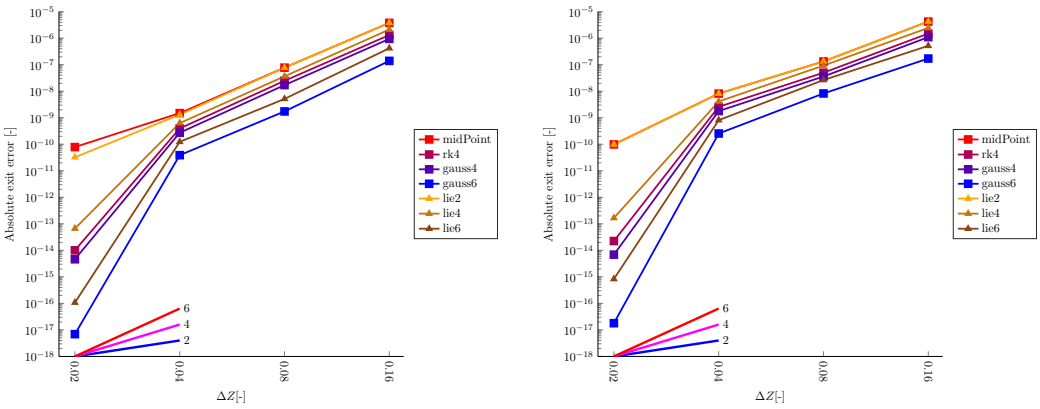

Figure 5.6: Realistic case, cubic spline interpolation. Error comparison between ODE methods for X (left) and P_y (right). The straight lines in the bottom right corner correspond to the theoretical slopes of the error curves for different convergence orders.

model (5.13), to which we will refer with the term nonlinearities. Despite the fact that the magnitude of these discrepancies are smaller than the main linear effect of the quadrupole, it has been shown that they have a significant impact on the overall beam stability [Cai+18]. In order to visualize these discrepancies, a set of different particles, entering the quadrupole with no transversal momenta (moving parallel to the longitudinal axis), but at different positions in the transversal plane, are simulated and the nonlinear effects for the positions and momenta are measured at the quadrupole exit.

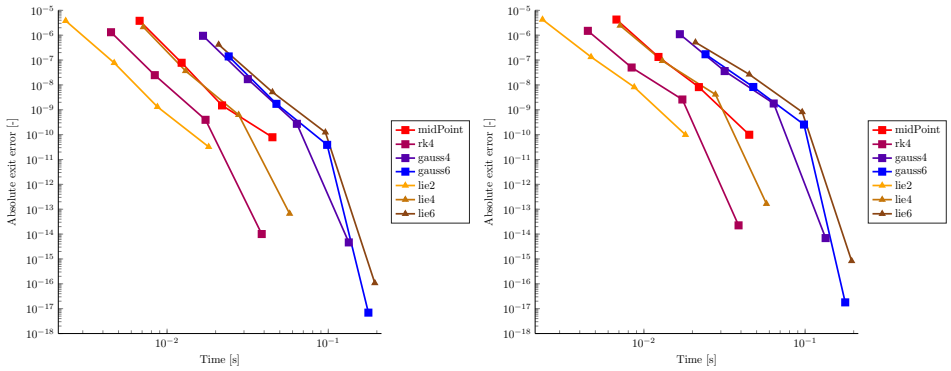

Figure 5.7: Realistic case, cubic spline interpolation. Efficiency comparison between ODE methods for X (left) and P_y (right).

Denoting with the subscript *in* the initial conditions of the particles at the inlet and with *out* the dynamical variables at the outlet computed with a generic integrator, we can compute the nonlinearities as

$$\boldsymbol{w}_{out} - \boldsymbol{w}_{out}^{lin} = \boldsymbol{w}_{out} - \mathbf{M}\boldsymbol{w}_{in} \,, \tag{5.20}$$

where the subscript *lin* indicates the linear model (5.13) with its associated matrix $\mathbf{M}$. The nonlinearities for the X and P_x components are shown in Figure 5.10. The circle drawn on the bottom part of the plots has a radius of R_{an} and represents the positions of the particles at the inlet. It can be noticed that the magnitude of the nonlinearities is larger when the particles travel further from the centre. As a consequence, their accurate description is fundamental in the context of the design of large aperture quadrupoles foreseen for the HL-LHC project [Ros11]. The magnitude of these nonlinear effects can be used to define a threshold on the error shown in Figure 5.7 below which it is possible to choose the fastest method, thus obtaining a first simple criterion to determine the most efficient method regarding the speed and capability of describing the nonlinear effects.

We then compare the sixth-order symplectic Gauss method with the thin lens model currently used in SixTrack [CER], which is based on integrated multipoles, whose definition is analogous to the one given for the quadrupolar component (5.18), and therefore neglects the z-dependence of the field. The version of the thin lens method employed uses 500 slices. In Figure 5.11, it can be seen that there is a good agreement between the two models the momentum nonlinearities, while the position nonlinearities, represented in Figure 5.12, show different behaviours. In particular, the thin model describes the position nonlinearities similarly to the momentum nonlinearities, whereas those computed by the sixth-order Gauss method have a smaller

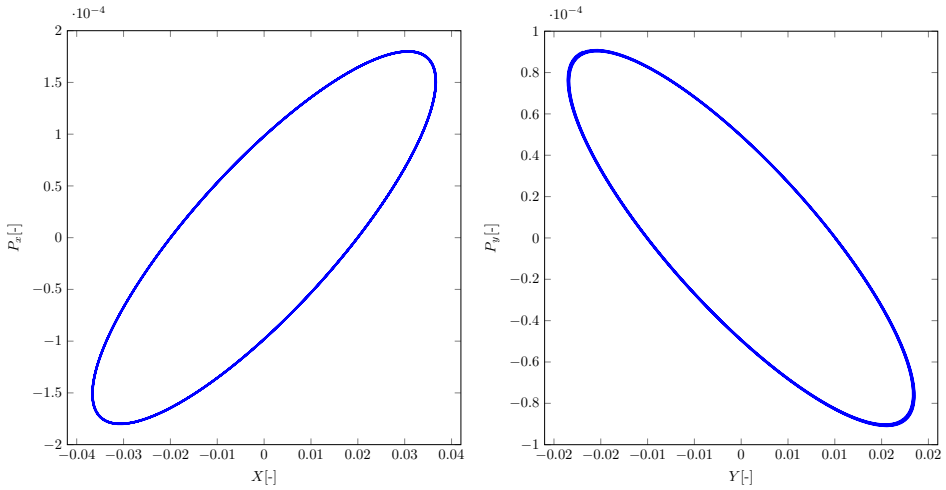

Figure 5.8: Realistic case. Phase-space trajectories in the (X, P_x) (left) and (Y, P_y) (right) planes, $X_0 = -0.02$, $Y_0 = 0.01$. Fourth-order Lie method.

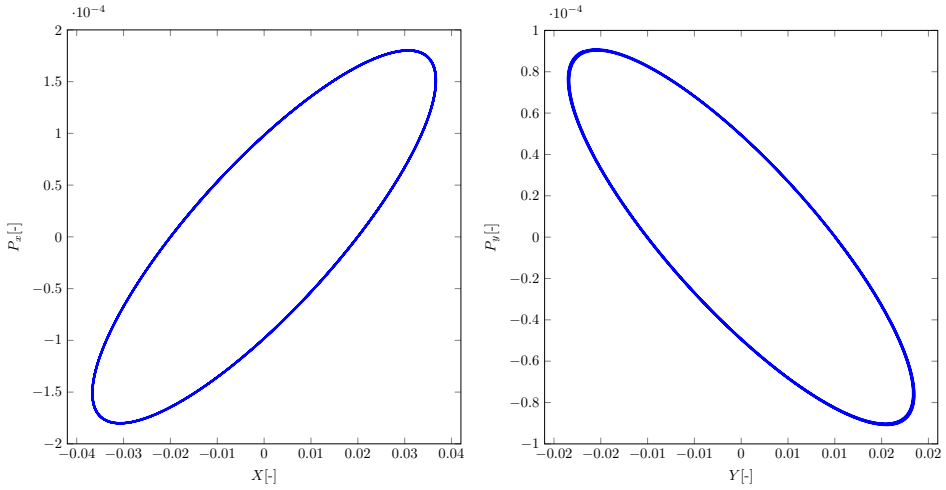

Figure 5.9: Realistic case. Phase-space trajectories in the (X, P_x) (left) and (Y, P_y) (right) planes, $X_0 = -0.02$, $Y_0 = 0.01$. Fourth-order explicit Runge-Kutta method.

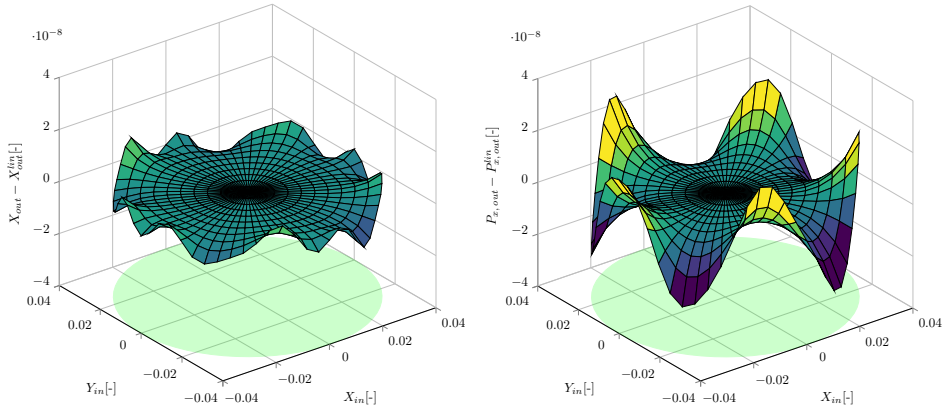

Figure 5.10: Realistic case, nonlinearities of X and P_x for a set of particles starting at different positions in the transversal plane and null transversal momenta.

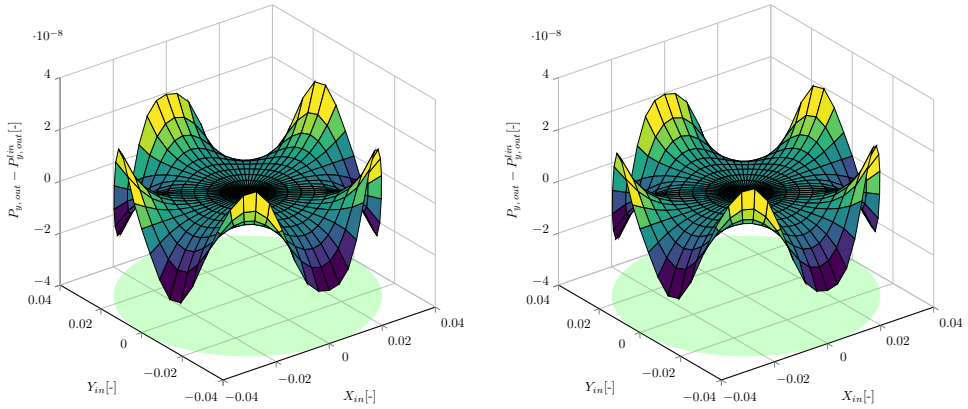

Figure 5.11: Thin lens model. Good agreement between the momentum nonlinearities computed with the thin lens model (left) and the ones computed with the sixth-order symplectic Gauss method (right).

magnitude and a more complex behaviour. We attribute this difference to the asymmetry of the field in the z direction, which cannot be taken into account using integrated multipoles (5.18). In fact, if we consider a symmetric field, which can be obtained adding a specular quadrupole immediately after the first one, we obtain again comparable results for the position nonlinearities too, as can be seen in Figure 5.13. In this latter case, where the field is symmetric and the results seem to be comparable, we can compute the differences between the two models. If we compare the maximum of the differences to the maximum of the nonlinearities, we see a difference of $\sim$ 5-10%, but the maxima correspond to different initial positions in the transversal plane,

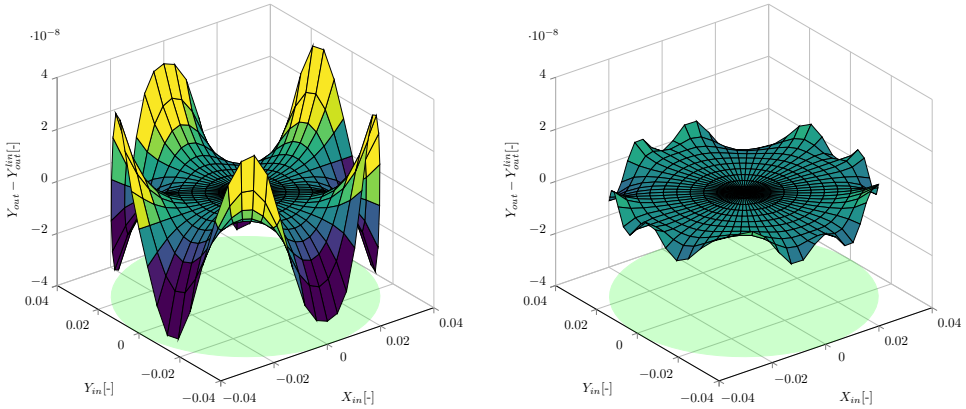

Figure 5.12: Thin lens model. Position nonlinearities computed with the thin lens model (left) and with the sixth-order symplectic Gauss method (right). The position nonlinearities produced by the thin lens model are larger and similar to the momentum nonlinearities.

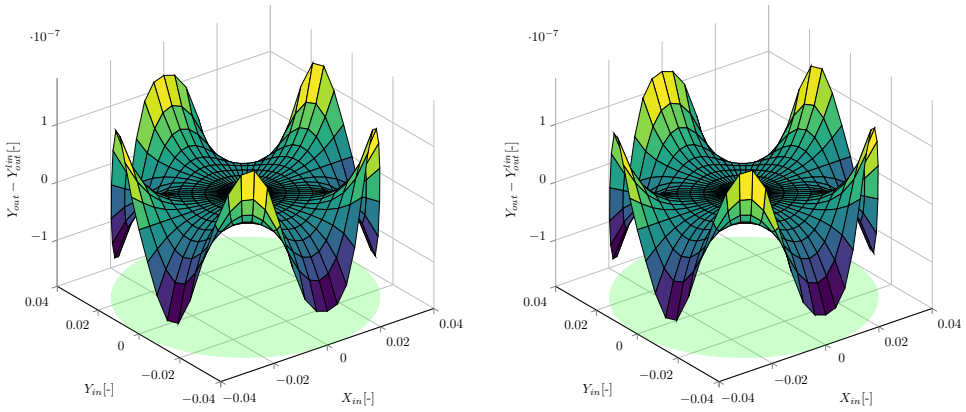

Figure 5.13: Thin lens model, symmetric field obtained considering two adjacent specular quadrupoles. Position nonlinearities computed with the thin lens model (left) and with the sixth-order symplectic Gauss method (right). In this case, where the the field is symmetric with respect to the longitudinal axis z, the results of the two methods are comparable.

so that there is no fixed correspondence, for each entrance position, between the magnitude of the nonlinearities and the magnitude of the differences.

An extension of this work would require, on one hand, to perform the simulations on the whole accelerator to see the effect of this more accurate field description over significant quantities for the beam dynamics and, on the other, to assess the quality of the field description using alternative techniques like the one proposed in Section 4.1.2. The former step is crucial to

identify the most efficient method and might also highlight a bad behaviour for the non-symplectic fourth-order Runge-Kutta method, clarifying the unexpected behaviour shown in Figure 5.9. The latter step, instead, is crucial to understand the impact of the field errors over the overall beam quality and to possibly enhance the efficiency through, for example, a faster field evaluation. Some examples of alternative field description will be given in the next sections.

5.1.2 Vector potential computation using IGA

In this section we briefly present the result of a vector potential computation on a non-trivial geometry using the method presented in Section 4.1.2. We use the Fourier-IGA discretization and we test the method using a manufactured solution which depends on a parameter γ and satisfies the PEC (homogeneous Dirichlet) boundary conditions on Σ_D (at $z = 5$):

$$\boldsymbol{A}^{ex} = \begin{bmatrix} \cos(3\theta)\,(5-z)^3\,\rho^{\gamma+1}\,e^{-\rho} \\ \rho^2\,(\sin(\theta) - 2\sin(\theta)^3)\,(5-z)^\gamma \\ \sin(2\theta)\,(1-\cos(5-z))\,\rho^{\gamma+1} \end{bmatrix} . \tag{5.21}$$

The magnitude of the magnetic flux of the manufactured solution for $\gamma = 2$ is depicted in Figure 5.14. The manufactured solution $\boldsymbol{A}^{ex}$ is not in the

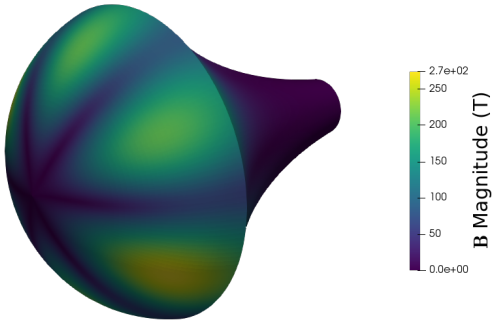

Figure 5.14: Magnitude of the magnetic induction $\boldsymbol{B}$ on the domain for a manufactured solution with $\gamma = 2$.

Coulomb gauge, *i.e.* $\mathrm{div}(\epsilon \boldsymbol{A}^{ex}) \neq 0$, and so will be different from the solution of Problem 2.10. We therefore evaluate the errors comparing the magnetic fluxes, *i.e.* the seminorm in $H_\rho(\mathbf{curl}^m)$. For this testcase we choose the modes

$$m = \pm 1,\ \pm 2,\ \pm 3\,,$$

so that $M = 6$. The regularity of the solution depends on the parameter γ. In Figure 5.15, we compare the error with respect to the number of subdivisions (h-refinement) for different values of the polynomial degree p. Looking at the

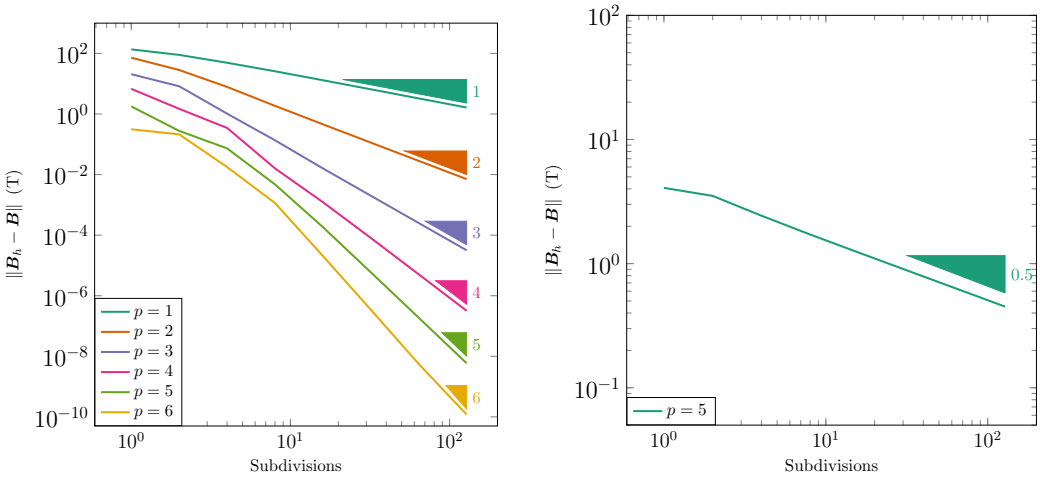

Figure 5.15: Error on the magnetic flux with respect to the number of subdivisions for a regular solution (left, $\gamma = 2$) and for a non-smooth solution (right, $\gamma = 0.5$) which limits the convergence rate.

left plot in Figure 5.15, it can be noticed that for a smooth solution ($\gamma = 2$) the rate of convergence with respect the number of subdivisions is equal to the polynomial degree p. On the contrary, in the right plot of Figure 5.15 the results for a non-regular solution ($\gamma = 0.5$), which limits the convergence rate, are shown. In Figure 5.16, the error is compared against the polynomial degree p (p-refinement) for different number of subdivisions and the spectral convergence is achieved. The method presented in this section has a wide range of applications and can of course be applied also to the simple case of the cylindrical beam region of a magnetic quadrupole. The results of this test, motivate one of the future perspectives of this thesis, which is the use of this method in the particle tracking.

5.1.3 Field reconstruction from measurements

The analysis over the particle trajectories carried out above was considering the field, or the data used for its reconstruction, as exact. This is not the case for data obtained from realistic measurements. In this case, the noise level affects the accuracy of the result. On the other hand, if the data are produced by a numerical model, the main source of uncertainty is related to the model parameters. We will now present the problem of reconstructing the

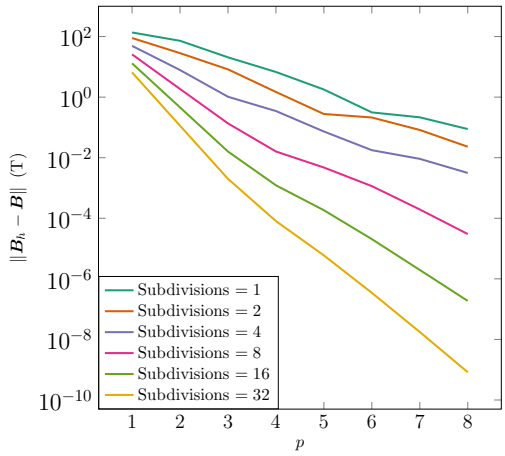

Figure 5.16: Error on the magnetic flux with respect to the polynomial degree p for a regular solution ($\gamma = 2$). It can be noticed the spectral convergence with respect to the p-refinement.

field from a set of measurements. Apart from the uncertainty quantification procedure, this method might be useful to obtain a field description of those magnets for which a numerical model does not exist or to improve an existing one through an hybrid approach that combines the mathematical model with the measured data. The results presented here have been obtained in the framework of the thesis work [IG19]. The Maxwell equations relevant for the modelling of the inner region of a magnetic quadrupole where the beam travels are those for magnetostatic field in a vacuum with neither charges nor currents. The magnetic field $\boldsymbol{H}$ and the magnetic flux $\boldsymbol{B}$ are related through the permeability μ (see Assumption 2.2). In this context, due to the homogeneity of the vacuum, it acts simply as a scaling factor. As already shown in Chapter 2, the magnetic field can be described either using a vector potential (2.9), as in the previous section, or a scalar potential (2.20). The former setting is preferred if the aim is to then perform, as in Section 5.1.1, the particle tracking but, even though the use of a vector potential formulation is perfectly allowed to reconstruct the field from measurements, in the remaining part of this section we consider instead a scalar potential formulation, and in particular, the methods presented in Section 4.2. This choice is due to the fact that the Laplace problem is simpler and the cylindrical geometry of the beam region that we will consider allows to avoid the difficulties related to the parametrization and to employ the spectral basis on the radial direction for which we expect superior approximation properties [Ger+18].

We consider the problem of reconstructing the magnetic scalar potential (2.20) on a cylindrical domain with length L and radius R, where the

Neumann boundary data $g = \boldsymbol{B} \cdot \boldsymbol{\nu}$ are unknown. The information about the field is provided by the following measurement process. We consider a spinning coil [ACR18] placed on the lateral surface of a small cylindrical support, located along the longitudinal axis z, with its centre at z_c, length ℓ and radius R_{an}. The coil spans an angle α and rotates at constant angular speed ω around the longitudinal axis. Due to Faraday's law (2.2), the rotation in a magnetic field induces a voltage on the coil, which is then measured. For this purpose, it is convenient to consider the following parametrized surface whose boundary coincide with the coil:

$$\begin{aligned}\Sigma(t,\, z_c) = \{&R_{an}\, \boldsymbol{e}_\rho + z\, \boldsymbol{e}_z + (\omega t + \theta)\, \boldsymbol{e}_\theta \ , \\ &z \in (z_c - \ell/2,\, z_c + \ell/2),\, \theta \in (0,\, \alpha)\} \ .\end{aligned} \tag{5.22}$$

The right-hand side of Faraday law (2.2) entails the computation the time derivative of an integral over a moving domain. It is possible to bring the time derivation inside the integral using the Leibniz rule for surface integrals [Abr32, Section 12]

$$\begin{aligned}-\frac{\mathrm{d}}{\mathrm{d}t} \int_{\Sigma(t,\, z_c)} \boldsymbol{B} \cdot \boldsymbol{\nu}\, \mathrm{d}\Sigma = &- \int_{\Sigma(t,\, z_c)} \mathrm{div}\,(\boldsymbol{B})\boldsymbol{v} \cdot \boldsymbol{\nu}\, \mathrm{d}\Sigma \\ &+ \int_{\partial\Sigma(t,\, z_c)} (\boldsymbol{v} \times \boldsymbol{B}) \cdot \boldsymbol{\tau}\, \mathrm{d}\Sigma \\ &- \int_{\Sigma(t,\, z_c)} \partial_t \boldsymbol{B} \cdot \boldsymbol{\nu}\, \mathrm{d}\Sigma \ ,\end{aligned} \tag{5.23}$$

where $\boldsymbol{v}$ is the velocity of the moving surface

$$\boldsymbol{v}(t) = \omega\, \rho\, \boldsymbol{e}_\theta \ . \tag{5.24}$$

The first term on the right-hand side in (5.23) vanishes since the magnetic flux is solenoidal (2.8) and the last one vanishes because the magnetic field is stationary. Considering the fact that, on the curved sides of the coil, the tangent vector has the same direction of the velocity, we obtain that the induced voltages are

$$V(t,\, z_c) = \int_{z_c - \ell/2}^{z_c + \ell/2} R_{an}\, \omega\, (B_\rho(R_{an},\, z,\, \omega t) - B_\rho(R_{an},\, z,\, \omega t + \alpha))\, \mathrm{d}z \ . \tag{5.25}$$

Having a known field, for example through its scalar potential ψ, it is therefore possible to compute the induced voltages on the coil and interpret the right-hand side of (5.25) as a (linear) operator, called measurement operator, that acts on the scalar potential

$$V = M(t,\, z_c,\, \ell,\, R_{an},\, \omega)\psi \, . \tag{5.26}$$

The second key ingredient is therefore a description of the scalar potential ψ. This is typically obtained through a finite-dimensional representation, like those presented in Chapter 4. Since the field satisfies Maxwell equations or more specifically, in the particular case considered, the magnetic scalar potential is a solution of the Laplace problem, we can determine ψ knowing only the boundary terms and solving a well-posed problem. Denoting with g the boundary value, we can then define another (linear) operator S, called solution operator, that associates the boundary data to the solution ψ of the well-posed Problem 2.6

$$\psi = S(R,\, L)\, g\,. \tag{5.27}$$

It is also possible to combine the solution and measurement operators defined above to obtain a linear operator, called forward operator, $F = M \circ S$, so that

$$V = (M \circ S) g\,. \tag{5.28}$$

In practical cases, a finite-dimensional representation both for g and ψ is chosen and the forward operator defined above is just a matrix that links the Degrees of Freedom (DoFs) of the boundary representation to the voltages. Specifically, given the basis of a finite-dimensional space

$$\operatorname{span}\left(\{b_i(\rho,\, z,\, \theta)\}_{i=1}^{N_\psi}\right) = Z_h\ ,$$

the approximate magnetic scalar potential is described through its DoFs, grouped in a vector $\boldsymbol{\psi}$, *i.e.*

$$\psi_h(\rho,\, z,\, \theta) = \sum_{i=1}^{N_\psi} \psi_i\, b_i(\rho,\, z,\, \theta)\,. \tag{5.29}$$

If we then compute the induced voltages at N_M different times t and longitudinal positions z_c we can group them in a vector $\mathbf{v} \in \mathbb{R}^{N_M}$ and we have that the matrix representation of the measurement operator $\mathbf{M} \in \mathbb{R}^{N_M \times N_\psi}$ is given by (5.25)

$$\begin{aligned} M_{i,\,j} = &\int_{z_c(i)-\ell/2}^{z_c(i)+\ell/2} R_{an}\, \omega\, \partial_\rho b_j(R_{an},\, z,\, \omega t(i))\, \mathrm{d}z \\ &- \int_{z_c(i)-\ell/2}^{z_c(i)+\ell/2} R_{an}\, \omega\, \partial_\rho b_j(R_{an},\, z,\, \omega t(i) + \alpha)\, \mathrm{d}z\,. \end{aligned} \tag{5.30}$$

Moreover, the finite-dimensional expression of equation (5.26) is

$$\mathbf{v} = \mathbf{M}\, \boldsymbol{\psi}\ . \tag{5.31}$$

An analogous procedure can be applied to the solution operator. Expressing the finite-dimensional representation of the boundary data g_h in terms of the basis functions ψ_h which do not vanish on the boundary, we can describe g_h using a vector of DoFs $\mathbf{g} \in \mathbb{R}^{N_g}$, where $N_g \ll N_\psi$, which we denote as state. Consider now the linear system arising from the discretization of a well-posed problem as Problem 2.6

$$\mathbf{K}\,\boldsymbol{\psi} = \mathbf{E}\,\mathbf{g}\ , \tag{5.32}$$

where $\mathbf{K}$ is the matrix arising from the discretization of the boundary value problem and $\mathbf{E}$ is the matrix that associates the DoFs of $\mathbf{g}$ to the appropriate non-vanishing DoFs of the discretization Z_h. We then have that $\mathbf{K}^{-1}\,\mathbf{E} = \mathbf{S} \in \mathbb{R}^{N_\psi \times N_g}$. Assuming that the measurement process has a negligible effect on the field, we model it as [Bar18]

$$\mathbf{v} = \mathbf{F}\mathbf{g} + \boldsymbol{\eta}, \tag{5.33}$$

where $\mathbf{v}$ is a set of measurements, $\mathbf{F} = \mathbf{M}\,\mathbf{S} \in \mathbb{R}^{N_M \times N_g}$ is the discrete counterpart of the forward operator (5.28) and $\boldsymbol{\eta} \sim \mathcal{N}(\mathbf{0},\, \boldsymbol{\Lambda})$ is a noise term, assumed to be independent on $\mathbf{g}$ and normally distributed with null mean and symmetric positive-definite covariance $\boldsymbol{\Lambda}$. This formula is used to generate synthetic measurements, taking as $\mathbf{g}$ a reference solution that will be then used to assess the quality of the field reconstruction. The aim is therefore to reconstruct the magnetic scalar potential ψ, determined by $\mathbf{g}$, measuring the voltages induced on the coil $\mathbf{v}$. This is an inverse problem that can be solved in a Bayesian framework. A more general treatment of the reconstruction problem, can be found in [IG19], where different methods for the solution of the inverse problem are considered together with nonlinear measurement operators. In a Bayesian setting [Bar18], the terms $\mathbf{g}$ and $\mathbf{v}$ are modelled as random variables, and thus indicated with a capital letter in the following. We also assume to have a prior knowledge of the distribution of $\boldsymbol{G}$ expressed through the prior density function $p_{\boldsymbol{G}}$. Another important density function is the so called likelihood $p_{\boldsymbol{V}|\boldsymbol{G}}(\mathbf{v}|\mathbf{g})$ that, in the simple case of (5.33), takes the form

$$p_{\boldsymbol{V}|\boldsymbol{G}} \sim \mathcal{N}(\mathbf{F}\mathbf{g},\, \boldsymbol{\Lambda})\ . \tag{5.34}$$

It is then possible to obtain the posterior distribution, which expresses the probability of a state given a measurement $\widetilde{\mathbf{v}}$, using the Bayes rule, *i.e.*

$$p_{\boldsymbol{G}|\boldsymbol{V}} = \frac{p_{\boldsymbol{V}|\boldsymbol{G}}(\widetilde{\mathbf{v}}|\mathbf{g})\, p_{\boldsymbol{G}}(\mathbf{g})}{p_{\boldsymbol{V}}(\widetilde{\mathbf{v}})}\ , \tag{5.35}$$

where $p_{\boldsymbol{V}}(\widetilde{\mathbf{v}})$ is called evidence and can be computed as

$$p_{\boldsymbol{V}}(\widetilde{\mathbf{v}}) = \int p_{\boldsymbol{V}|\boldsymbol{G}}(\widetilde{\mathbf{v}}|\mathbf{g})\ p_{\boldsymbol{G}}(\mathbf{g})\, \mathrm{d}\mathbf{g}\ .$$

Once a set of measurements are gathered, it is possible to apply the so called Maximum A Posteriori (MAP) estimator [Bar18] to the state, which amounts to choosing the state $\mathbf{g}_{MAP}$ that maximizes the posterior density function (5.35). If we assume the prior distribution to be normal with mean $\mathbf{g}_0$ and covariance $\mathbf{\Sigma}$, we can obtain the MAP estimate $\mathbf{g}_{MAP}$ solving the following linear system

$$\left(\mathbf{F}^T\,\mathbf{\Lambda}^{-1}\,\mathbf{F}+\mathbf{\Sigma}^{-1}\right)\mathbf{g}_{MAP}=\mathbf{F}^T\,\mathbf{v}+\mathbf{\Sigma}^{-1}\,\mathbf{g}_0\ . \tag{5.36}$$

The measurements can be processed in different ways. The coil can spin at a given location for a certain number of turns N_T before moving to the next location. The acquisition can proceed sequentially from the initial longitudinal position to the end of the quadrupole, performing a so called sweep. Moreover, different sweeps can also be performed. The MAP method can be applied after collecting all the measurements, or can be successively applied to subsets of measurements, updating the mean in the Gaussian prior with the previous MAP estimates and possibly damping the prior covariance matrix. A more elegant approach, which is applicable in our linear case and that provides information on the covariance of the estimated state, is the Kalman filter [Bar18]. In this context, the mean and the covariance of the Gaussian state, indicated with $\mathbf{g}$ and $\mathbf{\Sigma}$, respectively, are updated after each measurement using the following formulas:

$$\begin{aligned}\mathbf{K}&=\mathbf{\Sigma}\,\mathbf{F}^T\left(\mathbf{\Lambda}+\mathbf{F}\,\mathbf{\Sigma}\,\mathbf{F}^T\right)^{-1}\ ,\\ \mathbf{g}'&=\mathbf{g}+\mathbf{K}(\widetilde{\mathbf{v}}-\mathbf{F}\,\mathbf{g})\ ,\\ \mathbf{\Sigma}'&=\mathbf{g}+(\mathbf{I}+\mathbf{K}\,\mathbf{F})\,\mathbf{\Sigma}\ ,\end{aligned} \tag{5.37}$$

where the apostrophe indicates the updated quantities and $\mathbf{K}$ is called Kalman gain. Thanks to the Kalman filter, it is possible to obtain a measure of the uncertainty of the field that can be then propagated through sampling to the particle trajectories, thus estimating the uncertainties on the nonlinearities or on other significant quantities for the beam dynamic. In the following, we present two examples of state estimates using the MAP method and the two discretizations presented in Sections 4.2.1 and 4.2.2, respectively. To this end, we considered a cylinder with radius $R=0.05\,\mathrm{m}$ and length $L=3.04\,\mathrm{m}$. The spinning coil was assumed to have a radius of analysis $R_{an}=0.0375\,\mathrm{m}$, length $\ell=0.05\,\mathrm{m}$, $\alpha=\pi/8$ and an angular speed $\omega=2\pi\,\mathrm{rad\,s^{-1}}$. Over a single coil spin, 256 voltages are measured and the covariance matrix for the measurement noise is

$$\mathbf{\Lambda}=0.1\,\mathbf{A}^T\mathbf{A}\ , \tag{5.38}$$

where the following non-diagonal matrix was used in order to introduce a more complex noise structure:

$$\begin{aligned}\mathbf{A}_{i,j} = \delta_{i,j} - 0.2\left(\delta_{i-1,j} + \delta_{i,j-1} + \delta_{i-2,j} + \delta_{i,j-2}\right) \\ - 0.2\left(\delta_{i-3,j} + \delta_{i,j-3} + \delta_{i-4,j} + \delta_{i,j-4}\right).\end{aligned}$$

The measurement process can be carried out using different strategies. It is possible to choose different numbers of spins at each longitudinal position and, if a sequence of different measurements is taken, it is also possible to consider a different number of complete sweeps. In the case of the BFF method, due to the non-locality of the basis along the longitudinal direction z, it is necessary to consider at once all the measurements corresponding to a complete sweep along all the longitudinal positions [IG19]. In the results shown in Figure 5.17, it is possible to notice the oscillations of the reconstructed harmonics, especially for the mode $m = 6$. Some penalization strategies

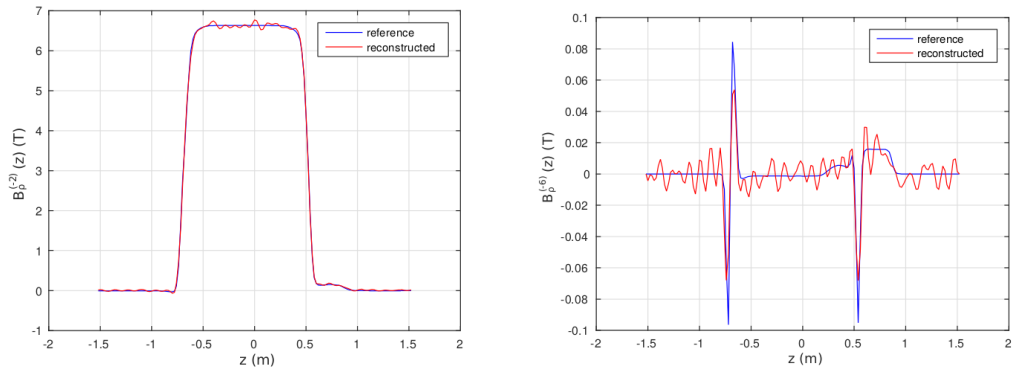

Figure 5.17: Reconstruction using the MAP estimator and the BFF discretization for the modes $m = 2$ (left) and $m = 6$ (right).

on the DoFs corresponding to high frequencies in the longitudinal direction can be applied to reduce the oscillating behaviour of the reconstruction with the BFF method, but this strategy has the drawback of damping the physical peaks of the field [IG19]. The use of the LBF method, presented in Section 4.2.2, is instead well-suited for the application of an updating strategy based on the acquisition of measurements at single longitudinal positions. This has a clear advantage in the perspective of a real measurement process because, combined with uncertainty information that can be obtained from methods like the Kalman filter, it can provide feedbacks on the positions in the magnet that require more measurements. Moreover, the reconstruction with the LBF method and the MAP estimator, provides better results, as can be seen in Figure 5.18. The results presented in this section were ob-

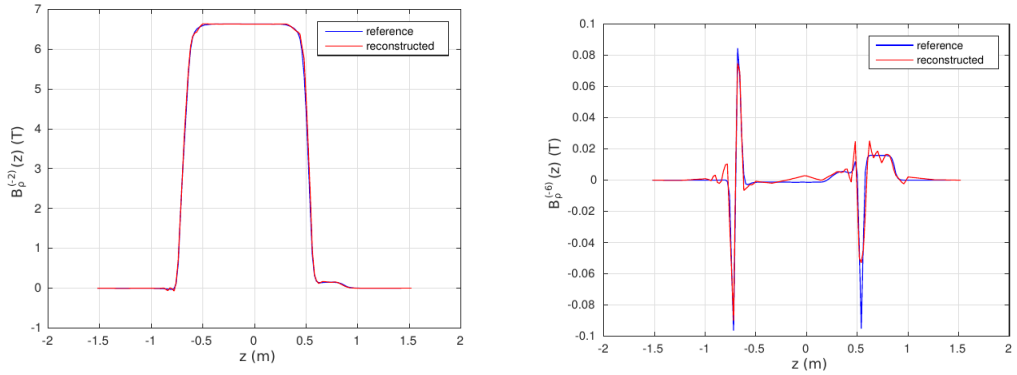

Figure 5.18: Reconstruction using the MAP estimator and the LBF discretization for the modes $m = 2$ (left) and $m = 6$ (right).

tained using synthetic measurements and serve as a motivation to apply the method to realistic measurements. The framework presented here can be easily extended to different types of measurement devices and provides information regarding the uncertainty of the field that can be then propagated to the particle trajectories computation, carried out in Section 5.1.1, and to the assessment of the beam quality.

5.2 Accelerating cavities

Accelerating cavities are another type of element used in particle accelerators often made of superconducting materials. They are used to accelerate the charged particles by means of an oscillating electric field, which is produced in such a way that the particle travelling through the cavity experiences always an accelerating force. The oscillating frequency of the electric field depends, of course, on the particle speed and it should match the principal resonant mode of the cavity. For this reason it is important to accurately compute the resonant frequencies of a cavity, which amounts of solving the eigenvalue problem (2.15) with suitable boundary conditions. The aim of this section is indeed to assess the method presented in Section 4.1.2 in the resolution of the eigenvalue Problem 2.12 on axisymmetric domains. At first, a simple pillbox cavity is considered, for which there exists an analytic expression of the exact solution. We will then consider a practically relevant application which consists of a one cell accelerating TESLA cavity.

5.2.1 Pillbox cavity

A pillbox cavity [Jac07, Section 8.7] is a cylindrical cavity whose cross-section S can be described as a rectangle. We consider here a geometry with radius $R = 35\,\mathrm{mm}$ and length $L = 100\,\mathrm{mm}$ (see figure 5.19) and we want to compute the the eigenvalues/eigenfunctions for the electric field $\boldsymbol{E}$, satisfying Problem 2.12 in which the homogeneous PEC (or Dirichlet) boundary conditions are imposed on $\Gamma_D = \Gamma$ (which correspond to $\Sigma_D = \partial\breve{\Omega}$). We consider the material parameters of a vacuum, which is

$$\epsilon \approx 8.8542 \times 10^{-12}\,\mathrm{F\,m^{-1}}\,, \qquad \mu = 4\pi \times 10^{-7}\,\mathrm{H\,m^{-1}}\,. \tag{5.39}$$

The solutions of (2.15) associated to eigenvalues different from zero can be divided in two classes. One, TM (Transverse Magnetic), is associated to fields where $B_z = 0$ everywhere and $E_z = 0$ on the lateral surface of the cylinder (see figure 5.19, left). The second one, TE (Transverse Electric), is associated to fields where $E_z = 0$ everywhere and $\partial_{\boldsymbol{\nu}} B_z = 0$ on the lateral surface of the cylinder see figure 5.19, right). The corresponding eigenvalues

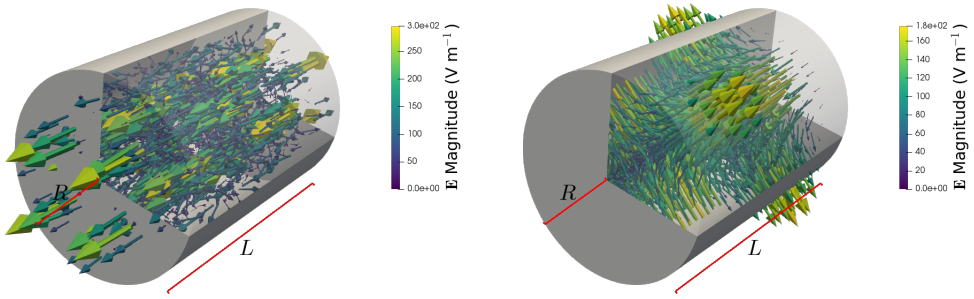

Figure 5.19: Representation of a pillbox cavity of radius $R = 35\,\mathrm{mm}$ and length $L = 100\,\mathrm{mm}$ with the electric field $\boldsymbol{E}$ associated to the eigenfunction $TM423$ (left) and $TE212$ (right).

are given by:

$$\omega^{TM}_{mnq} = \frac{1}{\sqrt{\epsilon\mu}}\sqrt{\frac{\chi^2_{mn}}{R^2} + \frac{q^2\pi^2}{L^2}}\,, \qquad \omega^{TE}_{mnq} = \frac{1}{\sqrt{\epsilon\mu}}\sqrt{\frac{\chi'^2_{mn}}{R^2} + \frac{q^2\pi^2}{L^2}}\,,$$

where χ_{mn} and χ'_{mn} are the n-th root of the Bessel function of the first kind of order m and of its derivative, respectively. The value m is the Fourier mode of the corresponding eigenfunction. As a consequence, for each m we can compute the eigenvalues varying the values of q and n. In the following we consider the case $\omega \neq 0$. In Figure 5.20, the exact value of the first 10 angular

frequencies for $m = 26$ are represented by horizontal blue lines. In the same figure, the approximated angular frequencies are shown for different values of subdivisions of the parametric section (h-refinement) and using a uniform discretization and a maximum degree $p = 3$. It can be seen that no spuri-

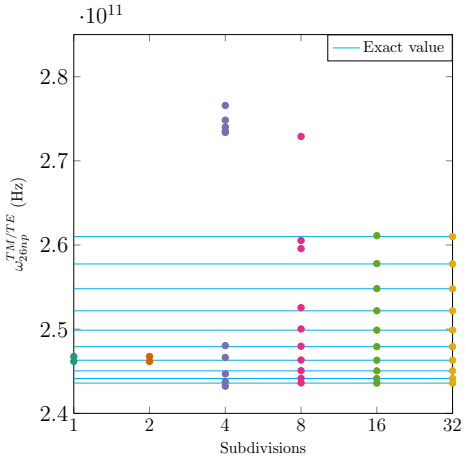

Figure 5.20: Approximations of the first 10 angular frequencies ($m = 26$) for different number of subdivision of the parametric section. The exact values are represented by horizontal blue lines.

ous modes appear and that the computed eigenvalues converge to the real ones. To test the approximation properties of our discretization, a specific eigenvalue ω_{134}^{TE} has been chosen and the error for different subdivisions and degrees p has been computed. In Figure 5.21, the error trends with respect to the to h-refinement (left) and to the number of DoFs (right) are shown. It can be seen that the approximate eigenvalues converge with a rate equal to the double of the polynomial degree p employed in the discretization.

5.2.2 TESLA cavity

We consider now the computation of the resonant modes on a more complex accelerating TESLA cavity whose geometry is defined using a NURBS surface. This type of cavities are used in practical applications and, in particular, the specific design considered in this test is the one-cell midcup TESLA cavity whose precise definition can be found in [Aun+00, Table III]. In Figure 5.22, the first 10 eigenvalues for the mode $m = 1$ are represented for different number of consecutive refinements. It can be noticed that the modes are well separated, no spurious modes occur when the space is refined and they all seem to converge. We consider now the assessment of the approximations properties of the method. To this end, we consider the computation

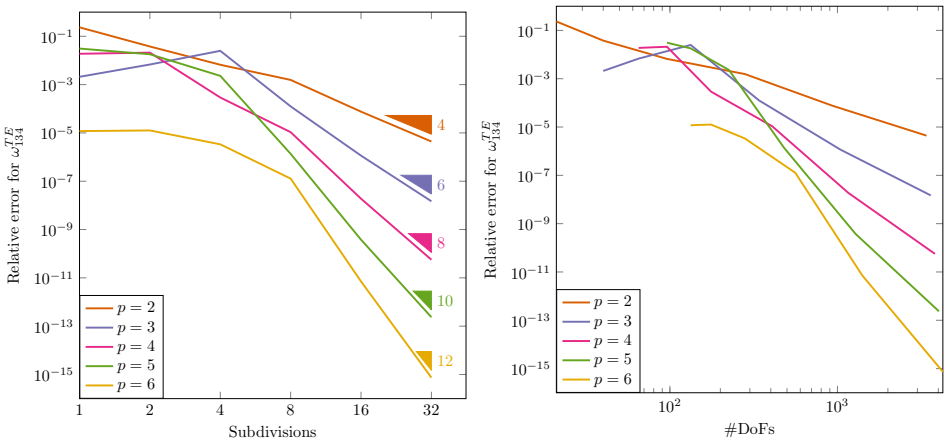

Figure 5.21: Relative error with respect to the number of subdivision of the parametric cross-section $\widehat{S}$ (left) and with respect to the number of DoFs (right) for the angular frequency ω_{134}^{TE}.

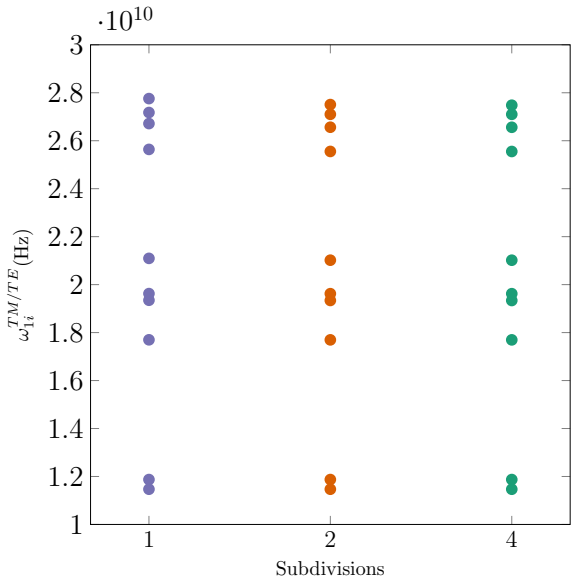

Figure 5.22: TESLA cavity. First 10 eigenvalues associated to the mode $m = 1$ for different level of refinement.

of the lowest resonant angular frequency for the modes $m = 1$ and $m = 2$ which are, respectively,

$$\omega_1 \approx 11\,468.32\,\text{MHz} \quad \text{and} \quad \omega_2 \approx 14\,582.56\,\text{MHz}\,. \tag{5.40}$$

In Figure 5.23, the eigenfunctions associated to the considered eigenvalues are depicted. In Figure 5.24, the trend of the relative errors, estimated as

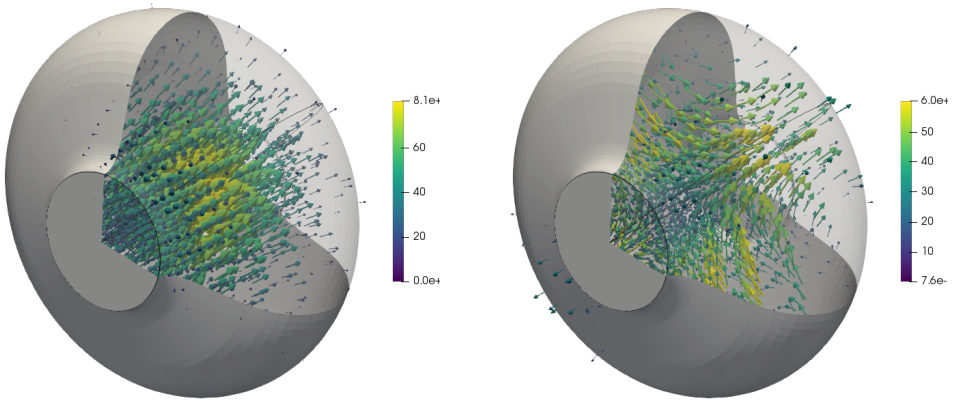

Figure 5.23: TESLA cavity. Eigenfunctions associated to the lowest eigenvalues for the modes $m = 1$ (left) and $m = 2$ (right).

the relative difference between two subsequent refinement levels, are shown. Also in this case, it can be seen that the approximate eigenvalues converges

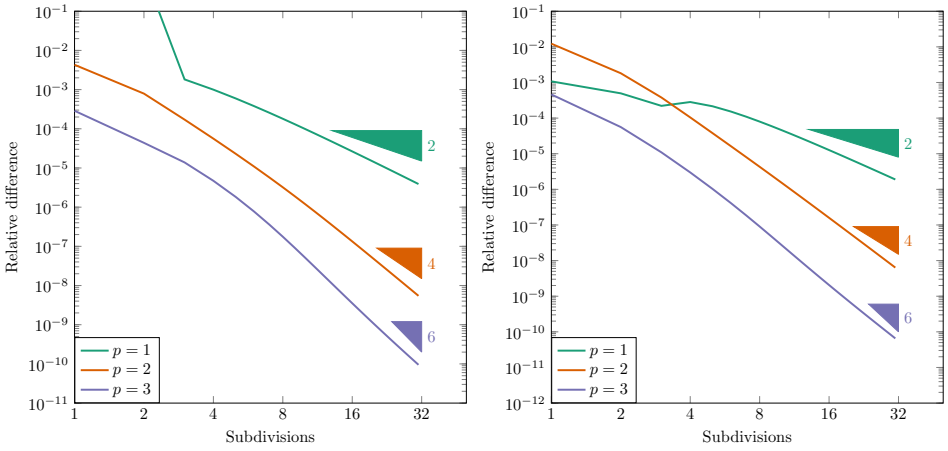

Figure 5.24: TESLA cavity. Error on the lowest eigenvalues $m = 1$ (left) and $m = 2$ (right) with respect to the number of subdivisions for different degrees p of the basis functions.

with a rate similar to the double of the polynomial degree p employed in the discretization. Finally, in Table 5.2, we report the values represented in the right plot of Figure 5.24 with the number of DoFs. The capability of solving a sequence of decoupled $2D$ problems for the different Fourier modes has a significant advantage in terms of computational cost and can be

	$p = 2$		$p = 3$	
Sub	#DoFs	ω_2 (MHz)	#DoFs	ω_2 (MHz)
1	101	11 529.8937	205	11 472.3798
2	205	11 480.5516	345	11 469.0743
4	521	11 469.5215	733	11 468.4131
8	1585	11 468.4242	1941	11 468.3252
16	5441	11 468.3278	6085	11 468.3207
32	20065	11 468.3210	21285	11 468.3206

Table 5.2: TESLA cavity, $m = 1$. Value of the lowest eigenvalue and the number of DoFs for different polynomial degrees p and refinement levels.

applied, for example, in the resolutions of problems that involve the coupling with $3D$ models that might induce non-axisymmetric boundary conditions on axisymmetric domain (see *e.g.* [Cor17, Section 5]).

Chapter 6

Conclusions and future perspectives

In this thesis, we have studied numerical methods for the solution of some problems arising in electromagnetism. A first strong motivation came from the design of high-energy particle colliders and in particular from the need of an accurate computation of the particle trajectories inside magnetic quadrupoles. In this context, we first developed a framework to compare the efficiency of different numerical methods for the computation of the particle trajectories, through the resolution of the Hamilton equations. The comparison was carried out both on a simple analytical field and on a realistic field of a High Luminosity - Large Hadron Collider (HL-LHC) quadrupole. In this framework, we have shown that the use of a specific Horizontal-Free Coulomb (HFC) gauge allowed to improve the overall computational efficiency. The results of the comparison highlighted the need of a sufficiently accurate description of the magnetic field, thus motivating the study of numerical methods for the solution of the Maxwell equations. In particular, we have focused on methods able to provide accurate and efficient descriptions of the field exploiting the symmetry of axisymmetric domains. We therefore combined the Fourier basis and IsoGeometric Analysis (IGA) to exploit the advantages of an exact representation of the computational domain and of the good approximations properties of the IGA discretizations. In this context, the main challenge was to build a sequence of finite-dimensional spaces that constitute a de Rham complex, which is crucial to obtain stable methods that produce physically correct approximations. This objective was achieved using the strategy proposed in [Oh15]. The new methods for the solution of the Maxwell equations in axisymmetric domains were applied to two different problems. The first was the computation of resonant modes in an accelerating TESLA cavity. Due to the nature of the problem, which is well-known

to be hard to solve accurately for methods that do not yield a discrete de Rham complex [Arn18], this realistic testcase was important to assess the approximation properties of the method. The second framework was the reconstruction of unknown field from measurements. In this context, a realistic measurement process with a device known as spinning coil was modelled and the magnetic field was reconstructed solving an inverse problem in a Bayesian setting. It was shown that the proposed reconstruction method is feasible and that discretizations with local support along the longitudinal direction have a significant advantage when modelling the measurement process.

Several results obtained in this thesis could be further improved and future work is necessary to take full advantage of the proposed methods. The efficiency comparison regarding the computation of particle trajectories in a quadrupolar field was carried out measuring the nonlinearities. A crucial further step is to incorporate the proposed methods in the simulation of the whole particle collider, to be able to measure the effect over parameters which are significant for the overall beam stability. This problem is still being studied in collaboration with Thomas Pugnat from Commissariat à l'énergie atomique et aux énergies alternatives (CEA). Some results in this respect were already presented in [Pug+19], where the field has been described using the method based on the generalized gradients. It would be also interesting to apply the new methods for the field reconstruction in the context of particle tracking and to further develop the field reconstructions from measurements, so as to obtain a realistic description of the field uncertainty and to propagate it to the quantities that determine the beam quality. In this respect, the application of the field reconstruction from real measurements (developed in collaboration with Ion Gabriel Ion (TU Darmstadt) and Melvin Liebsch CERN)) is an interesting perspective that might require further improvement from the modelling point of view, but might provide important feedbacks to magnet designers. Concerning the solution of the Maxwell equations in axisymmetric domains, it would be interesting to consider other applications with more complicated geometries and to define bounded cochain projectors from the continuous to the discrete spaces.

Acronyms

AF Azimuthal-Free.

B-spline Basis spline.

BEM Boundary Element Method.

BFF Bessel Fourier Fourier.

BVP Boundary Value Problem.

CAD Computer Aided Design.

CEA Commissariat à l'énergie atomique et aux énergies alternatives.

CERN Conseil Européen pour la Recherche Nucléaire.

DoF Degree of Freedom.

FEM Finite Element Method.

HE Hard Edge.

HFC Horizontal-Free Coulomb.

HL-LHC High Luminosity - Large Hadron Collider.

IGA IsoGeometric Analysis.

IP Interaction Point.

LBF Lobatto B-spline Fourier.

LHC Large Hadron Collider.

MAP Maximum A Posteriori.

NURBS Non-Uniform Rational Basis Spline.

ODE Ordinary Differential Equation.

PEC Perfect Electric Conductor.

PMC Perfect Magnetic Conductor.

SC Symmetric Coulomb.

SI Système international (d'unités).

Bibliography

[ACJL02] F. Assous, P. Ciarlet Jr, and S. Labrunie. "Theoretical tools to solve the axisymmetric Maxwell equations". *Mathematical methods in the applied sciences* 25 (2002), pp. 49–78.

[ACR18] P. Arpaia, G. Caiafa, and S. Russenschuck. "An induction rotating coil for longitudinal scanning of particle accelerator magnets". In: *Journal of Physics: Conference Series*. Vol. 1065. IOP Publishing. 2018.

[AFW10] D. Arnold, R. Falk, and R. Winther. "Finite element exterior calculus: from Hodge theory to numerical stability". *Bulletin of the American mathematical society* 47 (2010), pp. 281–354.

[Abr32] M. Abraham. "The classical theory of electricity and magnetism" (1932).

[Arn18] D. N. Arnold. *Finite element exterior calculus*. Vol. 93. SIAM, 2018.

[Aun+00] B. Aune, R Bandelmann, D Bloess, B Bonin, A Bosotti, M Champion, C Crawford, G Deppe, B Dwersteg, D. Edwards, et al. "Superconducting TESLA cavities". *Physical Review Special Topics-Accelerators and Beams* 3 (2000), p. 092001.

[BR91] O. Biro and K. R. Richter. "CAD in electromagnetism". *Advances in electronics and electron physics* 82 (1991), pp. 1–96.

[BSV13] A. Buffa, G. Sangalli, and R. Vázquez. "Isogeometric methods for computational electromagnetics: B-spline and T-spline discretizations". *Journal of Computational Physics* 257 (2013), pp. 1291–1320.

[Bar18] J. M. Bardsley. *Computational Uncertainty Quantification for Inverse Problems*. Vol. 19. SIAM, 2018.

[Ber+99] C. Bernardi, M. Dauge, Y. Maday, and M. Azaïez. *Spectral methods for axisymmetric domains*. Vol. 3. Series in Applied Mathematics (Paris). Gauthier-Villars, Éditions Scientifiques et Médicales Elsevier, Paris, 1999.

[Bog+05] P. T. Boggs, A. Althsuler, A. R. Larzelere, E. J. Walsh, R. L. Clay, and M. F. Hardwick. *DART system analysis.* Tech. rep. Sandia National Laboratories, 2005.

[Buf+11] A. Buffa, J. Rivas, G. Sangalli, and R. Vázquez. "Isogeometric discrete differential forms in three dimensions". *SIAM Journal on Numerical Analysis* 49 (2011), pp. 818–844.

[Bur+13] H Burkhardt, R De Maria, M Giovannozzi, and T Risselada. "Improved Teapot Method and Tracking with Thick Quadrupoles for the LHC and its Upgrade". CERN-ACC-2013-0059 (2013), 3 p.

[CB93] D. Chapelle and K.-J. Bathe. "The inf-sup test". *Computers & structures* 47 (1993), pp. 537–545.

[CER] CERN. *SixTrack - 6D Tracking Code*. URL: http://sixtrack.web.cern.ch/SixTrack/ (visited on 09/30/2019).

[CGP08] D. Copeland, J. Gopalakrishnan, and J. Pasciak. "A mixed method for axisymmetric div-curl systems". *Mathematics of Computation* 77.264 (2008), pp. 1941–1965.

[CHB09] J. A. Cottrell, T. J. R. Hughes, and Y. Bazilevs. *Isogeometric Analysis: Toward Integration of CAD and FEA*. Wiley, 2009.

[Cai+18] Y. Cai, M. Giovannozzi, R. De Maria, Y. Nosochkov, and F. Van Der Veken. *Dynamic aperture studies for HL-LHC V1. 0.* Tech. rep. 2018.

[Can+06] C. Canuto, M. Y. Hussaini, A. Quarteroni, and T. A. Zang. *Spectral Methods: Fundamentals in Single Domains*. Springer Berlin Heidelberg, 2006.

[Car88] D. C. Carey. "The optics of charged particle beams". *Applied Optics* 27 (1988), p. 1002.

[Cor17] J. Corno. "Numerical Methods for the Estimation of the Impact of Geometric Uncertainties on the Performance of Electromagnetic Devices". PhD thesis. Technische Universität Darmstadt, 2017.

[DM+13] R. De Maria, V Previtali, Y Levinsen, L Lari, F Schmidt, H Renshall, J Barranco, A Mereghetti, R Appleby, V Vlachoudis, et al. *Recent developments and future plans for SixTrack*. Tech. rep. 2013.

[Dal+14] B. Dalena, O. Gabouev, M. Giovannozzi, R. D. Maria, R. Appleby, A. Chancé, J. Payet, and D. Brett. *Fringe fields modeling for the high luminosity LHC large aperture quadrupoles*. Tech. rep. CERN-ACC-2014-0175. CERN, 2014.

[Dra97] A. J. Dragt. *Lie methods for nonlinear dynamics with applications to accelerator physics*. University of Maryland, Center for Theoretical Physics, Department of Physics, 1997.

[Erv13] V. J. Ervin. "Approximation of axisymmetric Darcy flow using mixed finite element methods". *SIAM Journal on Numerical Analysis* 51 (2013), pp. 1421–1442.

[FM88] É. Forest and J. Milutinović. "Leading order hard edge fringe fields effects exact in $(1+\delta)$ and consistent with Maxwell's equations for rectilinear magnets". *Nuclear Instruments and Methods in Physics Research Section A: Accelerators, Spectrometers, Detectors and Associated Equipment* 269 (1988), pp. 474–482.

[GK04] P. W. Gross and P. R. Kotiuga. *Electromagnetic theory and computation: a topological approach*. Cambridge University Press, 2004.

[GO12] J. Gopalakrishnan and M. Oh. "Commuting smoothed projectors in weighted norms with an application to axisymmetric Maxwell equations". *Journal of Scientific Computing* 51 (2012), pp. 394–420.

[GPS02] H. Goldstein, C. Poole, and J. Safko. *Classical mechanics*. American Journal of Physics, 2002.

[Ger+18] P Gervasio, L. Dedé, O Chanon, and A. Quarteroni. "Comparing Isogeometric Analysis and Spectral Element Methods: accuracy and spectral properties". *MOX report No. 21/2018* (2018).

[HL05] R. Hiptmair and P. D. Ledger. "Computation of resonant modes for axisymmetric Maxwell cavities using *hp*-version edge finite elements". *International journal for numerical methods in engineering* 62 (2005), pp. 1652–1676.

[HLW06] E. Hairer, C. Lubich, and G. Wanner. *Geometric numerical integration: structure-preserving algorithms for ordinary differential equations*. Springer Science & Business Media, 2006.

[Hip02] R. Hiptmair. "Finite elements in computational electromagnetism". *Acta Numerica* 11 (2002), pp. 237–339.

[IG19] I. Ion Gabriel. "Bayesian methods for magnetic field reconstruction from measurements." *M.Sc. Thesis* (2019). Supervisors: U. Römer and S. Schöps and A. Simona.

[Jac07] J. D. Jackson. *Classical electrodynamics*. John Wiley & Sons, 2007.

[KF75] A. N. Kolmogorov and S. V. Fomin. *Introductory real analysis*. Courier Corporation, 1975.

[Kob88] D. H. Kobe. "Gauge transformations in classical mechanics as canonical transformations". *American Journal of Physics* 56.3 (1988), pp. 252–254.

[Lac00] P. Lacoste. "Solution of Maxwell equation in axisymmetric geometry by Fourier series decompostion and by use of H (rot) conforming finite element". *Numerische Mathematik* 84 (2000), pp. 577–609.

[Lic19] M. Licht. "Smoothed projections and mixed boundary conditions". *Mathematics of Computation* 88 (2019), pp. 607–635.

[MR82] B. Mercier and G. Raugel. "Résolution d'un problème aux limites dans un ouvert axisymétrique par éléments finis en r, z et séries de Fourier en θ". *RAIRO. Analyse numérique* 16 (1982), pp. 405–461.

[Mon+03] P. Monk et al. *Finite element methods for Maxwell's equations*. Oxford University Press, 2003.

[Méo12] F Méot. *Zgoubi users guide*. Tech. rep. Brookhaven National Laboratory (BNL), 2012.

[Neč62] J. Nečas. "Sur une méthode pour résoudre les équations aux dérivées partielles du type elliptique, voisine de la variationnelle". *Annali della Scuola Normale Superiore di Pisa-Classe di Scienze* 16 (1962), pp. 305–326.

[Nis] *NIST Digital Library of Mathematical Functions*. F. W. J. Olver, A. B. Olde Daalhuis, D. W. Lozier, B. I. Schneider, R. F. Boisvert, C. W. Clark, B. R. Miller and B. V. Saunders, eds.

[Nke05] B. Nkemzi. "On the solution of Maxwell's equations in axisymmetric domains with edges". *ZAMM-Journal of Applied Mathematics and Mechanics/Zeitschrift für Angewandte Mathematik und Mechanik: Applied Mathematics and Mechanics* 85 (2005), pp. 571–592.

[Oh15] M. Oh. "de Rham complexes arising from Fourier finite element methods in axisymmetric domains". *Computers & Mathematics with Applications* 70 (2015), pp. 2063–2073.

[PP62] W. H. Panofsky and M. Phillips. *Classical electricity and magnetism*. Addison Wesley, 1962.

[Per+17] S. Perotto, A Reali, P Rusconi, and A. Veneziani. "HIGAMod: A Hierarchical IsoGeometric Approach for MODel reduction in curved pipes". *Computers & Fluids* 142 (2017).

[Pug+19] T. Pugnat, B. Dalena, A. Simona, L. Bonaventura, R. De Maria, and V. Berglyd Olsen. "Study of Fringe Fields Effects from Final Focus Quadrupoles on Beam Based Measured Quantities". In: *10th International Particle Accelerator Conference IPAC2019*. 2019, pp. 90–93.

[Ros11] L. Rossi. "LHC upgrade plans: Options and strategy". In: *Second International Particle Accelerator Conference, San Sebastian*. 2011.

[Rus98] S. Russenschuck. "ROXIE–a computer code for the integrated design of accelerator magnets". In: *Sixth European Particle Accelerator Conference, Stockholm, Sweden*. 1998, pp. 2017–2019.

[Röm15] U. Römer. "Numerical approximation of the magnetoquasistatic model with uncertainties and its application to magnet design". PhD thesis. Technische Universität, 2015.

[SS11] S. A. Sauter and C. Schwab. *Boundary Element Methods*. Berlin-Heidelberg: Springer, 2011.

[Sch81] L. L. Schumaker. *Spline functions: Basic theory*. Pure and applied mathematics: A Wiley-Interscience series of texts, monographs, and tracts. New York, Chichester, Brisbane: J. Wiley & Sons, 1981.

[Sim+19a] A. Simona, L. Bonaventura, T. Pugnat, and B. Dalena. "High order time integrators for the simulation of charged particle motion in magnetic quadrupoles." *Computer Physics Communications* 239 (2019), pp. 33–52.

[Sim+19b] A. Simona, L. Bonaventura, C. de Falco, and S. Schöps. "Isogeometric approximations for electromagnetic problems in axisymmetric domains." *In preparation* (2019).

[UP14] D Uriot and N Pichoff. "TraceWin". *CEA Saclay, June* (2014).

[Vei+14] L. Beirão da Veiga, A. Buffa, G. Sangalli, and R. Vázquez. "Mathematical analysis of variational isogeometric methods". *Acta Numerica* 23 (2014), pp. 157–287.

[Vei+16] L. B. da Veiga, A. Buffa, G. Sangalli, and R. Vázquez. "An introduction to the numerical analysis of isogeometric methods". *Numerical simulation in physics and engineering*. Springer, 2016, pp. 3–69.

[WFR03] Y. Wu, E. Forest, and D. Robin. "Explicit symplectic integrator for $s-$dependent static magnetic field". *Physical Review E* 68 (2003), p. 046502.

[Wol14] A. Wolski. *Beam dynamics in high energy particle accelerators*. World Scientific, 2014.

[XZ03] J. Xu and L. Zikatanov. "Some observations on Babuška and Brezzi theories". *Numerische Mathematik* 94 (2003), pp. 195–202.

[Yos90] H. Yoshida. "Construction of higher order symplectic integrators". *Physics Letters A* 150 (1990), pp. 262–268.

[ŠSD03] P. Šolín, K. Segeth, and I. Doležel. *Higher-order finite element methods*. CRC Press, 2003.

Acknowledgements

This thesis was developed in the context of a joint PhD programme between the Politecnico di Milano and the Technische Universität Darmstadt. This work has been partially supported by the 'Excellence Initiative' of the German Federal and State Governments and the Graduate School of Computational Engineering at Technische Universität Darmstadt.

I would like to thank Thomas Pugnat and Barbara Dalena with whom I collaborated on the topic of particle tracking and Ezio Todesco and Susana Izquierdo Bermúdez for providing the longitudinal harmonics data for a realistic design of a quadrupole for the HL-LHC project. I would also like to thank Kersten Schmidt and Minah Oh for the fruitful discussion regarding the discretization in axisymmetric domains and Ion Gabriel Ion and Melvin Liebsch for the collaboration on the field reconstruction from measurements. I appreciated the detailed and useful reviews of Dr. Ing. habil. Stephan Russenschuck and Prof. Rafael Vázquez which significantly improved the quality of this thesis.

I am very grateful to Prof. Luca Bonaventura, Prof. Sebastian Schöps and Prof. Carlo de Falco for their constant support during this experience, providing different point of views and valuable advices that guided me.

Finally, I would like to thank all the TEMF students at GSC for their warm welcome and friendship that made my stay in Darmstadt great.

Scrivo la seconda parte dei ringraziamenti in italiano, incominciando da tutte le persone del Tender. Siete stati degli ottimi compagni del viaggio che ha trasformato sia me che il Tender stesso. Un importante grazie va a tutta la mia famiglia, che mi ha supportato e incoraggiato in questa esperienza come nel passato, e a Stefania, per essermi stata accanto in tutti i momenti.

As a last note, I want to thank also all the wonderful people I met during these years (also those I did not mention above), with the hope of meeting them again in the future.